

THE ROLE OF MICRO AND ULTRA-STRUCTURE IN MICRODAMAGE  
ACCUMULATION IN CANCELLOUS BONE

A Dissertation

Presented to the Faculty of the Graduate School  
of Cornell University

In Partial Fulfillment of the Requirements for the Degree of  
Doctor of Philosophy

by

Matthew Goff

August 2015

© 2015 Matthew Goff

# THE ROLE OF MICRO AND ULTRA-STRUCTURE IN MICRODAMAGE ACCUMULATION IN CANCELLOUS BONE

Matthew Goff, Ph. D.

Cornell University 2015

Bone fractures affect over 1.5 million people a year in the United States and can lead to a decrease in life expectancy and quality of life. While some fractures occur due to a single overloading event such as a fall, many fractures develop over time. Insufficiency fractures are one type of fracture that develop over time and typically occur in regions of the skeleton dominated by cancellous bone. In cancellous bone, the accumulation of microdamage results in a loss of biomechanical performance and is believed to contribute to fracture incidence. However, relatively little is known about the how microdamage accumulates in cancellous bone and the aspects of cancellous bone structure that influence the development of microdamage.

While the development of microdamage is driven by stresses and strains at the tissue-level, the complex microarchitecture of cancellous bone prevents the direct measurement of tissue-level stresses/strains. Additionally, naturally forming stress concentrations called resorption cavities form on the surface of cancellous bone. Finite element models can be used to calculate the tissue-level stress/strain in cancellous bone. According to finite element models, the largest stresses/strains will occur at the surface of cancellous bone and the stresses around resorption cavities will be higher than other surfaces of the bone. However, finite element models are created from

three-dimensional images of the bone and the images are not typically obtained at resolutions capable of examining resorption cavities. Additionally, the material properties of cancellous bone are not homogeneous and may influence the location of microdamage formation. The oldest and stiffest tissue is found near the center of trabeculae away from the locations that experience the highest stresses. Therefore, first, we characterized the size and location of resorption cavities. Next, we explored the spatial relationship between microdamage and resorption cavities by developing three-dimensional spatial correlation techniques and determining the spatial relationship between microdamage and resorption cavities. Finally, we examined how well tissue-level strains measured from finite element models predicted the location of microdamage

The size and location of resorption cavities suggest that they can generate large stress concentrations in cancellous bone. However, microdamage preferentially formed away from resorption cavities, and the majority of microdamage was located distant from the surface of trabeculae. Additionally, reductions in biomechanical performance during fatigue loading were explained primarily by the largest microdamage sites. Hence, only microdamage sites larger than a certain size appear to influence the mechanical performance of cancellous bone following cyclic loading. Furthermore, when using finite element models, regions of cancellous bone displaying the greatest principal tissue strains were able to predict the location of the largest and most biomechanically relevant microdamage sites.

Together, the current work suggests that losses in biomechanical performance following damage accumulation in cancellous bone are due to a few large

microdamage sites that form near the center of trabeculae. Furthermore, microdamage accumulation is poorly related to location stress concentration due to microgeometry, suggesting that other factors such as tissue heterogeneity may be more influential in determining microdamage accumulation.

## BIOGRAPHICAL SKETCH

Matthew Geoffrey Goff was born in Clearwater, Florida in 1988. He graduated from St. Petersburg High School in 2006 and was named the St. Petersburg Times' Scholar-Athlete of the Year. In 2010, he graduated summa cum laude from the University of Florida in Gainesville, Florida, with a Bachelor of Science degree in Mechanical Engineering. While at the University of Florida, he performed research on tracking autonomous robots through dead-reckoning. He served as the vice president of members in the Pi Tau Sigma honor society. He volunteered at the Alachua County Crisis hotline where he talked callers through difficult situations and in some cases out of suicide. He wrestled for the University of Florida club team. In his final year at the University of Florida, he worked at RTI Biologics where he performed research on human tissue and designed surgical equipment. In 2013, he received his Master of Science degree in Biomedical Engineering. While at Cornell, he received the Howard Hughes Medical Institute Med into Grad fellowship and passed the fundamentals of engineering exam in mechanical engineering.

## ACKNOWLEDGMENTS

I would like to thank my wife Lianyi, my son Luke and my parents for their support and encouragement. I would also like to thank the collaborators that assisted me with my research. Additionally, I would like to thank my graduate advisory committee for their guidance and insight into crafting both my research and presenting my data. Finally, I would like to acknowledge the National Institutes of Health, the National Science Foundation, and the Howard Hughes Medical Institute for funding the research in this dissertation.

## TABLE OF CONTENTS

Biographical Sketch	iii
Acknowledgements	Iv
Table of Contents	V
List of Figures	viii
List of Tables	X
Chapter 1: Introduction	11
1.1 Fracture in Bone	11
1.2 Bone Composition and Architecture	12
1.3 Mechanical Testing of Bone	14
1.4 Mechanical Properties of Bone	16
1.5 Modeling the Distribution of Stress/Strain in Bone	19
1.6 Microdamage in Bone	20
1.7 Bone Remodeling	23
1.8 Imaging Bone	26
1.9 Thesis Aims	27
1.9.1 Aim 1	28
1.9.2 Aim 2	29
1.9.3 Aim 3	30
1.9.4 Aim 4	31
Chapter 2: Three-Dimensional Morphology of Resorption Cavities	33
2.1 Abstract	33
2.2 Introduction	34
2.3 Materials and Methods	37
2.3.1 Image Acquisition and Processing	37
2.3.2 Identification of Resorption Cavities in Three-Dimensional Images	38
2.3.3 Automated Measures of Cavity Size in Three-Dimensional Images	41
2.3.4 Determination of Cavity Location	44
2.3.5 Statistical Analyses	44
2.4 Results	45
2.5 Discussion	55
2.6 Acknowledgements	62
2.7 Supplementary Material	63
Chapter 3: Techniques to Detect the Proximity of Objects in Three- Dimensional Models	67
3.1 Abstract	67
3.2 Introduction	68
3.3 Materials and Methods	70
3.3.1 Study Design	70
3.3.2 Finite Element Modeling	70
3.3.3 Three-Dimensional Spatial Correlation	74
3.3.4 Statistical Analysis	78
3.4 Results	78
3.4.1 Tissue Stress Magnitudes	78

3.4.2 Spatial Correlations	79
3.5 Discussion	84
3.6 Acknowledgements	86
Chapter 4: Spatial Relationship Between Microdamage, Resorption Cavities and Trabecular Surfaces	87
4.1 Abstract	87
4.2 Introduction	88
4.3 Methods	90
4.3.1 Study Design	90
4.3.2 Number, Size and Location of Microdamage	92
4.3.3 Spatial Correlation of Microdamage and Resorption Cavities	94
4.3.4 Statistical Analyses	96
4.4 Results	97
4.5 Discussion	101
4.6 Acknowledgements	105
Chapter 5: Relationship Between Microdamage and Tissue Level Strain	107
5.1 Abstract	107
5.2 Introduction	108
5.3 Methods	109
5.3.1 Study Design	110
5.3.2 Finite Element Modeling	111
5.3.3 Probability of Microdamage at Finite Element Modeled Strain	112
5.3.4 Spatial Correlation of Microdamage and Highly Strained Tissue	113
5.3.5 Statistical Analyses	115
5.4 Results	115
5.5 Discussion	120
5.6 Acknowledgements	123
Chapter 6: Summary and Future Directions	125
6.1 Summary	125
6.1.1 Aim 1	126
6.1.2 Aim 2	127
6.1.3 Aim 3	128
6.1.4 Aim 4	128
6.1.5 Synthesis	129
6.1.7 Strengths	130
6.1.7 Limitations	131
6.2 Future Work	132
6.2.1 Continues Research Avenues	133
6.2.1.1 Material Properties Surrounding Cavities	133
6.2.1.2 Modeling Material Properties of Cancellous Bone	134
6.2.1.3 Microdamage Repair in Cancellous Bone	135
6.2.2 New Research Avenues	136
6.2.2.1 Spatial Relationship Between Microdamage and Structural Features	136
6.2.2.2 Modeling Variations in Cancellous Bone Tissue-level Ductility	137
References	139
Appendix A: Chapter 3 Supplementary Material	170
Appendix B: Chapter 4 Supplementary Material	205

Appendix C: Chapter 5 Supplementary Material  
Appendix D: Rabbit Study Preliminary Material

207  
212

## LIST OF FIGURES

1.1	Hierarchical Structure of Bone	14
1.2	Schematic of Reductions in Modulus During Fatigue Loading of Cancellous Bone	18
1.3	Schematic of Different Forms of Microdamage	22
1.4	Schematic of Extrinsic and Intrinsic Toughening in Bone	22
1.5	Schematic of a Remodeling Event in Bone	24
1.6	Cross-sections of a Young and an Old Vertebra	24
2.1	Example of Limitations of Traditional Bone Histomorphometry	35
2.2	Representative SEM Images of Resorption Cavities	36
2.3	Summary of Resorption Cavity Identification Techniques	40
2.4	Summary of Maximum Resorption Cavity Depth Measurement	43
2.5	Illustration of Resorption Cavity Locations	47
2.6	Distribution of Resorption Cavity Size	48
2.7	Distribution of Resorption Cavity Location	49
2.8	Relationship between Maximum Resorption Cavity Depth and Local Strut Thickness (a) and Resorption Cavity Surface Area (b)	50
2.9	Relationship Between Resorption Cavity Depth and Stress Concentration Factor	62
2.10	Shapes Used to Benchmark Cavity Depth Measurements	65
2.11	Validation of Cavity Depth Measurements	66
3.1	Illustrations of Potential Misalignments During Loading	73
3.2	Schematic of Three-Dimensional Correlation Techniques	77
3.3	Example of Location of High Mechanical Stress in Cancellous Bone	79
3.4	Spatial Correlation Results for Cancellous and Cortical Bone Using the Inflate Algorithm	81
3.5	Spatial Correlation Results for Cancellous and Cortical Bone Using the G(r) Parameter	83
4.1	Diagram Describing the Fatigue Loading for Each Specimen	92
4.2	Hypothetical Normal Distribution of Microdamage Site Size	93
4.3	Schematic of Resorption Cavity Identification	95
4.4	Relationship Between Reduction in Young's Modulus and DV/BV, Number of Large Microdamage Sites and Number of Microdamage Sites	98
4.5	Representative Histogram of the Distribution of Microdamage Site Size in Specimens Loaded to the Secondary and Tertiary Phases of Fatigue Life	99
4.6	Spatial Correlation Results for Microdamage and Resorption Cavities Using the Volume Based Method	100
4.7	Spatial Correlation Results for Microdamage and Resorption Cavities Using the Object Based Method	100
5.1	Illustration of the Overlap of Highly Strained Tissue and Microdamage	114
5.2	Strain Magnitude at Microdamage and away from Microdamage	117
5.3	Probability of Microdamage at Strain Magnitudes	118
5.4	Spatial Correlation Results for Microdamage and Highly Strained	

	Tissue Using the Volume Based Method	118
5.5	Spatial Correlation Results for Microdamage and Highly Strained Tissue Using the Object Based Method	119
5.6	Spatial Correlation Results for All Large Objects vs All Objects	120

## LIST OF TABLES

1.1	Average Mechanical Properties of Human Femoral Cortical Bone	18
1.2	Survey of Mechanical Properties of Human Cancellous Bone	18
2.1	Characteristics of Trabecular Microarchitecture and Resorption Cavities in Human Lumbar Vertebral Trabecular Bone	51
2.2	Measures of Resorption Cavities on Rod-like Trabeculae, Plate-like Trabeculae and Nodes	52
2.3	Correlations Among Measures of Individual Cavities	53
2.4	Correlations Among Measures of Cavities and Trabecular Microarchitecture	56
2.5	Comparisons Between Measures in Current and Previous Studies	59

## CHAPTER 1

### **Introduction**

#### **1.1 *Fracture in Bone***

In the United States alone, over 1.5 million fractures occur annually resulting in a financial burden of over \$19 billion [1-3]. Additionally, in the elderly, fractures lead to an increase in the amount of time spent in nursing facilities by approximately 17% and a decrease in life expectancy of 1.8 years [4, 5]. Fractures fall into two main categories: fractures that follow a sudden traumatic event and fractures that develop over time due to repeated sub-failure loading events. Fractures that occur due to repeated loading events are classified as follows: fatigue fractures and insufficiency fractures [6-10]. Fatigue fractures occur in bones with normal material and structural properties submitted to excessive physical activity. Fatigue fractures occur following intense activity such as military training [6, 11-14]. Insufficiency fractures occur in bones with impaired material and structural properties submitted to normal daily loading. Many osteoporosis-related fracture are insufficiency fractures [6, 15, 16]. Insufficiency fractures tend to occur in regions dominated by cancellous bone (see ***Bone Composition and Architecture***) and the majority of vertebral fractures are insufficiency fractures [17-19].

## **1.2 Bone Composition and Architecture**

Bone is a complex structure with an intricate architecture spanning several length scales (Figure 1.1). Bone consists of 65% mineral and 35% organic matrix by mass [20, 21]. The mineral portion of bone is primarily composed of impure hydroxyapatite [20, 22]. The organic matrix of bone is composed of 90% type I collagen and 10% non-collagenous proteins [20, 23]. The organic matrix is assembled into ordered bundles called fibrils that are stabilized by cross-links that occur between the collagen molecules [24]. The mineral forms between the fibrils and then extends into the organic matrix [22, 24, 25]. Additionally, water plays an important role in the composition of bone tissue, and when bone tissue is dehydrated the mechanical properties drastically change [26-33].

Bone consists of two types of microarchitecture: cortical bone and cancellous bone. Cortical bone is the hard exterior of bones and is the only type of microarchitecture found in the midshaft region of long bones. Cortical bone is dense and has a relatively small porosity (2-5%)[34]. The porosity of cortical bone consists of canals containing blood vessels and nerves that run through the tissue. Haversian canals run longitudinal to the bone and Volkmann canals run transverse to the bone [35]. During remodeling, osteons form around canals and consist of concentric lamellae [20] (see **Bone Remodeling**) . Osteons are delimited from the rest of the tissue by 1-5  $\mu\text{m}$  thick regions called cement lines [36]. Cancellous bone is found in the center of vertebrae and the ends of long bones. Cancellous bone does not contain osteonal canals and instead consists of a network of struts called trabeculae.

Trabeculae consist of lamellae separated by cement lines that form parallel to the long axis and hemi-osteons on the surfaces [20, 37]. Trabeculae can be classified as rod- or plate-like and are oriented longitudinally, transversely, or obliquely to the longitudinal axis of the bone [38]. Typical measurements of cancellous bone microarchitecture include bone volume fraction, number of trabeculae, thickness of trabeculae, separation of trabeculae, degree of anisotropy and structure model index [39]. Degree of anisotropy is a measure of the alignment of the trabeculae, and structure model index is a measure of the proportion of plate-like versus rod-like trabeculae [40, 41].

Bone tissue contains a network of sub-micron scale canals called canaliculi that connect small spaces called lacunae. Osteocytes, the bone cells believed responsible for signaling bone remodeling (see ***Bone Remodeling***), are located in lacunae and the canaliculi contained the cell processes of the osteocytes [42, 43]. Both lacunae and canaliculi are too small to be observed with most imaging techniques and are generally ignored when calculating the stress distribution in bone (see ***Modeling the Distribution of Stress/Strain in Bone***).

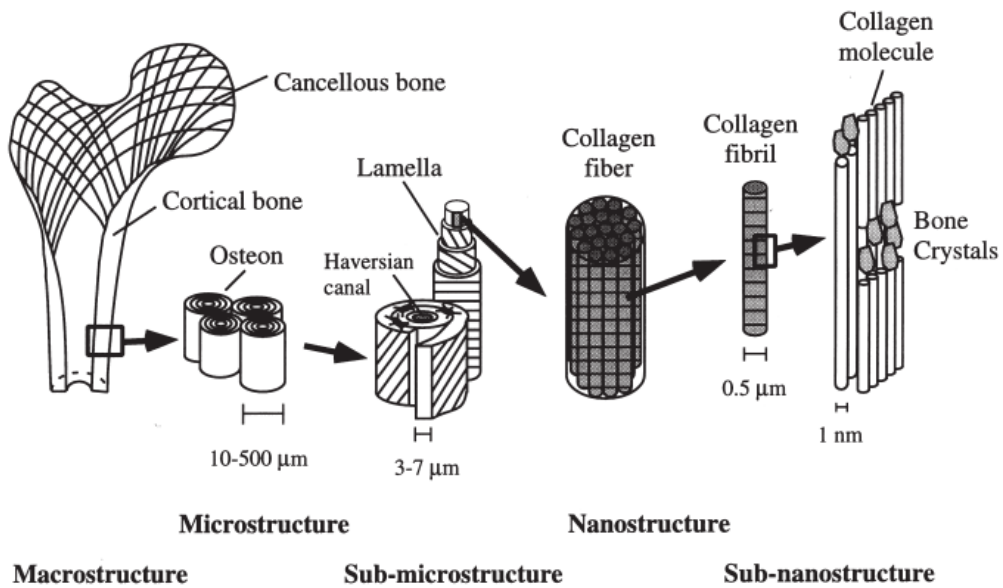


**Figure 1.1** The structure of bone is complicated and varies at many length scales. Image adapted from Rho et al [24].

### 1.3 Mechanical Testing of Bone

The mechanical properties of bone can be measured both at the structural level through whole bone mechanical testing and the material level through tissue-level mechanical testing [44-46]. Whole bone mechanical tests can be used to approximate how the complex structure will react and potentially fail during loading. However, whole bone mechanical tests are highly dependent on specimen size and shape and it is difficult to compare the results from experiment to experiment. Tissue-level mechanical tests are performed on samples of known size and geometry and can be used to calculate material properties.

Structural properties calculated from whole bone tests are stiffness, ultimate load, and energy absorbed to failure. The material properties calculated from tissue-level

tests are modulus, ultimate strength, and work to failure. Whole bone test measures are calculated from the relationship between the load and displacement while tissue-level test measures are calculated from the relationship between the stress and strain. Stiffness and modulus are calculated as the slope of the linear region of the force/displacement and stress/strain curves respectively. Since the relationship between loading and displacement in bone isn't linear, several techniques are used to calculate the slope of the elastic region [44-46]. Ultimate load and ultimate strength describe when the bone or tissue will fail under the applied load. Energy absorbed to failure and work to failure are measures of toughness and are calculated as the area under the force/displacement and stress/strain curves respectively. Additional mechanical tests are performed to assess how bone tissue resists the initiation and growth of cracks [47-52].

Both whole bones and bone tissues are tested using several different loading modalities. Techniques used to test mechanical properties are axial loading, torsional loading and bending. When bone is loaded through bending, both three-point and four-point bending techniques are used. Additionally, tissue-level modulus and hardness can be measured using nanoindentation [53-55], but nanoindentation has been found to have little correlation with whole bone mechanical properties [56]. Differences between nanoindentation results and whole bone mechanical properties are not surprising since nanoindentation measures tissue-level properties while whole bone tests incorporate both bone tissue and voids in the bone tissue.

#### **1.4 Mechanical Properties of Bone**

The mechanical properties of cortical bone vary based on loading direction, tissue age, and mineral density. At the continuum scale, both the modulus and ultimate stress of cortical bone are transversely isotropic. The Young's modulus of cortical bone tissue is larger longitudinal to the primary loading orientation of the whole bone than transverse to the primary loading orientation. Additionally, the Young's modulus is decreased in older tissue and is increased in tissue with a greater degree of mineralization [24, 57-60]. The ultimate strength of cortical bone is also largest longitudinal to the primary loading orientation of the whole bone. Furthermore, the ultimate tensile strength is less than the ultimate compressive strength (Table 1.1) [24, 61]. The fatigue life of cortical bone is affected by the loading orientation. The strain magnitude necessary to initiate damage during cyclic tensile loading is smaller than during compressive loading [62]. Additionally, the fatigue life of cortical bone is dictated by the amount of time the bone is loaded rather than the overall number of cycles that the bone experiences [63]. Both loading orientation and tissue age affect the crack-initiation and crack-growth toughness of cortical bone [52, 64]. In cortical tissue from older donors, both the crack-initiation toughness and crack-growth toughness are greatly decreased [52]. Cortical bone also exhibits viscoelastic properties [65, 66]. The viscoelastic properties are greatly affected by the water that is present in the bone and when the bone is dehydrated the effects disappear [67]. Tissue-level properties of cortical bone have been examined using nano-indentation and interstitial tissue is found to be stiffer than osteonal tissue [68].

In cancellous bone, the mechanical properties are affected by the porosity, trabecular orientation and donor age. The porosity of cancellous bone influences both the continuum level modulus and ultimate strength [65, 69]. Trabecular orientation affects both the continuum level modulus and strength and when combined with the bone volume fraction has been shown to explain most of the variations in those two measures [70]. Furthermore, age related increases in porosity and alterations in trabecular microstructure lead to large reductions in both the continuum level modulus and strength (Table 1.2) [71, 72]. Cyclically loaded cancellous bone exhibits three distinct phases of fatigue (Figure 1.2) [73-75]. The three phases are observed through changes in the stiffness of the specimen. During the primary phase, the stiffness of the specimen decreases rapidly. During the secondary phase, the stiffness decreases slowly. During the tertiary phase, the stiffness decreases rapidly until the failure. The accumulation of microscopic tissue damage is believed to play a role in the reduction in stiffness observed during fatigue [74, 76]. Additionally, the number of cycles to failure of a specimen is influenced by the initial stiffness of the specimen and normalizing the load applied during fatigue by the initial stiffness is a common method for removing variation associated with density [73, 75]. Nano-indentation has shown that the tissue near the center of trabeculae is both stiffer and harder than tissue near the surface of trabeculae [53, 77].

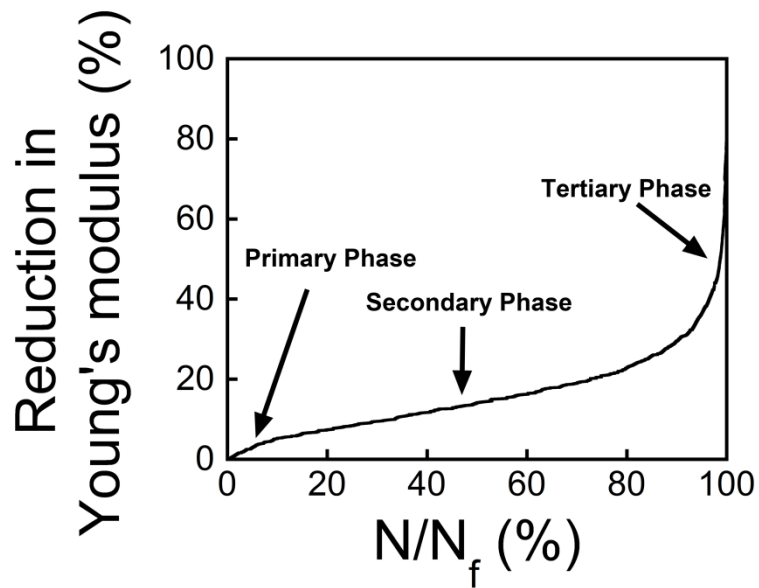


**Figure 1.2** Schematic of the phases of fatigue that occur during cyclic loading of cancellous bone. Image adapted from Lambers [78].

**Table 1.1** Average mechanical properties of human femoral cortical bone with respect to the tissue loading direction. Adapted from Reilly [1].

	Longitudinal	Transverse
Modulus (MPa)	17,000	11,500
Ultimate Tensile Strength (MPa)	133	51
Ultimate Compressive Strength (MPa)	193	68

**Table 1.2** Survey of published mechanical properties of human cancellous bone with respect to donor age and anatomic site. Adapted from Keaveny [2].

Anatomic Site	Age	Modulus (MPa)	Ultimate Strength (MPa)	Reference
Vertebra	15-87	67 ± 5	2.4 ± 1.6	[3]
Tibia	59-82	445 ± 257	5.3 ± 2.9	[4]
Femur	58-85	441 ± 271	6.8 ± 4.8	[5]

### ***1.5 Modeling the Distribution of Stress/Strain in Bone***

While the strains at the surface of cortical bone can be measured using strain gauges, in cancellous bone the tissue-level distribution of stress and strain cannot be directly measured. Finite element modeling is used to approximate the stress and strain distribution present in both cortical and cancellous bone during loading [79-82].

High resolution finite element models of cancellous bone are generated from three-dimensional structural data. Models should be created from images obtained before the tissue is loaded because significant deformation in a loaded sample can affect the predicted stress and strain [83]. High resolution finite element models of cancellous bone are typically generated using eight-noded brick elements. Convergence studies have shown that a minimum of four elements across each trabecula is necessary to properly model the stress/strain distribution in cancellous bone [84-86]. Linear elastic finite element models are the most commonly used and can describe the apparent Young's modulus of cancellous bone. More complex models including heterogeneity in material properties [87, 88] and nonlinearities in both geometry and material properties [89-97] have also been developed.

Finite element models of bone have been used to examine both apparent and tissue-level material properties. At the apparent-level, finite element models of cancellous bone have been used to determine both the apparent modulus and yield strength [98-103]. At the tissue-level, the Young's modulus of cancellous bone can be approximated by combining data from finite element models and data from physically loaded bone specimens [104]. In cortical bone, finite element models have been used

to examine how the tissue-level stresses and strains affect microcrack growth [105-107]. In cancellous bone, finite element models have been used to show that microdamage forms in regions of elevated stress and strain [108-111]. Furthermore, finite element models of cancellous bone have been used to examine how changes in tissue-level material properties affect the apparent level material properties and change the distribution of stress and strain [88, 97]. Whole bone finite element models derived from clinical images are now being used to predict fracture risk in patients [112-114]

### **1.6 Microdamage in Bone**

Microscopic cracks and other tissue damage, collectively known as microdamage, accumulate in both cortical and cancellous bone in-vivo [115-120]. Microdamage falls into three classifications: microcracks, diffuse damage, and microfractures (Figure 1.3). Microcracks are long thin cracks (~100  $\mu\text{m}$ ) that typically form in the interstitial regions of bone and travel along lamellae [121-123]. Diffuse damage is classified as clusters of submicroscopic cracks in the bone where no large cracks are observed [121, 123, 124]. Microcracks tend to form due to compression while diffuse damage tends to form due to tension [121]. Additionally, diffuse damage can form at the tips of microcracks and slow the progress of microcracks by absorbing some of the energy that would go into extending the cracks [120, 125, 126]. Microfractures occur when trabeculae are completely fenestrated and can no longer support mechanical loading. Tang and colleagues have proposed a technique to differentiate whether damage is crack-like or diffuse by measuring the surface area to volume ratio (crack-like damage

having a larger surface area to volume ratio than diffuse-like damage) [127, 128]. However, the surface area to volume ratio is not dimensionless and shows some dependence on damage site size.

The formation of microdamage is detrimental to the mechanical properties of bone although the ability of bone to dissipate energy by creating microdamage prevents brittle fractures [121, 123, 129]. The elastic modulus [78, 130-133] and strength [117, 134] of the bone decrease as microdamage accumulates in cortical and cancellous bone. However, when damage occurs it dissipates energy preventing larger fractures [123].

Several mechanisms exist that prevent the rapid expansion of microdamage that would lead to large fractures (Figure 1.4). In cortical bone, structural features such as the cement lines surrounding osteons will arrest microdamage [135-140]. Two types of toughening mechanisms are responsible for retarding and arresting microdamage growth: intrinsic and extrinsic toughening [141, 142]. Intrinsic toughening mechanisms act ahead of the damage and limit the amount of microdamage that occurs. Some examples of intrinsic toughening mechanisms are microcracking ahead of the damage, fibrillar sliding, and molecular uncoiling. Extrinsic toughening mechanisms act in the wake of the damage and shield the damage from the applied load. Some examples of extrinsic damage are uncracked-ligament bridging, collagen-fibril bridging and constrained microcracking around the damage site [143-146].

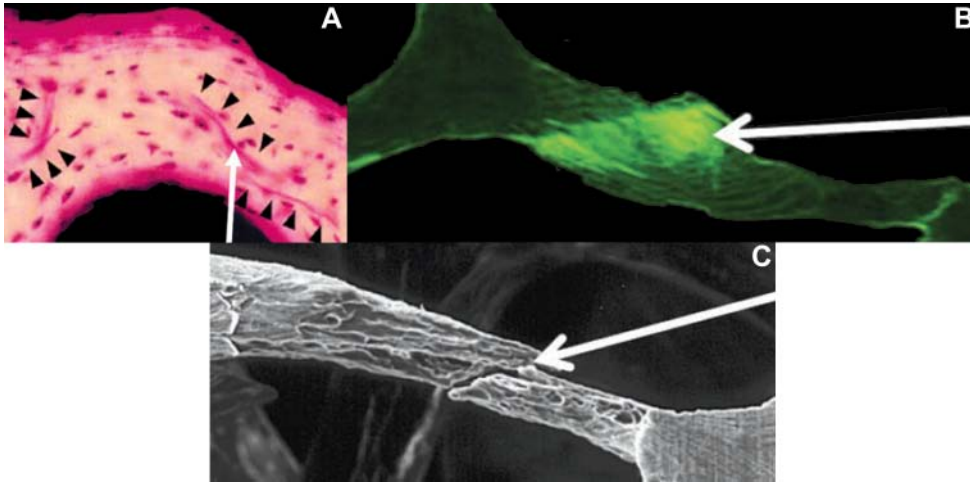


**Figure 1.3** Schematic of different forms of microdamage in bone. Microdamage forms as large cracks called microcracks (A) and clusters of small cracks called diffuse damage (B). A microfracture occurs when enough microdamage accumulates to fenestrate a trabecular strut (C). Image adapted from Burr [121].

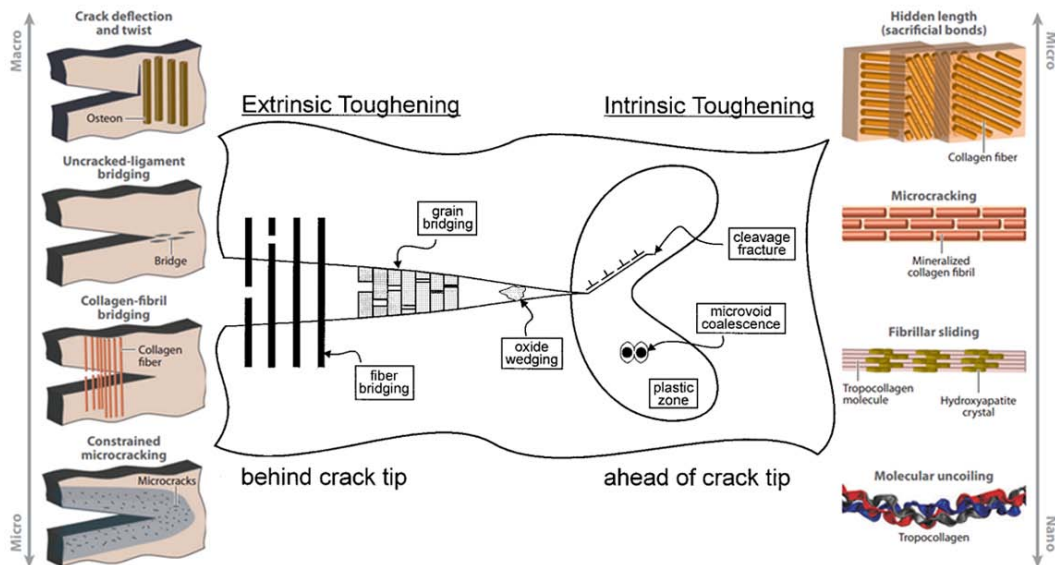


**Figure 1.4** Schematic of extrinsic and intrinsic toughening in bone. Intrinsic toughening acts ahead of the crack tip while extrinsic mechanisms act behind the crack tip. Intrinsic and extrinsic toughening mechanisms act at many structural levels in bone. Image adapted from Ritchie and Launey [141, 142].

Most of our knowledge of microdamage development, accumulation, and repair is derived from research on cortical bone and relatively little is known about how

microdamage forms in cancellous bone. Since the microarchitecture and ultrastructure of cancellous bone differs from that of cortical bone, the manner in which microdamage develops and is repaired may be different than what is known for cortical bone.

### **1.7 Bone Remodeling**

Bone remodeling is a naturally occurring process in which old or damaged bone tissue is replaced with new bone tissue [20, 147]. The bone remodeling cycle involves three types of cells: osteoclasts, osteoblasts and osteocytes [20, 148]. Osteoclasts remove the old or damaged bone through a process called resorption [42, 43]. Osteoblasts then deposit new matrix that mineralized over time to replace the material that was removed by the resorption cavities [42, 43] (Figure 1.5). Osteocytes are mature osteoblasts that are embedded in osteoid and are believed to trigger the remodeling process [42, 43]. In healthy bone, remodeling is a beneficial process that enhances the material properties of the bone and decreases the risk of overall fracture [147, 149]. Animal models have shown that microcracks are removed from cortical bone through the remodeling process [150-152]. Furthermore, when remodeling is suppressed, there is a significant increase in the amount of damage present in cortical bone [153, 154]. Osteocyte apoptosis has been suggested as a mechanism that triggers the targeted remodeling that removes microcracks [155, 156]. Diffuse damage does not trigger osteocyte apoptosis [157] and appears to heal through a mechanism other than remodeling; however, the mechanism is not clear yet [158].

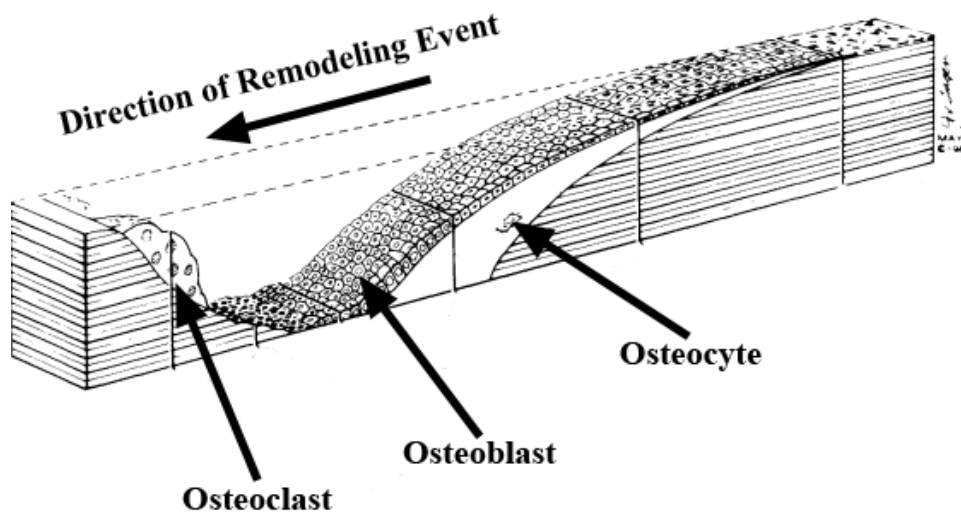


**Figure 1.5** Schematic of a remodeling event in bone. The remodeling event is progressing from right to left. After the osteoclast removes old or damaged bone, osteoblasts lay un-mineralized osteoid. Through the remodeling process, osteoblasts are trapped in the osteoid and differentiate into osteocytes which are believed to trigger remodeling and modeling events. Image adapted from Eriksen [159].

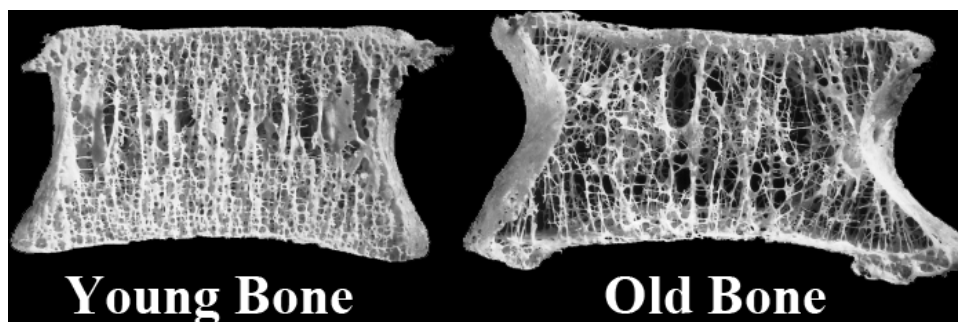


**Figure 1.6** Cross-sections of a young and an old vertebra. The young bone has a thicker cortical shell and a denser cancellous network. Image adapted from Mosekilde [160].

In cortical bone, remodeling events result in the creation of an osteons [20, 42].

In osteons, the bone tissue is removed cylindrically and then replaced resulting in a

gradient of mineralized tissue from the center to the edge of the osteon [54, 161].

In cancellous bone, remodeling occurs on the surface of trabeculae. Since cancellous bone has a larger surface area to volume ratio than cortical bone, remodeling has a larger influence on the structure of cancellous tissue than cortical tissue [20, 42]. As remodeling occurs at the surface of cancellous bone, the youngest tissue in cancellous bone is located at the surface of trabeculae while the oldest tissue is located near the center of trabeculae [52, 53, 77]. Additionally, resorption cavities are created during the resorption phase of remodeling and are expected to act as stress concentrations [162-164]. As people age and during diseases such as osteoporosis, osteoclasts remove more bone tissue than osteoblasts deposit resulting in a net loss of bone volume and a greater risk of whole bone fracture [1, 160, 165-169] (Figure 1.6). When remodeling is altered, the resorption cavities are not completely filled resulting in a general thinning of the cancellous bone.

Some studies have suggested that blood serum measurements for remodeling are better indicator of fracture risk than structural measures such as BMD [170-173]. While the mechanism behind bone remodeling affecting fracture risk isn't known, resorption cavities have been proposed as a mechanism [162]. Computational models have shown that the presence of resorption cavities [163, 164, 174] on individual trabeculae act as stress concentrations and when resorption cavities are located at high stress regions they have a large effect on cancellous bone strength [175]. If so, resorption cavities would be preferential locations of microdamage.

## 1.8 *Imaging Bone*

Bone structure, microdamage, and resorption cavities are analyzed using two-dimensional and three-dimensional techniques. Two-dimensional imaging techniques include light and fluorescent microscopy of thin sections of bone tissue [176]. During two-dimensional imaging, microdamage is stained using basic fuchsin and fluorochromes. Three-dimensional imaging techniques include micro-computed tomography, confocal microscopy, and serial milling [176-178]. During three-dimensional imaging, microdamage is stained using fluorochromes and heavy metals such as lead uranyl acetate. Microdamage stains work by attaching to free surfaces of the bone structure, including those resulting from microscopic and submicroscopic cracks. Fluorochrome stains are also used to label microdamage [134, 179-183]. Basic fuchsin and heavy metal stains can only be used ex-vivo [122, 184, 185]. Since multiple fluorochrome stains can be utilized simultaneously and imaged at different wavelengths, sequential fluorochrome stains can be utilized to mark damage at different time points [136, 183, 186, 187]. Additionally, a specimen can be loaded, stained, and loaded again to determine whether the presence of microdamage affects the structural properties of a specimen [134]. Currently no staining techniques exist to identify resorption cavities and resorption cavities must be identified manually by looking for scalloped regions of the bone [188, 189] (see *Chapter 2*).

## **1.9 Thesis Aims**

Over 1.5 million fractures occur annually in the United States, resulting in medical costs of over \$19 billion each year [1-3]. Insufficiency fractures occur in skeletal regions dominated by cancellous bone [190, 191]. In cancellous bone, the accumulation of microdamage results in a loss of biomechanical performance [78, 134] and is believed to play a role in whole bone fractures. However, relatively little is known about the how microdamage accumulates in cancellous bone or how cancellous bone structure affects the development of microdamage.

In bone tissue, the development of microdamage is driven by the tissue-level mechanical environment and is influenced both by the load distribution throughout the microarchitecture and tissue-level material properties [142]. However, the complicated microarchitecture of cancellous bone prevents direct measurement of the tissue-level mechanical environment. Finite element models of cancellous bone can be used to approximate the distribution of stress/strain and have been used to predict apparent level mechanical properties following loading [95, 192, 193]. However, the capability finite element models to predict the location of microdamage based on regions of high tissue strain has not been validated against physically-loaded specimens. Additionally prior to this dissertation, no three-dimensional spatial correlation techniques had been developed to examine the proximity of resorption cavities, regions of elevated tissue strain, and microdamage.

Additionally, finite element models are not typically created from images obtained at resolutions capable of incorporating structural aspects of cancellous bone such as

resorption cavities. Resorption cavities are believed to act as stress concentrations in cancellous bone and play a role in whole bone failure [162, 164, 194]. However, before the work in this dissertation no three-dimensional measurements of resorption cavities shape and size had been made, and previous studies examining the effects of resorption cavities have assumed idealized sizes and shapes of resorption cavities. Furthermore, no spatial relationship has been seen between resorption cavities and microdamage in cancellous bone loaded monotonically [183]. As cancellous bone is cyclically loaded, more microdamage accumulates [78] and the effects of local stress concentrations should be more pronounced.

While the highest stresses are expected to be located at trabecular surfaces and resorption cavities, no studies have examined if microdamage preferentially forms near highly stressed regions or if another aspect of bone tissue directs microdamage accumulation. Therefore, the aims for this dissertation are: 1) characterize the size and location of resorption cavities in cancellous bone; 2) develop three-dimensional spatial correlation techniques; 3) characterize the size, number and the location of microdamage in cancellous bone with respect to trabecular surfaces and resorption cavities; 4) determine how well linear elastic finite element models predict the location of microdamage in cancellous bone.

### **1.9.1 *Aim 1: Characterize the Size and Location of Resorption Cavities in Cancellous Bone***

Resorption cavities are believed to act as stress concentrations in cancellous

bone [162, 164]. However, finite element models are created from three-dimensional images of cancellous bone and the images are not typically obtained at a high enough resolution to include resorption cavities. Resorption cavities may not create significant stress concentrations if cavities are shallow or if cavities are located in regions of the bone not experiencing loading. Currently no studies have characterized the size or location of resorption cavities in human bone in three-dimensions. In this aim, the size and location of resorption cavities in human vertebral bone were characterized. Three-dimensional images were acquired of cylinders of cancellous bone from the fourth lumbar vertebra using serial milling at a resolution for which individual resorption cavities could be identified ( $0.7 \times 0.7 \times 5 \mu\text{m}$ ) [195, 196]. The cavity depth, surface area, volume, depth/trabecular thickness, and number of cavities per unit tissue volume were calculated. Additionally, the percentage of cavities on different types of trabeculae (rod-like, plate-like and nodes) and the percentage of cavities on different orientations of trabeculae (longitudinal, transverse, and oblique) were calculated. The results of this aim were published in Bone [188].

### **1.9.2 *Aim 2: Develop Three-dimensional Spatial Correlation Techniques***

To determine the spatial relationship between microdamage and highly strained regions of the cancellous microarchitecture, three-dimensional spatial correlation techniques were necessary. Characterizing the spatial correlation between sets of objects of arbitrary size and shape within a three-dimensional image is challenging; therefore, we developed several three-dimensional spatial correlation

techniques. The spatial correlation techniques were based on two-dimensional techniques used for stereology [197-199]. The spatial correlation techniques developed in this aim were used to check the validity of using finite element models to predict the locations of bone formation when using the rodent tail loading model. Finite element models of the rodent tail loading model assume axial loading; however, when loading live animals small misalignments are unavoidable. Therefore, a parametric analysis of the effects of angular and translational misalignments during in-vivo loading was performed by creating finite element models of the eighth caudal vertebra of Sprague Dawley rats. Locations of tissue with high stress were defined as tissue with von Mises stress exceeding the 90<sup>th</sup> percentile, a conservative estimate of tissue stress that would stimulate bone formation [200, 201]. The results of this aim were presented at the Northeast Bioengineering Conference and Orthopaedic Research Society annual meetings and were published in the Journal of Biomechanics [202].

### ***1.9.3 Aim 3: Characterize Number, Size, and Location of Microdamage Sites in Cancellous Bone Following Fatigue Loading***

In cancellous bone, microdamage is expected to form at locations of the highest stress/strain [89]. The stress and strain in cancellous bone are expected to be highest at the surfaces of trabeculae [88] and resorption cavities that form on the surface of trabeculae are expected to act as stress concentrations [162, 164, 194]. However, the oldest and stiffest tissue is located near the center of trabeculae [53, 77, 203], and the only study that has examined the relationship between resorption cavities

and microdamage was done following monotonic loading [183]. The effects of high stress regions will be more pronounced and have a larger effect on damage accumulation following cyclic loading. Thus the aim of this study was to determine where in cancellous bone microdamage forms following cyclic loading. In this aim, cylinders of cancellous bone were cyclically loaded to different points in their fatigue lives. The volume, number and location of microdamage were examined with respect to the amount of loading that was applied. Specifically, the proximity of microdamage to the surface of trabeculae and resorption cavities were examined. The results of this aim were presented at the World Congress of Biomechanics and Orthopaedic Research Society annual meetings and were published in Bone [204].

#### **1.9.4 *Aim 4: Determine how well Linear Elastic Finite Element Models Predict the Location of Microdamage in Cancellous Bone***

Finite element models of cancellous bone are used to examine the effects of variations in tissue-level material properties [102] and can be used to predict whole bone failure [205]. However, the locations at which tissue-level yield is predicted to occur in models have not been validated against where tissue yield occurs in physically-loaded specimens. Previous studies have determined that microdamage forms at higher than average strains [108, 206], but the ability of finite element models to predict the location of microdamage has not been examined. Additionally, no studies have examined the relationship between tissue strain and microdamage in cancellous bone loaded in tension. Microdamage accumulation in cancellous bone is

greater following tensile loading than following compressive loading [183]. Therefore, the purpose of this aim was to determine how well linear elastic finite element models can predict the location of microdamage in cancellous bone loaded in compression or tension. The results of this aim were presented at the Orthopaedic Research Society annual meeting.

## CHAPTER 2

### **Three-dimensional Morphology of Resorption Cavities**

This chapter was published in *Bone* in 2012 in Volume 51 (pgs. 28-37). The article is titled “Three-dimensional characterization of resorption cavity size and location in human vertebral trabecular bone” by Goff MG, Slyfield CR, Kummari SR, Tkachenko EV, Yi YH, Jekir MG, Keaveny TM, and Hernandez CJ and is reprinted here with permission of Elsevier.

#### **2.1 Abstract**

The number and size of resorption cavities in cancellous bone are believed to influence rates of bone loss, local tissue stress and strain and potentially whole bone strength. Traditional two-dimensional approaches to measuring resorption cavities in cancellous bone report the percent of the bone surface covered by cavities or osteoclasts, but cannot measure cavity number or size. Here we use three-dimensional imaging (voxel size 0.7 X 0.7 X 5.0  $\mu\text{m}$ ) to characterize resorption cavity location, number and size in human vertebral cancellous bone from nine elderly donors (7 male, 2 female, ages 47-80 years). Cavities were  $30.10 \pm 8.56 \mu\text{m}$  in maximum depth,  $80.60 \pm 22.23 \times 10^3 \mu\text{m}^2$  in surface area and  $614.16 \pm 311.93 \times 10^3 \mu\text{m}^3$  in volume (mean  $\pm$  SD). The average number of cavities per unit tissue volume (N.Cv/TV) was  $1.25 \pm$

0.77 mm<sup>-3</sup>. The ratio of maximum cavity depth to local trabecular thickness was 30.46 ± 7.03 % and maximum cavity depth was greater on thicker trabeculae (p < 0.05, r<sup>2</sup> = 0.14). Half of the resorption cavities were located entirely on nodes (the intersection of two or more trabeculae) within the trabecular structure. Cavities that were not entirely on nodes were predominately on plate-like trabeculae oriented in the cranial-caudal (longitudinal) direction. Cavities on plate-like trabeculae were larger in maximum cavity depth, cavity surface area and cavity volume than cavities on rod-like trabeculae (p < 0.05). We conclude from these findings that cavity size and location are related to local trabecular microarchitecture.

## ***2.2 Introduction***

The amount of bone remodeling in the body has been associated with fracture risk independent of bone mineral density [170, 207]. The association between bone remodeling and fracture risk is believed to be due to the biomechanical effects of cavities formed during the remodeling process [208, 209]. Cavities formed during remodeling, referred to here as resorption cavities, may act as stress risers and promote microscope tissue damage and whole bone failure. However, like any stress riser, the mechanical effects of a cavity depend on cavity size and location within the microarchitecture.

Techniques for measuring resorption cavity depth, surface area and location in human cancellous bone are limited. The percent of bone surface area covered by cavities in cancellous bone can be measured in two-dimensional histology sections as

percent eroded surface (ES/BS) or osteoclast surface (Oc.S/BS). However, two-dimensional histology sections cannot be used to identify individual cavities due to the complex shapes of cavities and trabecular bone (Figure 2.1) [210, 211]. Measures of average maximum resorption cavity depth within a specimen (erosion depth, E.De) can be performed in two-dimensional sections by counting lamellae [189, 212] or by estimating the pre-resorbed surface in a two-dimensional section [213, 214]. However, the techniques do not account for cavity morphology out-of-plane, are limited to only a few surfaces in each section (potentially generating a sampling bias) and/or require extensive training to achieve repeatable results [215]. Scanning electron microscopy (SEM) has been used to visualize individual resorption cavities in human cancellous bone [216-218] (Figure 2.2), but the method provides only rough estimates of cavity size because images collected in this manner cannot measure out-of-plane depth on the curved surfaces of cancellous bone (SEM can be used to measure cavity depth on flat surfaces in vitro [219, 220]).

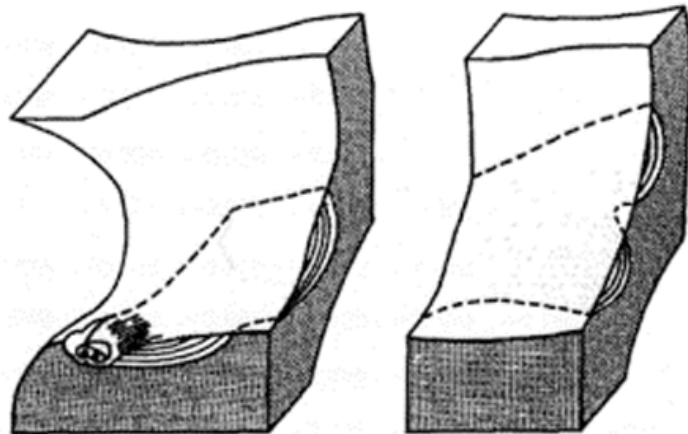


**Figure 2.1** Traditional bone histomorphometry cannot be used to measure the number or size of remodeling events or resorption cavities [211]. Although only a single remodeling event is present, it may appear as one or two profiles. Reprinted from [210], with permission from Elsevier.

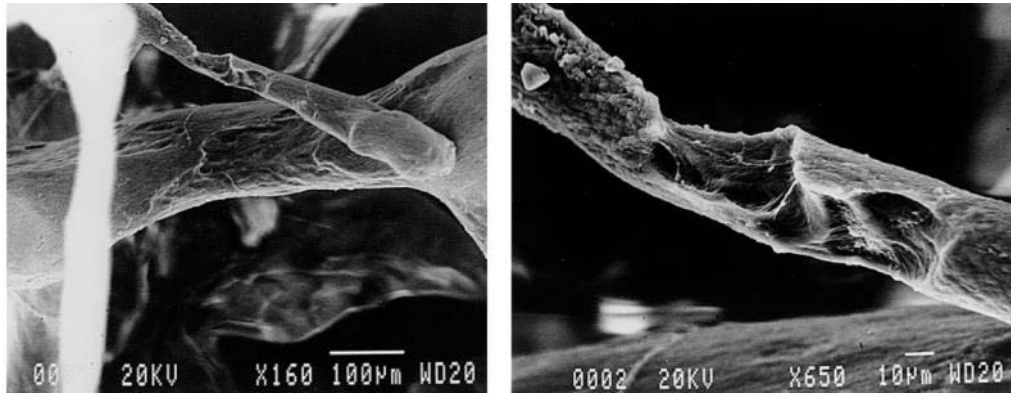


**Figure 2.2** Scanning electron microscopy (SEM) can visualize individual resorption cavities in cancellous bone but only provides estimates of cavity size because out-of-plane depth cannot be determined. Reprinted from [217], with permission from Elsevier.

Due to the technical limitations mentioned above, it is not known how the breadth and depth of individual resorption cavities vary within human cancellous bone. Additionally, to our knowledge, measures of resorption cavities (eroded surface and erosion depth) in human cancellous bone have been limited to iliac crest biopsies [221] and have not been applied to regions of the skeleton that are prone to age-related fracture such as the vertebrae. It is not known if resorption cavities occur preferentially on rod-like or plate-like trabeculae or on nodes in the trabecular microarchitecture (the intersection of two or more trabeculae). Nor is it known if resorption cavities are located preferentially on trabeculae of a certain orientation (longitudinal, oblique or transverse to the primary structural orientation). Stress distributions in cancellous bone have been shown to differ between rod-like and plate-like trabeculae and on trabeculae oriented in longitudinal, oblique and transverse directions [110, 222], suggesting that the biomechanical importance of cavities may depend on their location within the trabecular microarchitecture as well as their size and shape. For example, it has been argued that resorption cavities may not have an

important biomechanical effect unless they are located on vertical trabeculae with long spans (so called “unsupported trabeculae”) [208, 209]. It is also not known how cavity depth is related to the thickness of the trabeculae upon which they form. Theoretical models suggest that the ratio of cavity depth to thickness can greatly influence stress concentrations associated with resorption cavities [223].

The long term goal of the current work is to understand how bone remodeling influences bone strength and fracture risk independent of bone mineral density and bone mass. In this study, we provide the first, three-dimensional characterization of the number, size and shape of resorption cavities in human vertebral cancellous bone. Specifically, we determine: 1) The depth, surface area and volume of individual resorption cavities; and 2) the relationship between maximum resorption cavity depth, surface area, local trabecular thickness, trabecular type (rod-like, plate-like, node) and trabecular orientation (longitudinal, oblique, transverse).

## ***2.3 Materials and Methods***

### ***2.3.1 Image Acquisition and Processing***

Cylinders of human vertebral cancellous bone (8 mm diameter, 15 mm in height) oriented in the cranial-caudal direction were collected from vertebral bodies from nine individuals (L4, 7 male, 2 female, 47-80 years of age,  $70 \pm 10$ , mean  $\pm$  SD). The donors had no history of metabolic bone disease and displayed no obvious

vertebral deformities. The specimens were part of a larger biomechanical study and had previously been submitted to uniaxial compression to apparent yield followed by unloading. The central 5 mm of each specimen length was embedded undecalcified in methyl-methacrylate. Subsequently, three-dimensional images of each specimen were acquired using serial milling [224]. Serial milling is an automated imaging approach in which five micrometers are milled away from the top of the specimen and images of the newly exposed block face are collected. The approach has been described in detail in prior publications [195, 225]. In our implementation of serial milling, fluorescent light images of bone were acquired using UV excitation/emission and achieved voxel sizes of 0.7 X 0.7 X 5.0  $\mu\text{m}$  [195]. Raw images collected using this resolution consist of 800 transverse cross-sections, each consisting of a 6 X 6 mosaic of images (86,400 images total per specimen, occupying 691 GB of memory). We have previously demonstrated that an in-plane voxel size of 1.4  $\mu\text{m}$  or smaller is required to reliably detect individual resorption cavities [226]. Image processing and analysis were performed using custom software written for use with Matlab (Mathworks, Natick, MA, USA) and scripts written for use with Amira (version 5.3 Visage Imaging, San Diego, CA, USA).

### ***2.3.2 Identification of Resorption Cavities in Three-Dimensional Images***

As there are no fluorescent markers of resorption cavities compatible with the serial milling approach, resorption cavities were detected and traced manually by a trained observer. To reduce labor requirements associated with manual tracing, only a

subset of the specimen was examined using the following sampling approach: Three transverse cross-sections, each 1.5 mm from one another were selected in a systemic random manner (Figure 2.3A). The eroded surface (ES/BS) of the whole specimen was determined using line intersection counting with a grid spacing of 200  $\mu\text{m}$  (Figure 2.3B). Eroded surfaces were identified as scalloped defects or crenated surfaces on the trabecular surface in the two-dimensional images.

To obtain three-dimensional measures of individual cavities, the observer first noted the location of each eroded surface profile within the cross-section (shown as squares on Figure 2.3C and at a higher magnification in Figure 2.3D). A three-dimensional rendering of the region of bone surrounding each of the eroded surface profiles was generated to allow the observer to visualize the entire resorption cavity in three-dimensions (Figure 2.3E). The observer then traced the entire surface of each cavity in the three-dimensional image using the lasso tool in Amira (version 5.3 Visage Imaging, San Diego, CA, USA (Figure 2.3F) [226]. The boundaries of the eroded surface were confirmed by visualization of the scalloped or crenated surface in cross section (Figure 2.3D). A total of 206 cavities (15-34 cavities per specimen) were manually identified and submitted to automated three dimensional measurement.

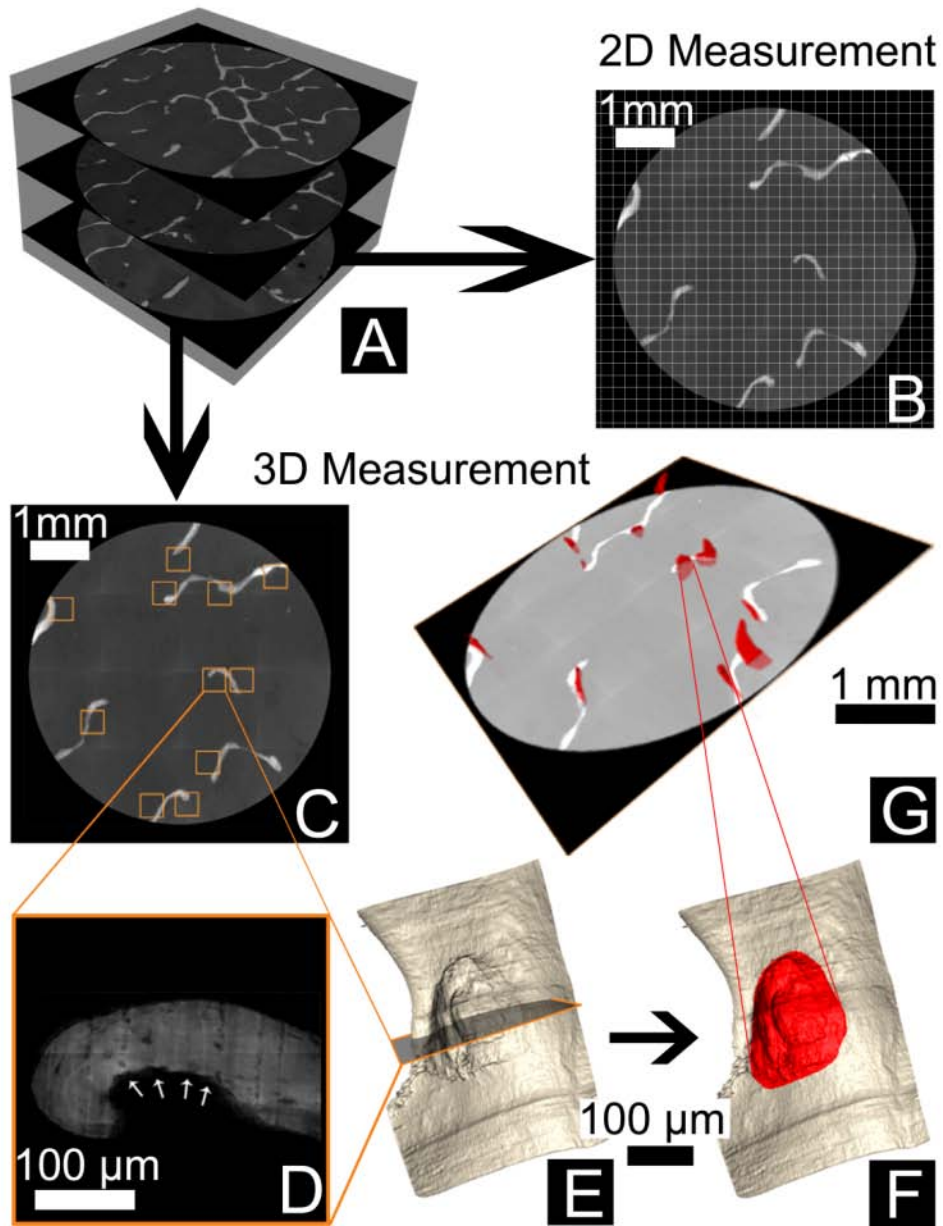


**Figure 2.3** Resorption cavities were sampled in the following manner: (A) Three transverse cross-sections were collected from each specimen. (B) Two-dimensional measures of eroded surface (ES/BS) were determined using the line intersection method with a grid size of 200  $\mu\text{m}$ . Three-dimensional measures of cavities were then determined by first (C) Identifying all eroded surfaces within each cross-section (squares). (D) The eroded surface observed is illustrated (arrows). (E) A three-dimensional image surrounding each eroded surface profile was then generated for the observer. (F) The observer then traces the cavity in the three-dimensional image. (G) Cavities identified in each cross-section were then measured in three-dimensions using automated software.

### ***2.3.3 Automated Measures of Cavity Size in Three-Dimensional Images***

Custom software written for Amira and Matlab was used to automatically measure surface area, maximum cavity depth and cavity volume. The eroded surface traced manually (see above) was used to measure the surface area of each cavity. To measure maximum cavity depth a three-dimensional thin plate smoothing spline was fit across the surface of each cavity to estimate the ‘pre-resorbed’ bone surface. A thin plate smoothing spline is a three-dimensional version of a cubic spline that is commonly used in image processing to cover voids on surface renderings [227, 228]. The bone surface within 50  $\mu\text{m}$  surrounding the edge of each resorption cavity was used to generate the curve fit (Figure 2.4A-C). A three-dimensional curve fit spanning the cavity was generated (the ‘tpaps’ function in Matlab). The spline fit used Lagrangian end conditions such that the slope of the spline matched the slope of the three-dimensional bone surface surrounding each cavity (Figure 2.4D). Cavity depth was determined at every point on the eroded surface as the minimum distance between the eroded surface and the pre-resorbed surface (Figure 2.4E). The maximum cavity depth was then determined for each cavity. Benchmarking studies suggest that the approach provides cavity depth measures within 12% of the actual values in test shapes (Supplementary Material). Volume per cavity was determined as the volume enclosed by the ‘pre-resorbed’ bone surface and the eroded surface (black region in Figure 2.4E) [229]. Additionally, estimates of the average number of cavities per unit bone surface ( $N.Cv/BS$ ) and total volume occupied by cavities ( $Tt.Cv.V/BV$ ) were estimated using the following relationships:

$$\text{Number of Cavities (N.Cv/BS)} = (\text{ES/BS}) / (\text{BS/Cv}), \quad (1)$$

$$\text{Volume Occupied by Cavities (Tt.Cv.V/BV)} = \text{Cv.V} / (\text{BS/Cv}) \times (\text{ES/BS}) \times (\text{BS/BV}), \quad (2)$$

where BS/Cv is the average bone surface per cavity and Cv.V is the mean volume per cavity. The abbreviation BS is the bone surface and BV is the bone volume in the specimen, both of which were measured directly in the three-dimensional image by coarsening to a voxel size of 10.6 X 10.6 X 10.0  $\mu\text{m}$  and importing into BoneJ (bonej.org) [230]. Additionally, traditional three-dimensional measures of trabecular microarchitecture were measured (bone volume fraction, Bone Surface to Bone Volume Ratio, trabecular thickness, trabecular separation, degree of anisotropy, structure model index, connectivity density).

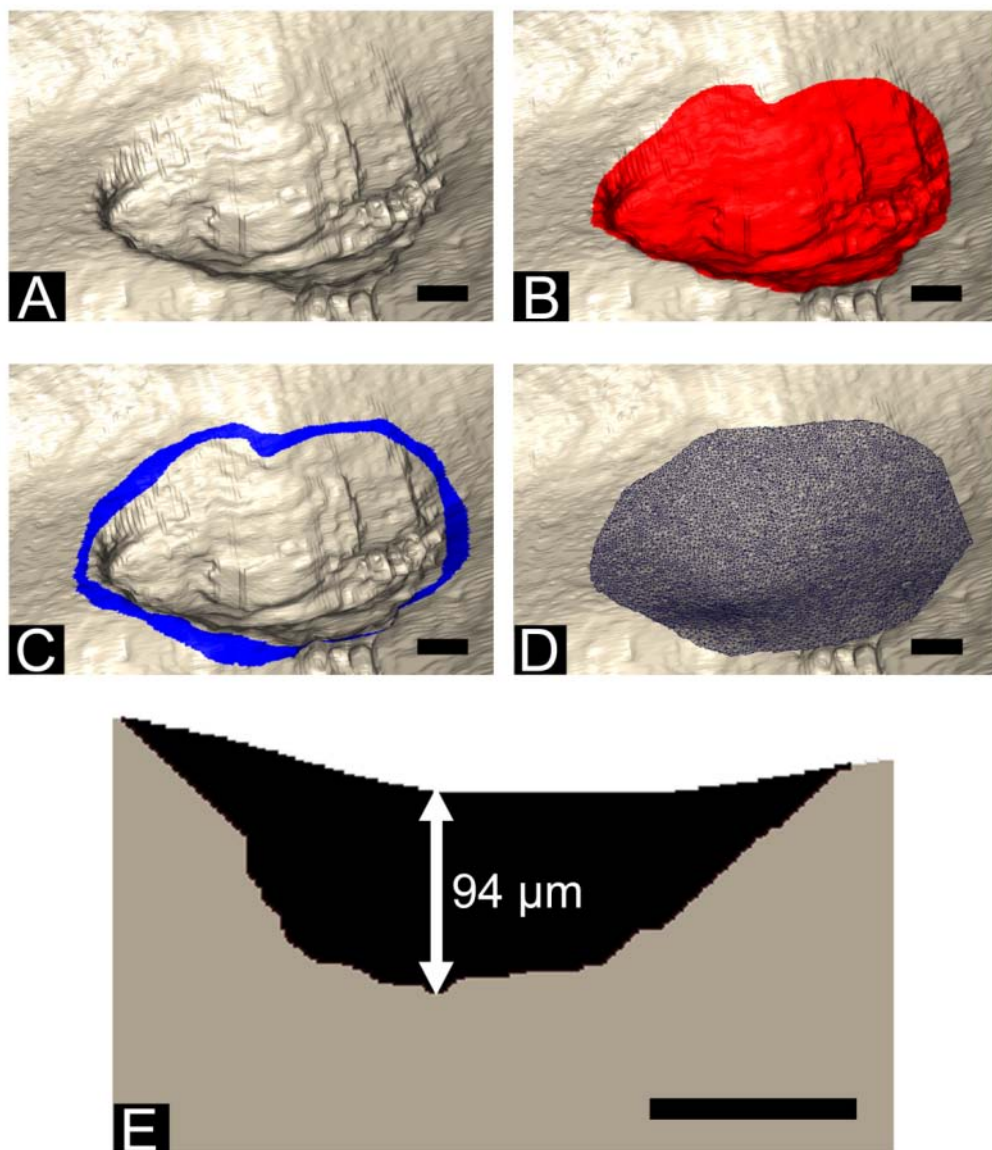


**Figure 2.4** (A) A cavity on the trabecular bone surface detected as described in Figure 2.3 is shown. (B) The cavity was manually traced in the three-dimensional image using Amira. (C) The automated measurement software then identified the bone surface within 50  $\mu\text{m}$  from the edge of the cavity. (D) A thin plate smoothing spline was fit to the surface area surrounding the cavity (shown in C) and used to estimate the “pre-resorbed” surface. (E) The maximum cavity depth was measured as the maximum distance between the spline fit and the eroded surface of the cavity. The cavity shown has a maximum cavity depth of 94  $\mu\text{m}$  (mean maximum cavity depth is reported in Table 2.1). All scale bars represent 100  $\mu\text{m}$ .

### **2.3.4 *Determination of Cavity Location***

Each resorption cavity traced by the observer was reviewed to assess local trabecular morphology. The observer manually measured the local thickness of the trabecula (referred to here as sTb.Th,  $\mu\text{m}$ ) as the maximum distance between the ‘pre-resorbed’ bone surface and the opposing side of the trabecula (performed with the 3D length measurement tool in Amira). Additionally, each cavity was characterized as being on a rod-like trabecula, plate-like trabecula and/or a node (where two or more trabeculae meet). When appropriate, a cavity was characterized as being both on a node and on a rod-like trabecula or both on a node and on a plate-like trabecula. The angle of each trabecula relative to the primary trabecular orientation (i.e. cranial-caudal direction),  $\phi$ , was determined (using the 3D angle measurement tool in Amira). Trabeculae were characterized as longitudinal ( $0^\circ < \phi \leq 30^\circ$ ), oblique ( $30^\circ < \phi \leq 60^\circ$ ) or transverse ( $60^\circ < \phi \leq 90^\circ$ ) [231].

### **2.3.5 *Statistical Analyses***

The average and median cavity sizes across all nine specimens were determined. Additionally, analyses of the distribution of cavity size were performed. Since measures of cavity size were not normally distributed, the median, 25<sup>th</sup> and 75<sup>th</sup> quartiles are used to characterize the results. A Kruskal-Wallis non-parametric ANOVA and a Wilcoxon post-hoc test were used to identify differences in microarchitecture or cavity size relative to location (rod-like, plate-like, node,

trabecular orientation). Correlation analysis was used to determine the relationships among measures of cavities and trabecular microarchitecture. Statistical analyses were implemented using JMP (version 9.0, ImageMagick Studio LLC, Cary, NC, USA).

## **2.4 Results**

Resorption cavities were much broader than they were deep (Figure 2.5A-F). Resorption cavities were observed on plate-like trabeculae (Figure 2.5A,B), rod-like trabeculae (Figure 2.5C,D) and nodes within the trabecular microarchitecture (Figure 2.5E,F). Resorption cavities that fenestrated plate-like trabeculae were also observed (Figure 2.5G,H).

The average number and size of the resorption cavities in the nine specimens are summarized in Table 2.1. Cavities from all nine specimens were pooled to characterize the range of cavity shape. Maximum cavity depth ranged from 4.90 to 116.73  $\mu\text{m}$  (Figure 2.6). The ratio of maximum cavity depth to local trabecular thickness ranged from 4.61 to 90.34% (Figure 2.6). Cavities on plate-like trabeculae displayed greater maximum cavity depth and surface area than those on rod-like trabeculae ( $p < 0.05$ , Table 2.2). No differences in maximum cavity depth or surface area were observed among cavities located on longitudinal, oblique or transverse trabeculae. The maximum cavity depth was positively correlated with local trabecular thickness and with cavity surface area but the relationships were not predictive ( $p < 0.05$ ,  $r^2 = 0.14$  for local trabecular thickness,  $r^2 = 0.27$  for cavity surface area, Table 2.3, Figure 2.8). Measures of cavity size were not correlated with traditional measures of

trabecular microarchitecture (Table 2.4).

A total of 72.9% of all resorption cavities measured in the study were in contact with nodes within the trabecular structure (Figure 2.7A). Cavities that were not entirely on nodes were more commonly located on plate-like trabeculae than on rod-like trabeculae (Figure 2.7A) and were most often on longitudinal trabeculae (trabeculae aligned with the primary direction of the trabecular microarchitecture) (Figure 2.7B).

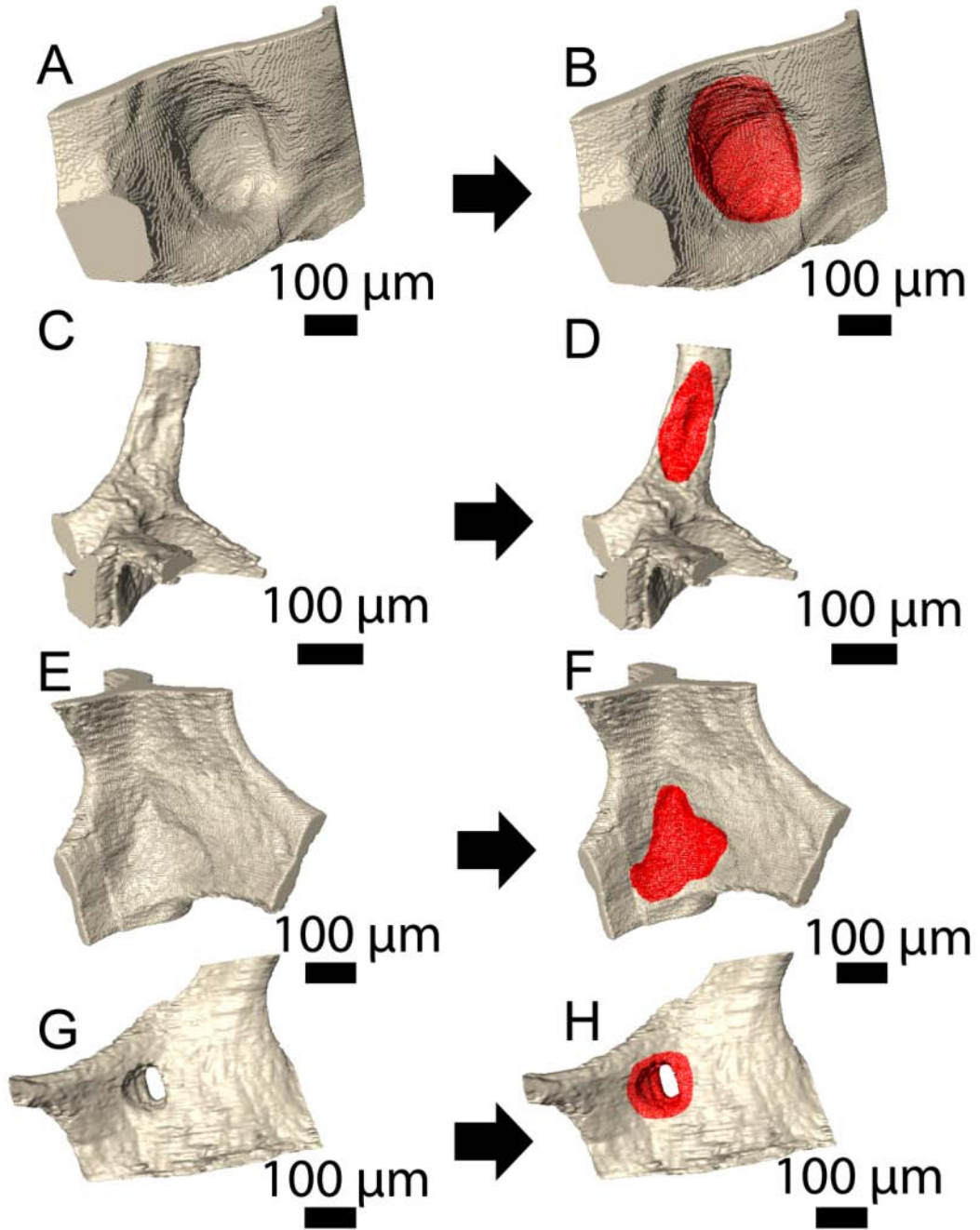


**Figure 2.5** Resorption cavities were observed on plate-like trabeculae (A-B), rod-like trabeculae (C-D), nodes (E-F) and fenestrations (G-H).

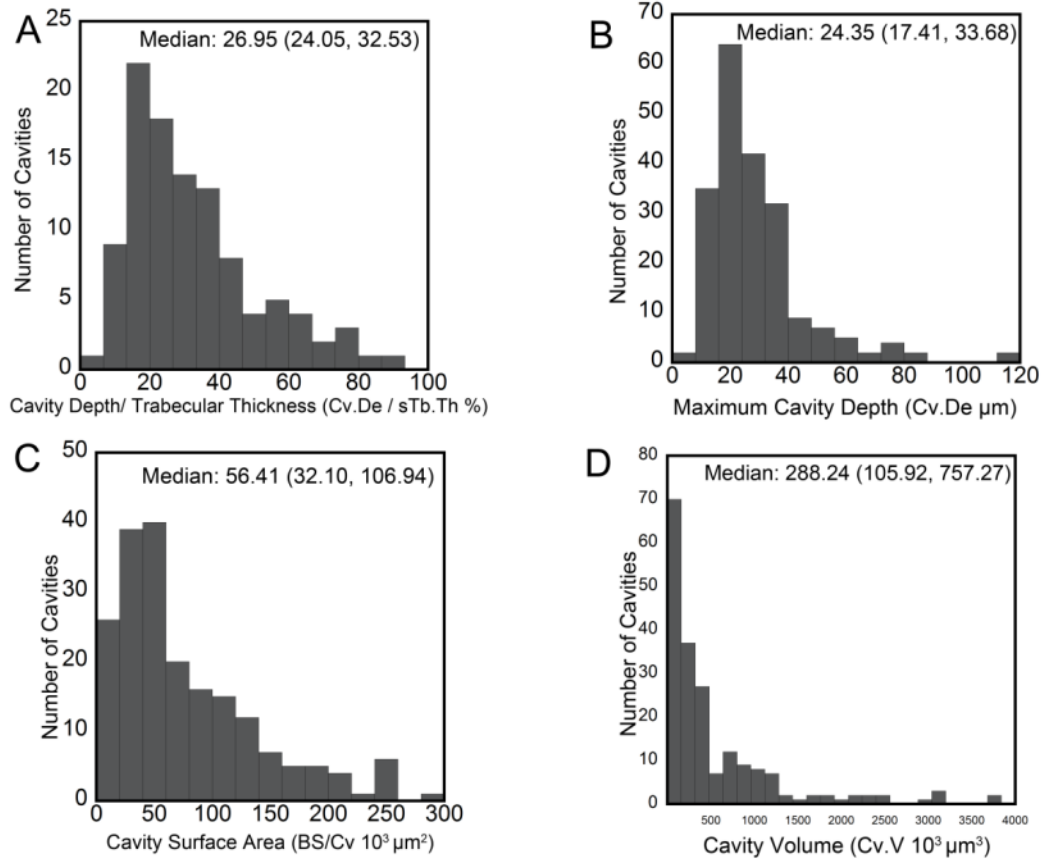


**Figure 2.6** The distribution of cavity size across the entire study is shown (cavities from all specimens pooled) for (A) Maximum cavity depth/local trabecular thickness, (B) maximum cavity depth, (C) cavity surface area and (D) cavity volume.

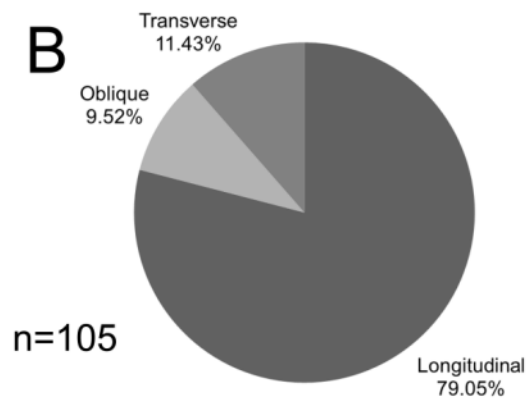
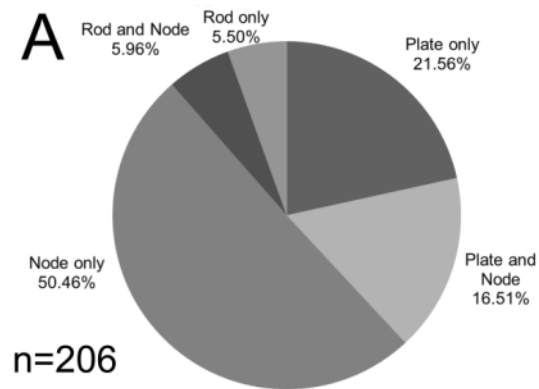


**Figure 2.7** (A) Cavities were located on nodes more often than either plate-like or rod-like trabeculae. (B) The subset of cavities that were not entirely on nodes (n=105) were located on longitudinal trabeculae more often than oblique or transverse trabeculae.

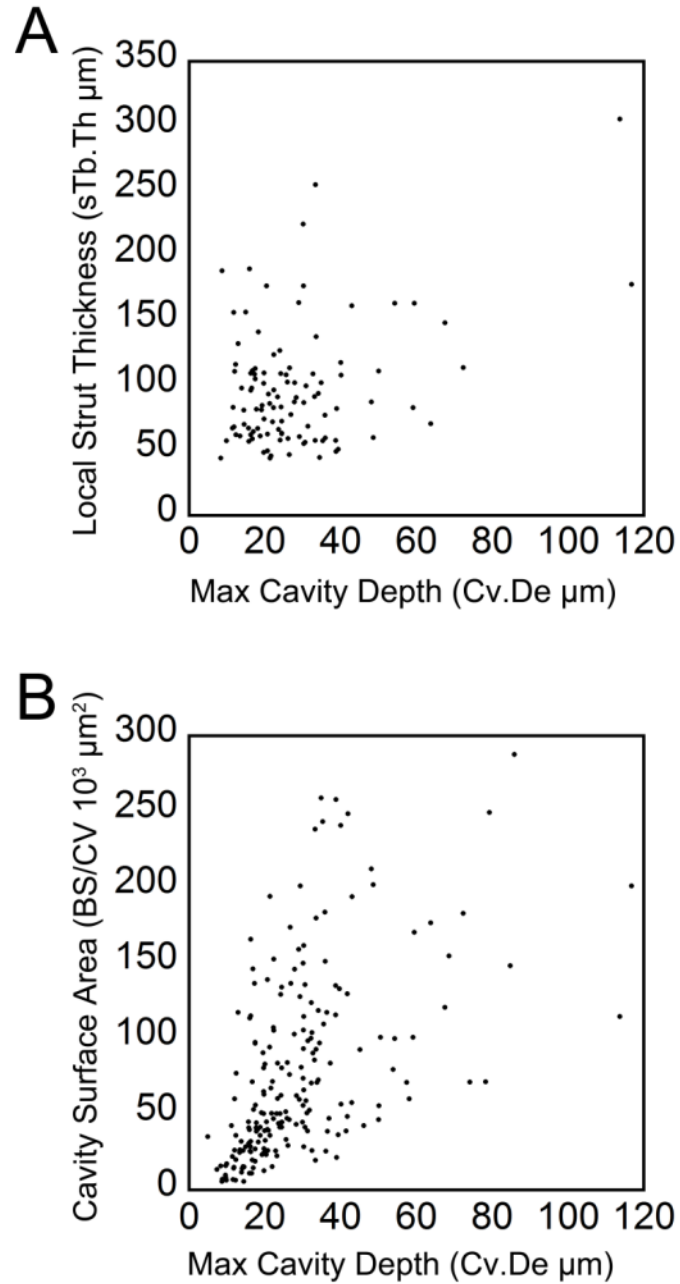


**Figure 2.8** Maximum cavity depth was correlated with both (A) local trabecular thickness ( $p < 0.05$ ,  $r^2 = 0.14$ ) and (B) cavity surface area ( $p < 0.05$ ,  $r^2 = 0.25$ ), however due to the large amount of scatter in the graphs the relationships are not predictive.

**Table 2.1** Characteristics of trabecular microarchitecture and resorption cavities in human lumbar vertebral trabecular bone are shown (n=9 specimens).

Measure	Mean $\pm$ SD
Percent Eroded Surface* (ES/BS, %)	5.10 $\pm$ 1.75
Bone Volume Fraction (BV/TV, %)	6.75 $\pm$ 2.45
Bone Surface to Bone Volume Ratio (BS/BV, mm <sup>2</sup> /mm <sup>3</sup> )	27.08 $\pm$ 4.41
Trabecular Thickness (Tb.Th, $\mu$ m)	132.58 $\pm$ 22.15
Trabecular Separation (Tb.Sp, $\mu$ m)	1,015.50 $\pm$ 216.52
Degree of Anisotropy (DA)	1.48 $\pm$ 0.12
Structure Model Index (SMI)	1.70 $\pm$ 0.60
Connectivity Density (Conn.D, mm <sup>-3</sup> )	4.84 $\pm$ 2.26
Average Maximum Cavity Depth (Cv.De, $\mu$ m)	30.10 $\pm$ 8.56
Average Surface Area per Cavity (BS/Cv, 10 <sup>3</sup> $\mu$ m <sup>2</sup> )	80.60 $\pm$ 22.23
Average Volume per Cavity (Cv.V, 10 <sup>3</sup> $\mu$ m <sup>3</sup> )	614.16 $\pm$ 311.93
Average Maximum Cavity Depth/ Average Cavity Surface Area (Cv.De / BS/Cv, 10 <sup>-5</sup> $\mu$ m <sup>-1</sup> )	55.92 $\pm$ 12.00
Median Maximum Cavity Depth (Cv.De, $\mu$ m)	26.31 $\pm$ 6.57
Median Surface Area per Cavity (BS/Cv, 10 <sup>3</sup> $\mu$ m <sup>2</sup> )	66.86 $\pm$ 25.76
Median Volume per Cavity (Cv.V, 10 <sup>3</sup> $\mu$ m <sup>3</sup> )	343.62 $\pm$ 195.73
Average Maximum Cavity Depth/ Average Local Trabecular Thickness (Cv.De/sTb.Th, %)	30.46 $\pm$ 7.04
Number of Cavities (N.Cv/BS, 1/mm <sup>2</sup> ) <sup>#</sup>	0.66 $\pm$ 0.28
Number of Cavities per Unit Tissue Volume (N.Cv/TV 1/mm <sup>3</sup> ) <sup>#</sup>	1.25 $\pm$ 0.77
Total Volume Occupied by Cavities (Tt.Cv.V/BV, %) <sup>#</sup>	1.03 $\pm$ 0.53

\* measured using a grid and line intersection counts

# derived from specimen averages

**Table 2.2** Measures of resorption cavities on rod-like trabeculae, plate-like trabeculae and nodes are shown (cavities from all specimens were pooled, median (25<sup>th</sup> percentile, 75<sup>th</sup> percentile)).

Measure	Cavities on Rod-Like Trabeculae (n=25)	Cavities on Plate-Like Trabeculae (n=82)	Cavities on Nodes (n=99)
Maximum Cavity Depth / Local Trabecular Thickness (Cv.De / sTb.Th, %)	21.72 (14.57, 30.55)	31.02 (20.50, 45.73) *	
Maximum Cavity Depth (Cv.De, $\mu\text{m}$ )	18.74 (14.67, 26.02)	25.04 (18.85, 35.42) *	25.49 (17.40, 35.50) *
Surface Area per Cavity (BS/Cv, $10^3 \mu\text{m}^2$ )	46.39 (23.56, 71.67)	71.80 (36.53, 136.45) *	53.064 (32.09, 100.26)
Volume per Cavity (Cv.V, $10^3 \mu\text{m}^3$ )	122.69 (70.86, 372.88)	297.40 (140.00, 891.64) *	248.10 (99.32, 742.18)
Maximum Cavity Depth/ Cavity Surface Area (Cv.De / BS/Cv, $10^{-3} \mu\text{m}^{-1}$ )	0.48 (0.33, 0.91)	0.45 (0.24, 0.63)	0.47 (0.31, 0.78)

\*  $p < 0.05$  as compared to cavities on rod-like trabeculae

**Table 2.3** Correlations among measures of individual cavities are shown (n=206 cavities). The upper triangle presents Spearman's rho while the lower triangle presents the 95% confidence interval in Spearman's rho (confidence intervals that do not include zero are considered significant).

	Max Cavity Depth/Local Trabecular Thickness (Cv.De / sTb.Th, %)	Cavity Surface Area (BS/Cv, $\mu\text{m}^2$ )	Cavity Volume (Cv.V, $\mu\text{m}^3$ )	Max Cavity Depth (Cv.De, $\mu\text{m}$ )	Local Trabecular Thickness (sTb.Th, $\mu\text{m}$ )
Max Cavity Depth/Local Trabecular Thickness (Cv.De / sTb.Th, %)		0.55*	0.63*	0.74*	-0.52*
Cavity Surface Area (BS/Cv, $\mu\text{m}^2$ )	(0.38,0.65)		0.86*	0.62*	0.02
Cavity Volume (Cv.V, $\mu\text{m}^3$ )	(0.33,0.62)	(0.63,0.77)		0.81*	0.01
Max Cavity Depth (Cv.De, $\mu\text{m}$ )	(0.46,0.71)	(0.42,0.62)	(0.53,0.70)		0.10
Local Trabecular Thickness (sTb.Th, $\mu\text{m}$ )	(-0.54,-0.22)	(-0.19,0.19)	(-0.16,0.23)	(0.20,0.53)	

\* p<0.05

**Table 2.4** Correlations among measures of cavities and trabecular microarchitecture are shown (n=9 specimens). The upper triangle presents Spearman's rho while the lower triangle presents the 95% confidence interval in rho.

	Bone Volume Fraction (BV/TV, %)	Bone Surface to Bone Volume Ratio (BS/BV, 1/mm)	Trabecular Thickness (Tb.Th, $\mu\text{m}$ )	Trabecular Separation (Tb.Sp, $\mu\text{m}$ )	Degree of Anisotropy (DA)	Structure Model Index (SMI)	Connectivity Density (Conn.D, $\text{mm}^{-3}$ )	Average Max Cavity Depth/Local Trabecular Thickness (Cv.De / sTb.Th, %)	Average Cavity Surface Area (BS/Cv, $\mu\text{m}^2$ )	Average Cavity Volume (Cv.V, $\mu\text{m}^3$ )	Average Max Cavity Depth (Cv.De, $\mu\text{m}$ )
Bone Volume Fraction (BV/TV, %)		-0.61	0.58	-0.58	-0.35	-0.80*	0.19	-0.79*	0.10	-0.10	-0.14
Bone Surface to Bone Volume Ratio (BS/BV, 1/mm)	(-0.91, 0.10)		-0.66	-0.17	0.42	0.34	0.32	0.70*	-0.41	-0.29	-0.19
Trabecular Thickness (Tb.Th, $\mu\text{m}$ )	(-0.14, 0.90)	(-.92, 0.01)		-0.17	0.13	-0.27	-0.13	-0.73*	0.28	-0.12	-0.10
Trabecular Separation (Tb.Sp, $\mu\text{m}$ )	(-0.90, 0.13)	(-0.75, 0.55)	(-0.75, 0.56)		0.21	0.33	-0.30	0.26	0.29	0.62	0.49
Degree of Anisotropy (DA)	(-0.82, 0.41)	(-0.34, 0.85)	(-0.58, 0.73)	(-0.53, 0.77)		-0.01	0.17	0.13	0.09	0.11	0.23
Structure Model Index (SMI)	(-0.96, -0.28)	(-0.42, 0.82)	(-0.79, 0.48)	(-0.43, 0.81)	(-0.67, 0.66)		-0.44	0.64	-0.08	-0.19	-0.12
Connectivity Density (Conn.D, $\text{mm}^{-3}$ )	(-0.54, 0.76)	(-0.44, 0.81)	(-0.73, 0.58)	(-0.80, 0.46)	(-0.56, 0.75)	(-0.86, 0.31)		0.00	-0.25	-0.14	-0.42
Average Max Cavity Depth/Local Trabecular Thickness (Cv.De / sTb.Th, %)	(-.95, -0.27)	(0.06, 0.93)	(-0.94, -0.13)	(-0.49, 0.79)	(-0.58, 0.73)	(-0.05, 0.91)	(-0.66, 0.67)		0.09	0.18	0.17
Average Cavity Surface Area (BS/Cv, $\mu\text{m}^2$ )	(-0.61, 0.71)	(-0.84, 0.35)	(-0.47, 0.80)	(-0.46, 0.80)	(-0.61, 0.71)	(-0.71, 0.62)	(-0.78, 0.50)	(-0.61, 0.71)		0.80*	0.76*
Average Cavity Volume (Cv.V, $\mu\text{m}^3$ )	(-0.72, 0.60)	(-0.80, 0.46)	(-0.73, 0.59)	(-0.07, 0.91)	(-0.60, 0.72)	(-0.76, 0.54)	(-0.74, 0.58)	(-0.55, 0.75)	(0.29, 0.96)		0.89*
Average Max Cavity Depth (Cv.De, $\mu\text{m}$ )	(-0.73, 0.58)	(-0.76, 0.54)	(-0.72, 0.61)	(-0.25, 0.87)	(-0.51, 0.78)	(-0.73, 0.59)	(-0.85, 0.34)	(-0.56, 0.75)	(0.20, 0.95)	(0.57, 0.98)	

\* p<0.05

## ***2.5 Discussion***

The current study provides the first quantitative measures of individual resorption cavities in human cancellous bone using three-dimensional imaging. The study demonstrates that maximum cavity depth, surface area and volume are related to local trabecular microarchitecture and that cavities are located primarily on nodes within the trabecular microarchitecture.

There are a number of strengths to the current study that support our conclusions. First, measures of resorption cavities were generated by identifying the scalloped or crenated surface (a classic method of identifying eroded surfaces) as well as by observing the cavity as an indentation on the bone surface in three-dimensional images. Second, the current study provides the first measures of maximum depth of each cavity using a three-dimensional approach. The three-dimensional approach can be applied to any cavity observed in the specimen (i.e. it is not limited to certain shapes, etc.). Prior work using lamellar counting was limited to only a few cavity profiles in a two-dimensional cross-section, potentially generating a sampling bias (i.e. too few cavity profiles per specimen) [232]. Additionally, the lamellar counting approach requires assumptions regarding uniform thickness of individual lamellae. Lastly, the three-dimensional approach can provide information regarding the number of cavities and the depth of each individual cavity. As it is not possible to enumerate cavities using a two-dimensional approach (Figure 2.1), two-dimensional measures of resorption cavities cannot describe the breadth or volume of resorption cavities or their location in the trabecular microarchitecture (rod-like trabeculae, plate-like trabeculae

etc.).

There are some limitations that must be considered in interpreting our results. First, the current method detects resorption cavities using eroded surfaces and does not identify the presence of osteoclasts or other cells when measuring maximum cavity depth and surface area. Hence the current approach should be interpreted as a measure of morphology and not a direct measure of bone resorption. When using two-dimensional approaches, it is necessary to identify pre-osteoblasts on an eroded surface to ensure that bone resorption is complete at the cross-section where cavity depth is measured [232]. However, the three dimensional approach examines the entire cavity not just a two-dimensional cross-section. The entire cavity consists of all of the eroded surface in a basic multicellular unit (BMU), including eroded surface with active resorption as well as eroded surface where the resorption is complete (presumably covered with pre-osteoblasts) [42]. When viewed in three-dimensions a resorption cavity will include eroded surface where resorption is complete except when a BMU is so new that it has not yet completed a single resorption cycle. Using existing histomorphometry data it is possible to estimate the proportion of BMUs that have not completed a resorption cycle: The active erosion period of a BMU in humans has been reported to be 42 days with an entire erosion period of 51 days [189]. Parfitt has estimated that a BMU progresses for 6-12 months [233] (the parameter has never been measured in human cancellous bone). Summing the erosion period and the period of BMU progression suggests that each BMU will display eroded surface for ~8 to 14 months). The active resorption period (42 days) corresponds to only 12-18% of the total time period that a BMU displays eroded surface. Hence, only 12-18% of

all resorption cavities viewed in three-dimensions will not display eroded surface with complete resorption, and it is unlikely such a small percentage would bias our findings.

Second, the raw images had anisotropic voxels (0.7 X 0.7 X 5.0  $\mu\text{m}$ ). As a result, observation of resorption cavities was limited to eroded surface profiles in transverse cross-sections (with a pixel size of 0.7 X 0.7  $\mu\text{m}$ ). Eroded surface (ES/BS) measured in transverse cross-sections slightly differs from unbiased sampling methodology for cancellous bone, which requires longitudinal sections [211, 234]. As a result, there is the possibility that our approach under-reports cavities on transverse trabeculae because transverse trabeculae are less likely to be captured in transverse cross-sections. However, existing data suggests measurement bias from specimen orientation does not greatly influence conclusions regarding the location of cavities relative to trabecular orientation. Using morphological decomposition, Liu and colleagues have determined the average thickness and volume of bone occupied by rod- and plate-like trabeculae as well as the percentage of rod- and plate-like trabeculae with transverse orientations [231]. Using the averages reported by Liu et al., we estimate that the bone surface of transverse trabeculae constitutes only 16% of the surface in vertebral cancellous bone. If cavities were distributed uniformly across trabecular bone surfaces, we would expect ~16% of resorption cavities to be located on transverse trabeculae, a value that is similar to our observation of 11% in the current study. We therefore consider any potential measurement bias to be minor (Figure 2.7B).

It is useful to compare measures of resorption cavity surface area and depth

made with the current three-dimensional approach with those achieved previously using two-dimensional approaches (Table 2.5). First, resorption cavity surface area measured in the current study (mean  $0.09 \text{ mm}^2$ ) is similar to the “typical” cavity size estimated from scanning electron microscopy ( $0.10 \text{ mm}^2$ ) [217], but much larger than that measured in two-dimensional cross-sections from the iliac crest ( $0.003\text{-}0.004 \text{ mm}^2$ ) [213, 235] (Table 2.5). We do not consider prior work estimating cavity surface area in two-dimensional sections to be comparable to the current study because the work did not use stereology methods capable of enumerating individual cavities and was likely biased (Figure 2.1) [236]. With regard to maximum cavity depth, measures of average maximum cavity depth observed in the current study are 40% smaller than the median values of erosion depth achieved using lamellar counting techniques in two-dimensional sections from the iliac crest (Table 2.5). Although it is possible that differences between bone remodeling in the iliac crest and vertebral body may contribute to the discrepancy, the mean and median values in our study are below the 10<sup>th</sup> percentile of that reported using lamellar counting, suggesting that the difference is likely due to measurement methods. Assumptions made using lamellar counting methods (uniform thickness of lamellae, orientation of lamellae relative to the bone surface) may explain why measures using the lamellar counting technique are greater than those determined here [214]. Two-dimensional techniques that do not use lamellar counting achieve similar measures of maximum cavity depth as the current study (Table 2.5) [213, 235].

**Table 2.5** Measures of resorption cavities made in the current study using three-dimensional approaches are shown along with those reported in prior studies using two-dimensional techniques.

Source	Average Cavity Surface Area (mm <sup>2</sup> )	Measurement Approach	Average Maximum Cavity Depth (µm)	Measurement Approach
Current Study	0.081 ± 0.022	Serial Milling	30.10 ± 8.56	Three-dimensional Spline Fit (mean±SD)
Mosekilde 1990 [217]	0.1 (0.001 – 1.00)	SEM (Estimated size and range)	NR	
Eriksen et al. (1990) [212]	NR		49.1 (38.3 – 61.7)	Lamellar Counting (median, 10 <sup>th</sup> and 90 <sup>th</sup> percentiles)
Garrahan et al. (1990) [213]	NR		28.9 (23.4 – 39.3)	Spline fit on two-dimensional cross-section (mean with range)
Croucher et al. (1991) [235]	Males: 0.004 (0.002 – 0.007) Females: 0.003 (0.002 – 0.006)	Geometric mean and 95% range estimated from lengths of individual profiles*	Males: 35.6 (23.2 – 54.7) Females: 33.7 (24.4 – 46.6)	Spline fit on two-dimensional cross-sections Geometric mean and 95% range estimated from lengths of individual profiles*
Cohen-Solal et al. (1991) [214]	NR		Control: 40.8 ± 2.0	Manual estimation of ‘pre-resorbed surface’
Cohen-Solal et al. (1991) [214]	NR		Osteoporosis: 41.4 ± 2.0	

NR – Not Reported

\* Estimating the object number/surface area from profiles is not a recognized stereology approach [236]

In the current study we found 50% of cavities on nodes in the trabecular microarchitecture and 79% of the remaining cavities on longitudinally oriented trabeculae, primarily plate-like trabeculae. In surveys of cancellous bone from the femoral neck, Gentsch and colleagues report a much larger percentage of cavities on rod-like trabeculae (37-38%) [237, 238]. It is unclear if the differences between our results and Gentsch and colleagues are due to differences in skeletal region, visualization method, or sampling approach (the current study uses cross-sections to detect cavities while Gentsch and colleagues use small specimens submitted to scanning electron microscopy).

The aspects of osteoclast biology that determine maximum cavity depth are currently unclear. It has been proposed that alterations in osteoclast lifespan through regulation of osteoclast apoptosis may modify the surface area and/or maximum depth of individual resorption cavities and remodeling sites [239-241], but as there have been few three-dimensional studies of resorption cavities the relationship between rates of osteoclast apoptosis and resorption cavity morphology are unclear. Recent studies suggest that anti-catabolic agents such as cathepsin K inhibitors may cause resorption cavities to be more shallow and smaller in surface area [242] and that glucocorticoid treatment may modify resorption cavity shape [243], suggesting that drug treatments and disease states can alter cavity shape as well as number, potentially influencing cancellous bone biomechanics and rates of bone loss. Our laboratory recently found that established estrogen depletion in rats was not associated with changes in resorption cavity surface area or maximum cavity depth [229].

Although the current study did not examine biomechanical properties, it is

useful to consider the potential biomechanical implications of our observations. A simple mechanical analysis suggests that the depth and surface area of resorption cavities influence stress concentration factors and potentially cancellous bone biomechanics [223] (Figure 2.9). The current study found that typically maximum cavity depth is, on average, 30% of local trabecular thickness, suggesting that a typical resorption cavity may increase local tissue stresses by 2-3 times (Figure 2.9). However, cavities that were 40-50% of the local trabecular thickness were not unusual. Prior work using high-resolution finite element models suggests that tissue yielding occurs preferentially in longitudinally oriented plate-like trabeculae, where we observed cavities to be more common (Figure 2.7B) [110, 222]. A more thorough finite element analysis would be required to determine if cavity location is related to habitual stresses in cancellous bone specimens. In conclusion, we have demonstrated a method of visualizing individual resorption cavities that provides the first, three-dimensional measures of resorption cavity location, maximum depth and volume in human vertebral cancellous bone. The technique may be applied to any resorption cavity displaying an eroded surface profile in cancellous bone and can also be combined with other techniques to assess local trabecular thickness.

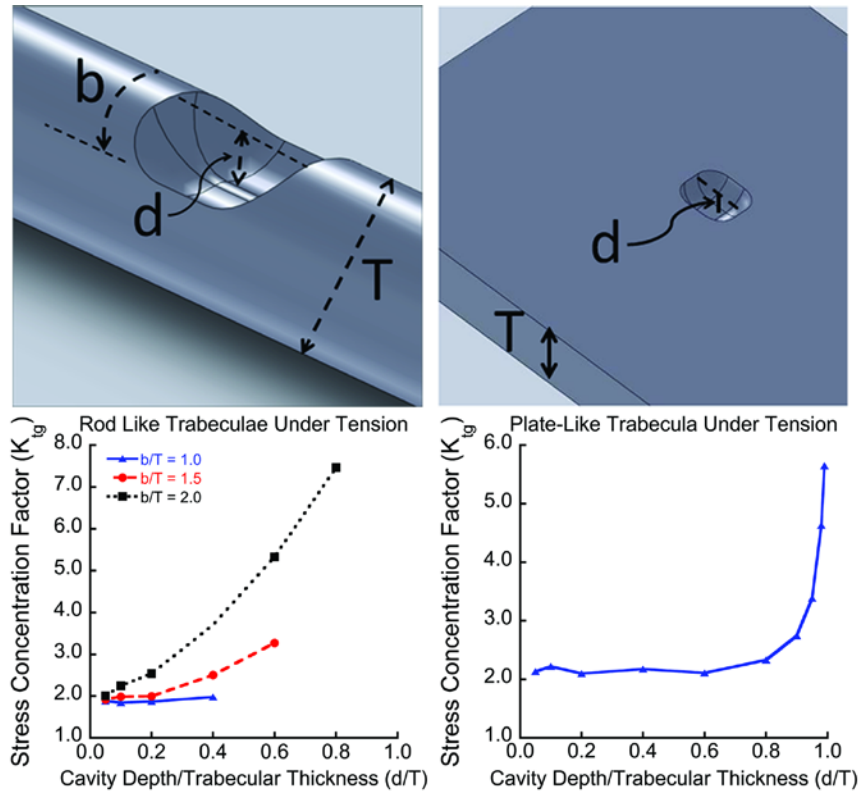


**Figure 2.9** Simple linear elastic finite element models generated with idealized cavities on (left) rod-like trabeculae and (right) plate-like trabeculae are shown [223]. The gross stress concentration factor ( $K_{tg}$ , maximum stress with the cavity/maximum stress without the cavity) is shown to increase as the ratio of maximum cavity depth to local trabecular thickness (referred to as  $d/T$ ) increases. In rod-like trabeculae the ratio of cavity breadth to local trabecular thickness (referred to as  $b/T$ ) is also shown to influence the gross stress concentration factor.

## 2.6 Acknowledgements

Supported by NIH/NIAMS R01 AR057362 (PI Hernandez).

Authors' roles: Study design: MGG, CRS, SRK, and CJH. Specimen Acquisition:

IHY, MGJ, and TMK. Image collection and analysis: CRS, EVT, SEF and CJH

Statistical Analysis: MGG and CJH. Drafting manuscript: MGG, CRS and CJH.

Revising manuscript content: MGG, CRS and CJH. Approving final version of

manuscript: CRS, EVT, SEF, IHY, MGJ, TMK, and CJH. MGG and CJH take responsibility for the integrity of the data analysis.

## ***2.7 Supplementary Material***

Cavity depth is determined by estimating the pre-resorbed surface using a thin plate smoothing spline [229]. A curve fit using a thin plate smoothing spline provides a smooth, continuous curve spanning a void on a three-dimensional surface. The technique is commonly used in image processing [227, 228]. In the current study, the thin plate smoothing spline curve fit is created through interpolation from the bone surface surrounding the cavity. In our implementation, we use the Lagrangian boundary conditions, which constrain the position and angle of the thin plate smoothing spline fit to match the bone surface surrounding the cavity.

To test the accuracy of the approach we devised test shapes of controlled geometry spanning a range of surface curvatures. The three test shapes were a hyperboloid, a cylinder and a hemispherical cap (Figure 2.10). These three test shapes represent a range of Gaussian curvature: the hyperboloid has a negative Gaussian curvature, the cylinder has a zero Gaussian curvature and the spherical cap has a positive Gaussian curvature [244]. Spherical cavities were added digitally to each test shape (Figure 2.10). Three different cavity sizes were examined, ranging in size from 25% to 75% of the convex radius of the original shape. The depth of the cavity was then determined using the thin plate smoothing spline technique (Figure 2.10). The measurement error was calculated using the following equation:

Measurement Error = (Measured Depth-Actual Depth)/Actual Depth x 100%,  
where Measured Depth is the distance measured using the automated cavity depth program and Actual Depth is the actual depth of the cavity generated on the test image. We observed a measurement error of less than 12% (Figure 2.11). For cavities on cylindrical and spherical cap surfaces, the measurement error was an overestimation except for the 75% cavity size case. For cavities on the hyperboloid, the measurement error was an underestimation.

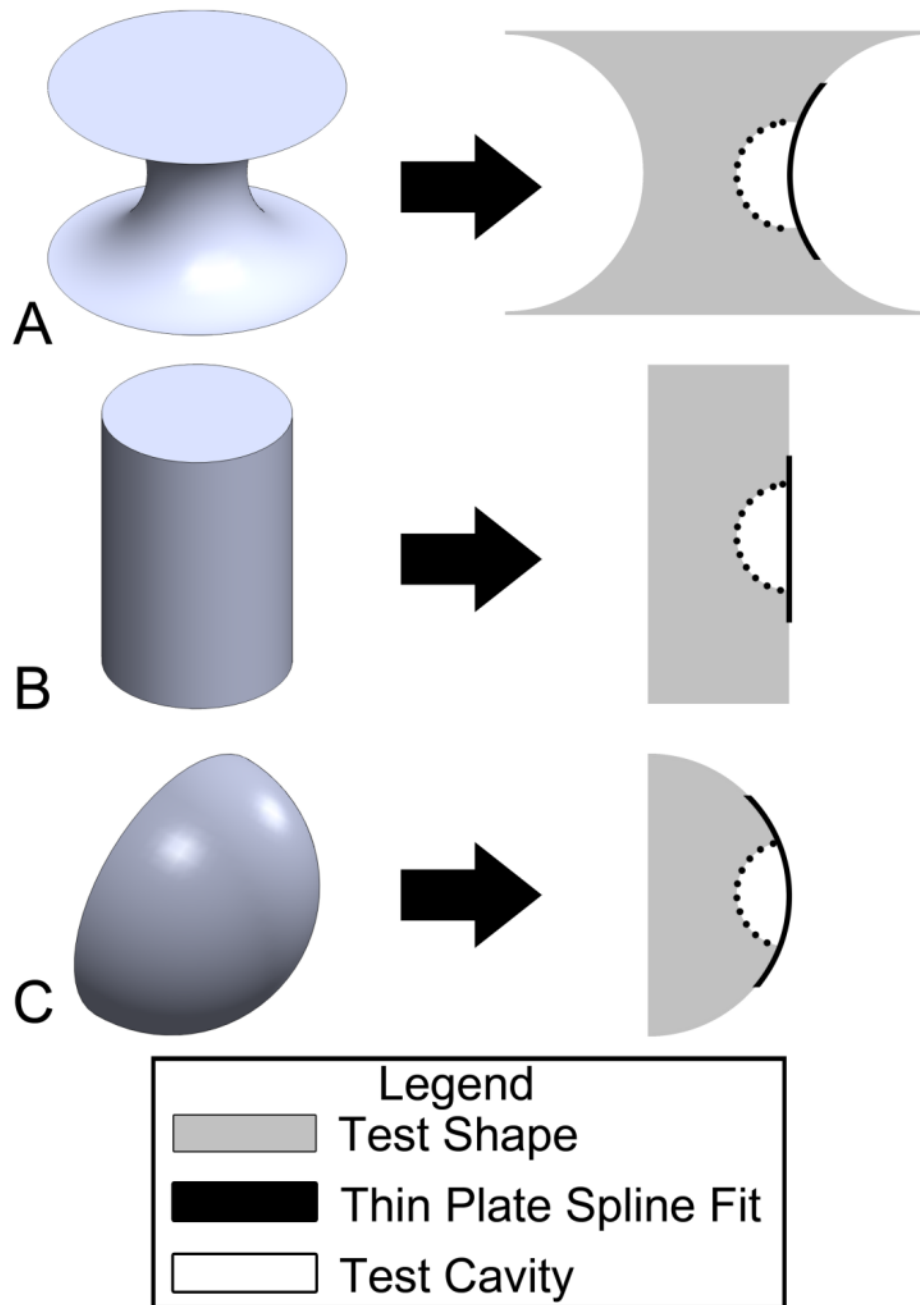


**Figure 2.10** Three dimensional test shapes used to benchmark cavity depth measurements included (A) a hyperboloid, (B) a cylinder, and (C) a spherical cap. Spherical cavities were added to the shape (right). The thin plate smoothing spline fit over the cavity estimated the surface of the test shape that was removed by the cavity.

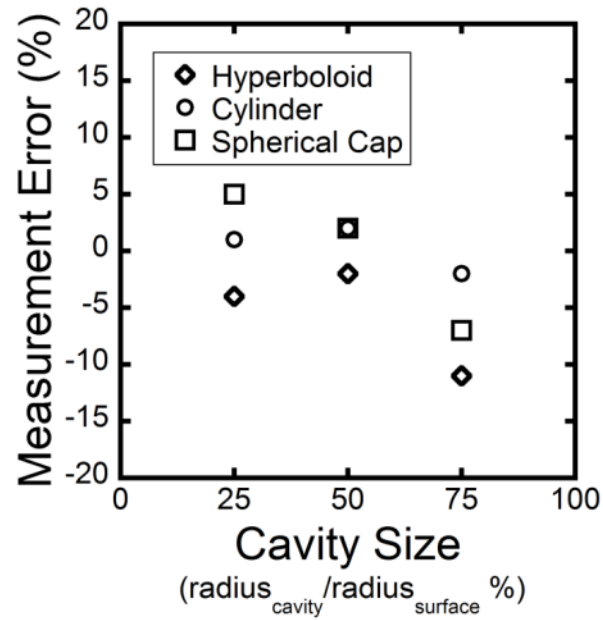


**Figure 2.11** The measurement error for cavities added to the test shapes is shown. Three different cavity sizes were simulated, ranging in size from 25% to 75% of the convex radius of each test shape.

## CHAPTER 3

### **Techniques to Detect the Proximity of Objects in Three-Dimensional Models**

This chapter was published in the Journal of Biomechanics in 2014 in Volume 47 (pgs. 3156-3161). The article is titled “The Effects of Misalignment During In vivo Loading of Bone: Techniques to Detect the Proximity of Objects in Three-Dimensional Models” by Goff MG, Chang KL, Litts EN, and Hernandez CJ and is reprinted here with permission of Elsevier.

#### **3.1 Abstract**

Theories of mechanical adaptation of bone suggest that mechanical loading causes bone formation at discrete locations within bone microstructure experiencing the greatest mechanical stress/strain. Experimental testing of such theories requires in vivo loading experiments and high-resolution finite element models to determine the distribution of mechanical stresses. Finite element models of in vivo loading experiments typically assume idealized boundary conditions with applied load perfectly oriented on the bone, however small misalignments in load orientation during an in vivo experiment are unavoidable, and potentially confound the ability of finite element models to predict locations of bone formation at the scale of micrometers. Here we demonstrate two different three-dimensional spatial correlation methods to determine the effects of misalignment in load orientation on the

locations of high mechanical stress/strain in the rodent tail loading model. We find that, in cancellous bone, the locations of tissue with high stress are maintained under reasonable misalignments in load orientation ( $p < 0.01$ ). In cortical bone, however, angular misalignments in the dorsal direction can alter the locations of high mechanical stress, but the locations of tissue with high stress are maintained under other misalignments ( $p < 0.01$ ). We conclude that, when using finite element models of the rodent tail loading model, small misalignments in loading orientation do not affect the predicted locations of high mechanical stress within cancellous bone.

### ***3.2 Introduction***

Theories of bone functional adaptation suggest that bone formation occurs specifically at locations within bone microstructure where mechanical stress and strain are greatest [245, 246]. While experimental studies have shown that mechanical stimulus causes net increases in bone formation within a whole bone (see [247] for a recent review), less is known about how well discrete locations of bone formation (at the scale of tens of micrometers) correspond to regions of high mechanical stress/strain. A series of recent studies using serial micro-computed tomography have shown that locations of new bone formation stimulated by loading tend to be surrounded by greater mechanical strains than locations of quiescent bone [248-251]. However, less is known about the converse question: how well do regions of high mechanical stress/strain predict the locations of new bone formation? A major challenge in testing the idea that mechanical stress/strain during loading can predict

discrete locations of bone formation is that the stress/strain distribution in a bone loaded in vivo cannot be measured directly and must be examined using finite element modeling.

Finite element models are the primary tool used to estimate the stress/strain magnitudes for both in vivo and ex vivo loading experiments [206, 252-254]. Finite element models of in vivo loading assume idealized boundary conditions, such as pure axial loading. However, small misalignments in loading orientation are unavoidable between loading sessions when applying mechanical loads to live animals. Small misalignments in the orientation of loading may alter the distribution of mechanical stress/strain. If the distribution of mechanical stress/strain predicted by the finite element model is greatly altered, locations of bone formation predicted by finite element models are unlikely to be correct, which would confound any tests of bone adaptation theories.

The long-term goal of the current work is to understand how bone adapts to the mechanical microenvironment. In this study, we evaluate the effects of misalignment in load orientation on the locations of greatest mechanical stress/strain (where bone formation is expected). Two, three-dimensional spatial correlation techniques are presented to evaluate the effects of misalignment in load orientation.

### ***3.3 Materials and Methods***

#### ***3.3.1 Study Design***

We use the rodent tail loading model to evaluate the effects of misalignment in load orientation on the locations of high mechanical stress/strain. In the rodent tail loading model, a controlled compressive load is applied to a caudal (tail) vertebra [252, 254, 255]. Five, three-month old female Sprague Dawley rats were used for this study. Animal use was approved by Cornell University's Institutional Animal Care and Use Committee. The animals were euthanized and three-dimensional images of the eighth caudal vertebrae were collected using micro-computed tomography (CT-120, GE Healthcare, Little Chalfont, Buckinghamshire, United Kingdom) at an energy of 80 kVp, a current of 7  $\mu$ A, an integration time of 1000 ms and an isotropic voxel size of 25  $\mu$ m voxels. A global threshold for bone was determined using the Otsu method [256].

#### ***3.3.2 Finite Element Modeling***

Micro-computed tomography images were converted into finite element models with linear elastic 8 node brick elements, isotropic 25  $\mu$ m cubes, using custom software for use with Matlab (2011a, Mathworks, Natick, MA, USA) [257]. Material representing intervertebral discs was added to the caudal and cranial ends of the

vertebrae in the finite element models (diameter of 3 mm, height of 0.5 mm) [250, 254, 258, 259]. The Young's modulus of the bone was set at 9.4 GPa based on a preliminary experiment (n=5 rats) in which finite element models were matched to surface strains measured using two strain gauges attached to the outer cortex. A Poisson's ratio of 0.3 was used. The intervertebral disc tissue was assigned an elastic modulus of 4 MPa and a Poisson's ratio of 0.3 [258]. A rolling boundary condition was applied across the bottom of the caudal disc with two nodes held fixed to prevent translation. Finite element models consisted of  $4.62 \pm 0.40$  million elements (Mean  $\pm$  SD).

A parametric analysis was performed to examine the effects of misalignment in load orientation. For each vertebra, a model using idealized boundary conditions was created in which a pure axial load of 100 N (a load magnitude known to cause increases in bone formation [253]) was uniformly distributed across the cranial disc. In preliminary experiments using strain gauges, we found 100 N to cause dorsal surface strains of  $2141 \mu\epsilon \pm 644 \mu\epsilon$  and ventral surface strains of  $771 \mu\epsilon \pm 534 \mu\epsilon$  (Mean  $\pm$  SD). The strains that we measured were higher than cage activity [260] and in our preliminary work have been used to generate increased bone formation (data not shown).

Additionally, non-idealized models were created simulating misalignments in load orientation that could occur during a bout of in vivo loading. Non-idealized models contained an angular offset, a translational offset or both. Angular offsets of  $2.5^\circ$  or  $5^\circ$  were simulated in either the dorsal or ventral directions (4 simulations/bone). Translational offsets of 0.25 mm or 0.5 mm were simulated in

either the dorsal or ventral directions (4 simulations/bone). The largest misalignments ( $5^\circ$  and 0.5 mm) would be visually obvious or exceed the tolerance of fixtures used during an in vivo loading experiment and therefore represent the maximum range of off-axis loading that could be expected (Figure 3.1). For one vertebra, the combination of the maximum angular offset ( $5^\circ$  in the dorsal or ventral direction) and maximum translational offset (0.5 mm in the dorsal or ventral direction) was simulated (4 simulations). A total of 49 finite element models (5 animals X 9 simulations + 1 animal X 4 simulations of combined misalignments) were implemented on a vSMP node of the Gordon super computing system using two 8-core 2.6 GHz Intel EM64T Xeon E5 (Sandy Bridge) processors and ~1 TB of DDR3-1333 ram (SDSC) (total computer time ~400 hours).

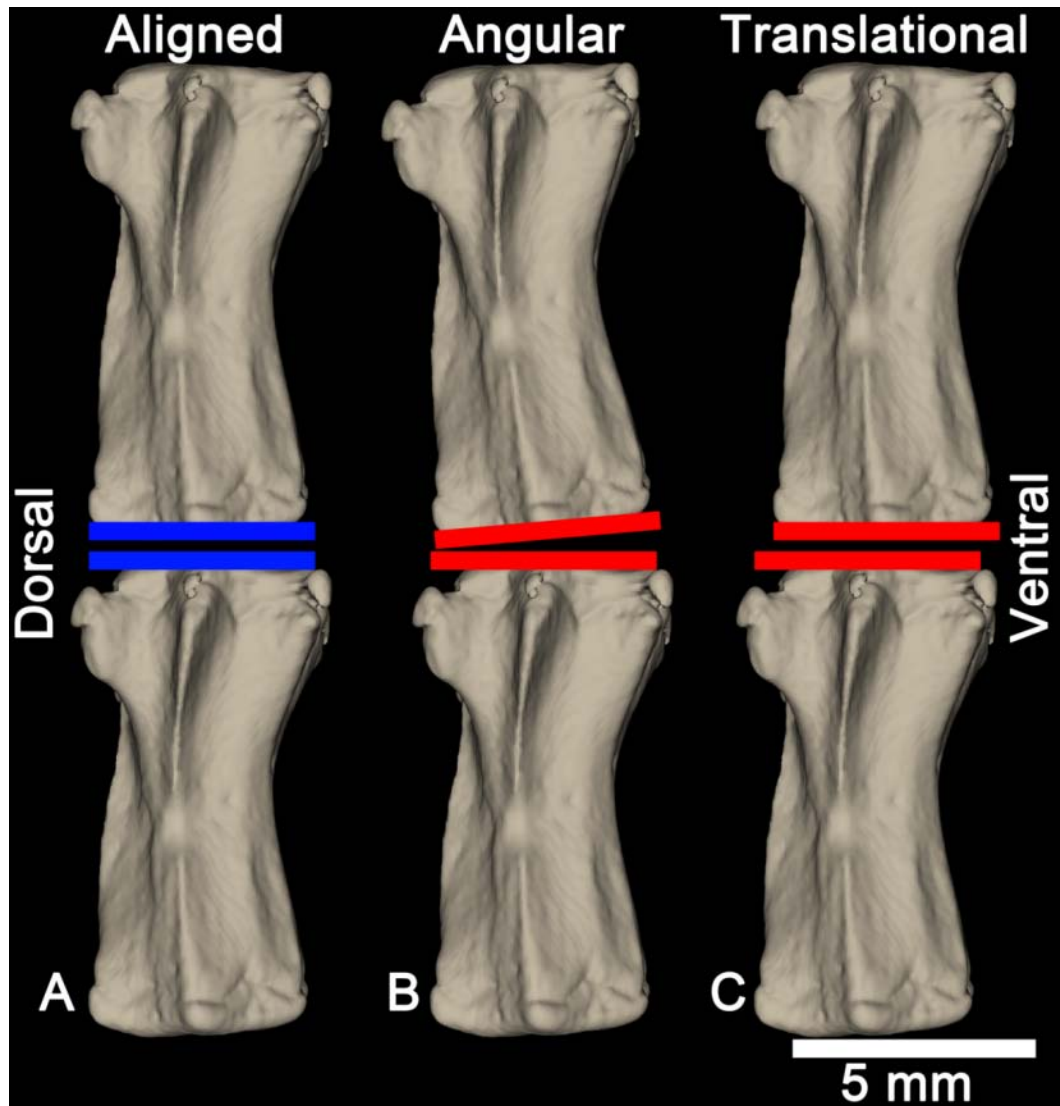


**Figure 3.1** Finite element models assume (A) perfect axial alignment of vertebra during in vivo loading, however during experimentation small angular misalignments (B) or translational misalignments (C) are unavoidable.

Most bone adaptation theories suggest that bone formation will occur at regions of the bone where tissue mechanical stress is greatest. Cancellous and cortical bone stress measurements were manually segmented by a trained observer [177]. High mechanical stress was defined as tissue with von Mises stress exceeding the 90<sup>th</sup> percentile (determined separately in cancellous and cortical bone), which we consider

a conservative estimate of tissue stress/strain that would stimulate bone formation [200, 201].

### **3.3.3 *Three-dimensional Spatial Correlation***

We tested the spatial correlation between regions of high stress in the idealized models and regions of high stress in the non-idealized models. Testing the spatial correlation of two different types of objects of arbitrary size and shape within a three-dimensional image is challenging and can be sensitive to the testing methodology. Here we used two methods to determine the spatial correlation between locations of high mechanical stress in idealized models (pure axial loading) and non-idealized models (with misalignments in loading orientation). Both methods evaluate the spatial correlation as a function of a distance,  $r$ . The first method is a three-dimensional version of a spatial correlation technique called the “inflate algorithm” [261]. The approach is summarized as follows: Consider a three-dimensional image with two types of objects of arbitrary size and shape (type A and type B) (Figure 3.2A). The percentage of type B material within a radius  $r$  of type A objects is determined (Figure 3.2B). To determine if the spatial correlation between type A and type B objects is greater than would be expected from random placement, a second image with the same volume of type B objects distributed at random within the bone volume is created and the percentage of material within the radius  $r$  of type A objects in the second image was determined (Figure 3.2C). If there is more type B material near type A objects than randomly selected material near type A objects, then the type A and

type B objects are spatially correlated.

The second spatial correlation method used is a three-dimensional adaption of the “linear dipole algorithm” described by Reed et al. [262, 263]. The approach is summarized as follows: Consider a three-dimensional image with two types of objects of arbitrary size and shape, type A and type B (Figure 3.2A). If the two types of objects are spatially correlated with one another, the expected volume of type B material at a distance  $r$  from type A material would be larger than the expected volume of type B material at a distance  $r$  from an arbitrary location in the image. In implementation, a number of randomly selected points are chosen from within type A objects and from the entire structure (Figure 3.2D,E). The amount of type B material within a shell of an inner radius of  $r$  and a thickness of one voxel is measured. While one could measure every voxel in the three-dimensional image, such an implementation is computationally expensive and a similar result can be obtained by randomly sampling a sufficient number of points. In our implementation, we sample 10,000 points from type A objects and 10,000 arbitrary points. The parameter  $g(r)$  is used to characterize the spatial correlation of type B objects to type A objects in each image:

$$g(r) = \frac{\text{Mean}(\textit{Type B object volume in a spherical shell centered around points in Type A objects})}{\text{Mean}(\textit{Type B object volume in a spherical shell around arbitrary points})},$$

where  $r$  is the radius around each point. A value of  $g(r)=1$  implies no spatial correlation (just as much type B material near a type A object as elsewhere in the image), a value of  $g(r)$  greater than one implies a positive spatial correlation (there is

more of type B material near a type A object than elsewhere in the image) and a value of  $g(r) < 1$  implies a negative spatial correlation (type B and type A objects are distant from one another).

In the current study, type A objects were tissue with high mechanical stress in the idealized model, type B objects were tissue with high mechanical stress in non-idealized model. The radius,  $r$ , examined for spatial correlation ranged from  $0 \mu\text{m}$  (0 voxels, a direct overlap of the two objects) to  $125 \mu\text{m}$  (5 voxels, ~the trabecular thickness).

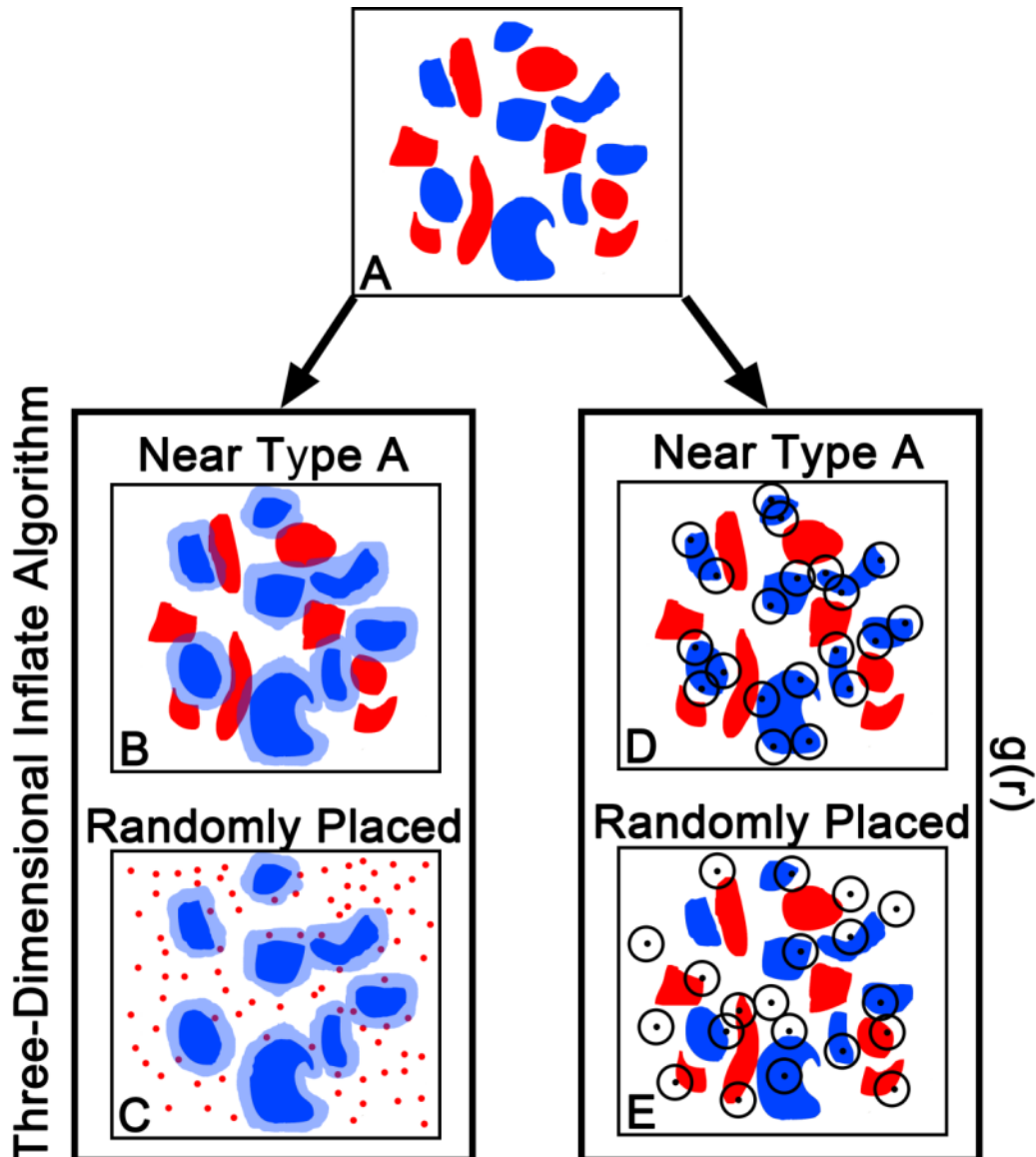


**Figure 3.2** A two-dimensional cartoon illustrating the steps involved in performing the three-dimensional spatial correlation techniques. (A) An image contains two types of objects, type A (blue) and type B (red). (B) The three-dimensional “inflate algorithm” involves dilating the type A objects by a radius,  $r$ , (shaded blue) and measuring the amount of type B material within the dilated region. (C) As a control, a volume of material equal to that of all type B objects is selected at random (red dots) and the percentage of material within a radius,  $r$ , of type A objects is measured. To calculate the  $g(r)$  spatial correlation method, a number of points are randomly chosen within type A objects (D) and randomly throughout the structure (E). A shell around each point is created with a radius  $r$  and a thickness of one voxel. The amount of type B material within the shells is measured (illustrated as circles).

### **3.3.4 *Statistical Analysis***

For the inflate algorithm, two-tailed paired t-tests were used to compare the regions of high mechanical stress between the non-idealized and idealized models. For the  $g(r)$  assay, two-tailed paired t-tests were used to compare the  $g(r)$  value for each simulation to one. A  $g(r)$  value greater than one indicated a positive spatial correlation.

## **3.4 *Results***

### **3.4.1 *Tissue Stress Magnitudes***

In cancellous bone, the 90<sup>th</sup> percentile von Mises stress ranged from 22.40 MPa to 35.76 MPa ( $27.93 \pm 3.65$  MPa, mean  $\pm$  SD) while in cortical bone, the 90<sup>th</sup> percentile ranged from 21.54 MPa to 40.88 MPa ( $28.92 \pm 4.69$  MPa) (Figure 3.3).

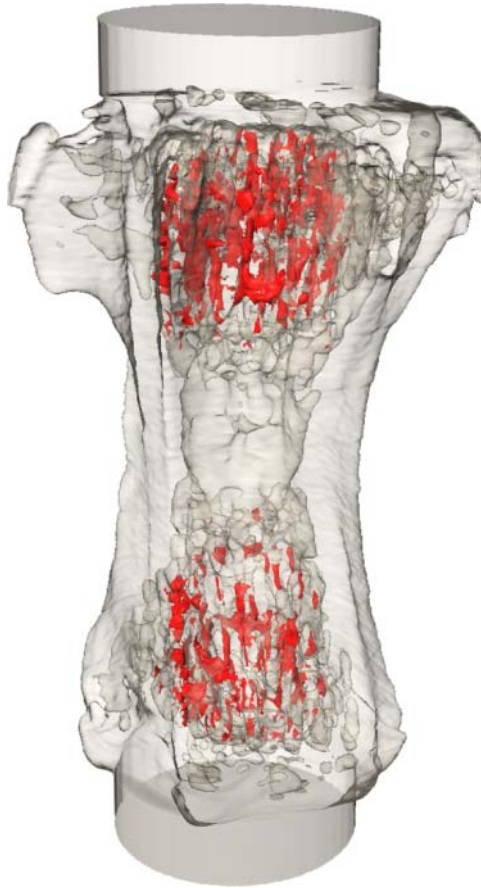


**Figure 3.3** A three-dimensional image illustrating the location of high mechanical stress (red) in cancellous bone.

### 3.4.2 *Spatial Correlations*

In cancellous bone, small misalignments in the orientation of loading did not alter the location of tissue with high mechanical stress. When using the inflate algorithm, the locations of tissue with high mechanical stress were not altered by load misalignment ( $p < 0.05$ , Figure 3.4A,C). The  $g(r)$  value (1.42 – 10.07) was larger than one indicating spatial correlation at all distances ( $p < 0.05$ , Figure 3.5A,C).

In cortical bone, dorsal angular misalignments altered the location of tissue with high mechanical stress. Models with dorsal angular misalignments showed poor spatial correlations using the inflate algorithm ( $p = 0.06 - 0.49$ , Figure 3.4D) and the  $g(r)$  value ( $p = 0.07 - 0.66$ , Figure 3.5D). However, in models containing either ventral misalignments or dorsal translational misalignments, the locations of tissue with high mechanical stress were not altered according to the inflate algorithm ( $p < 0.05$ , Figure 3.4B,D) and the  $g(r)$  method ( $g(r) = 1.15 - 9.44$ ,  $p < 0.05$ , Figure 3.5B,D).

In models with a combination of angular and translational misalignments, the spatial correlation was dominated by the angular misalignment (Figure 3.4E,F, Figure 3.5E,F).

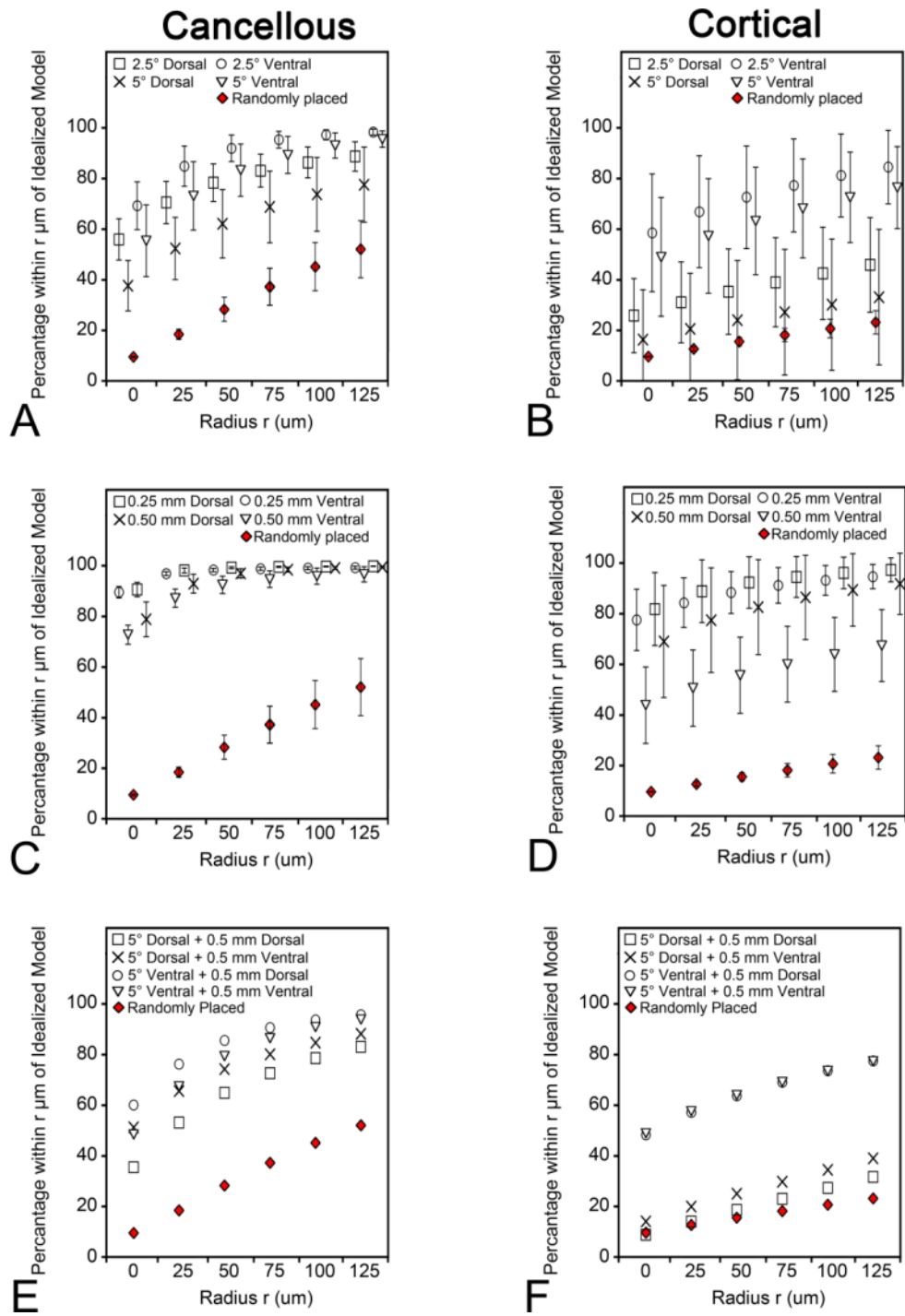


**Figure 3.4** Spatial correlations between idealized and non-idealized finite element analyses using the inflate algorithm are shown. In cancellous bone, tissue with high mechanical stress in idealized models was more likely to be near tissue with high mechanical stress in models with angular (A), translational (C) or combined (E)

misalignments than to regions selected at random. In cortical bone, tissue with high mechanical stress in idealized models was more likely to be near tissue with high mechanical stress in models with ventral angular (B) or translational (D) misalignments than regions selected at random. No spatial correlations were observed in cortical bone when dorsal angular misalignment was applied (B, F). When angular and translational misalignments were combined (E,F), the spatial correlation was dominated by the angular misalignment.

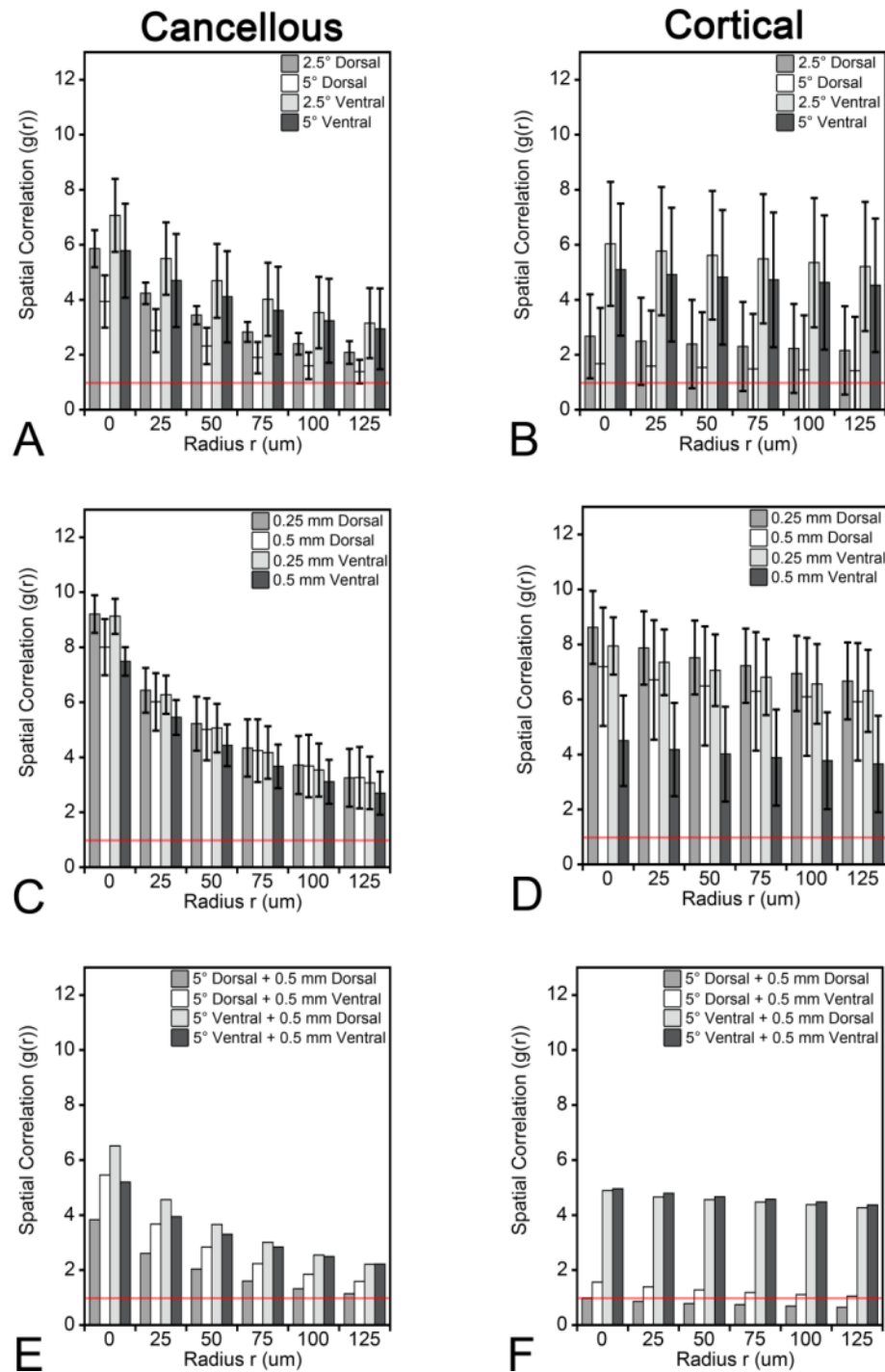


**Figure 3.5** Spatial correlations as determined using the  $g(r)$  parameter are shown (mean  $\pm$  SD) where spatial correlation is defined as  $g(r)$  is greater than one (red line). In cancellous bone, tissue with high mechanical stress in models with either angular (A) or translational (C) misalignments was spatially correlated with tissue with high

mechanical stress in the idealized model ( $g(r) > 1$ ,  $p < 0.01$ ). In cortical bone, tissue with high mechanical stress in models with both ventral angular (B) and translational (D) misalignments was spatially correlated with tissue with high mechanical stress in the idealized model ( $g(r) > 1$ ,  $p < 0.01$ ). No spatial correlations were observed in cortical bone when dorsal angular misalignment was applied (B, F). When angular and translational misalignments were combined (E, F), the spatial correlation was dominated by the angular misalignment.

### **3.5 Discussion**

Here we determined how small errors in load orientation during in vivo loading influence the locations of tissue with high mechanical stress at the scale of micrometers. When using the rodent tail loading model, small misalignments in the orientation of loading have a negligible effect on the location of cancellous bone tissue experiencing high mechanical stress. In cortical bone, dorsal angular misalignments in the orientation of loading may have an effect on the location of tissue with high mechanical stress, possibly due to bending moments caused by the bone's shape (Figure 3.1).

There are a number of strengths to the current study that support our conclusions. First, two methods were used to determine the spatial correlation between tissue with high mechanical stress in idealized and non-idealized models. Second, models with misalignment in loading orientation were compared directly to idealized models of the same bone. It has been shown that prediction of mechanical stress/bone formation in cancellous bone requires one to create a finite element model for each individual bone (rather than extrapolate cancellous bone tissue stresses using a "representative" bone) [259].

There are some limitations that must be considered in interpreting our results. First, the finite element model that we used was linear elastic. However, the maximum stress in all of the simulations (40.88 MPa) was much smaller than the compressive yield stress of human bone (134 MPa) [99], so it is unlikely that tissue non-linearity influenced our conclusions. Second, the current study, like most high resolution finite element models of bone adaptation, does not include smaller scale characteristics of bone tissue ultrastructure (resorption cavities, cement lines, tissue inhomogeneity) and therefore cannot address stress concentrations caused by ultrastructure. Third, the effects of small misalignments in the rodent tail loading model may be much less than those in other in vivo loading models (tibial loading for example) because loading of the caudal vertebra imposes relatively little bending. Fourth, the finite element models of bone use homogenous material properties and don't take into consideration the effects of variations in tissue mechanical properties such as the growth plates. However, previous studies using the rodent tail loading model have characterized bone mechanobiology with the use of homogenous tissue material properties [248, 251, 259] and the effect of growth plates would be similar within each of the paired comparisons.

Our findings suggest that when using the rodent tail loading model, the predicted location of tissue with high mechanical stress in cancellous bone is robust under reasonable misalignments in load orientation. Since regions of high mechanical stress are also regions where bone formation is expected, unavoidable errors in load alignment during in vivo loading are unlikely to alter the locations of bone formation stimulated by high mechanical stress. Therefore, we conclude the rodent tail loading

model is appropriate to test the function of theoretical models of bone adaptation at the scale of individual trabeculae.

### ***3.6 Acknowledgements***

Supported by National Science Foundation grant number 1068260 (PI Hernandez).

This work used the Extreme Science and Engineering Discovery Environment (XSEDE), which is supported by National Science Foundation grant number OCI-1053575.

Author's roles: Study design: MGG and CJH. Finite Element Analysis: KLC, MGG.

Statistical Analysis: MGG and CJH. Drafting Manuscript: MGG and CJH. Approval

final version of manuscript: MGG, KLC, ENL and CJH. MGG and CJH take responsibility for the integrity of the data analysis.

## CHAPTER 4

### **Spatial Relationship Between Microdamage, Resorption Cavities and Trabecular Surfaces**

This chapter was published in the Bone in 2015 in Volume 79 (pgs. 8-14). The article is titled “Fatigue-Induced Microdamage in Cancellous Bone Occurs Distant from Resorption Cavities and Trabecular Surfaces” by Goff MG, Lambers FM, Nguyen TM, Sung J, Rinnac CM and Hernandez CJ and is reprinted here with permission of Elsevier.

#### **4.1 Abstract**

Impaired bone toughness is increasingly recognized as a contributor to fragility fractures. At the tissue level, toughness is related to the ability of bone tissue to resist the development of microscopic cracks or other tissue damage. While most of our understanding of microdamage is derived from studies of cortical bone, the majority of fragility fractures occur in regions of the skeleton dominated by cancellous bone. The development of tissue microdamage in cancellous bone may differ from that in cortical bone due to differences in microstructure and tissue ultrastructure. To gain insight into how microdamage accumulates in cancellous bone we determined the changes in number, size and location of microdamage sites following different amounts of cyclic compressive loading. Human vertebral cancellous bone specimens

(n=32, 10 male donors, 6 female donors, age  $76 \pm 8.8$ , mean  $\pm$  SD) were subjected to sub-failure cyclic compressive loading and microdamage was evaluated in three-dimensions. Only a few large microdamage sites (the largest 10%) accounted for 70% of all microdamage caused by cyclic loading. The number of large microdamage sites was a better predictor of reductions in Young's modulus caused by cyclic loading than overall damage volume fraction (DV/BV). The majority of microdamage volume ( $69.12 \pm 7.04\%$ ) was located more than  $30 \mu\text{m}$  (the average erosion depth) from trabecular surfaces, suggesting that microdamage occurs primarily within interstitial regions of cancellous bone. Additionally, microdamage was less likely to be near resorption cavities than other bone surfaces ( $p < 0.05$ ), challenging the idea that stress risers caused by resorption cavities influence fatigue failure of cancellous bone. Together, these findings suggest that reductions in apparent level mechanical performance during fatigue loading are the result of only a few large microdamage sites and that microdamage accumulation in fatigue is likely dominated by heterogeneity in tissue material properties rather than stress concentrations caused by micro-scale geometry.

#### ***4.2 Introduction***

Impaired material toughness and resistance to crack growth in bone has been implicated as a cause of fragility fractures in patients with diabetes and patients submitted to long-term bisphosphonate treatment [264, 265]. Examination of microdamage is the primary means of assessing tissue material toughness and

resistance to crack growth [135, 137, 144]. Most of our understanding of microdamage is derived from studies of cortical bone. However, fragility fractures typically occur in regions of the skeleton dominated by cancellous bone [190, 191].

Cancellous bone microarchitecture and ultrastructure differs from that in cortical bone in ways that may influence the development of microdamage. In cortical bone, microdamage forms primarily in interstitial tissue and microdamage morphology may be influenced by structures such as the cement lines that surround osteons [135-137]. In cancellous bone, interstitial tissue is present in the central regions of trabeculae, distant from the trabecular surfaces [266], yet trabecular surfaces are expected to show the greatest tissue stresses due to bending and torsion of individual trabeculae during loading. Additionally, the orientation of cement lines in cancellous bone differs from that in cortical bone since cancellous bone does not have osteons per se (instead it has “hemi-osteons”) [188]. Furthermore, remodeling in cancellous bone causes the generation of resorption cavities, which are believed to act as stress risers and encourage the initiation and propagation of microdamage [162, 164].

Characterization of the development of microdamage in cancellous bone requires measurement of the number and size of individual microdamage sites. While there have been many studies of microdamage in cancellous bone [186, 267-271] most studies have evaluated microdamage using two dimensional methods that cannot accurately measure the number or size of microdamage sites or provide information about the location of microdamage sites relative to the rest of the trabecular microstructure due to the lack of out-of-plane information [272]. We and others have

used three-dimensional imaging methods to examine the overall amounts of microdamage generated in cancellous bone following loading [78, 273, 274], but the number, size and location of microdamage sites relative to the bone surface or resorption cavities has not been reported. Hence, it is unclear how the number and size of microdamage sites is related to the amount of applied loading.

The long-term goal of the current work is to understand how microdamage in cancellous bone contributes to cancellous bone failure and clinical fracture. Specifically, in the current study we determine: 1) the relationship between the number and size of microdamage sites, and reductions in biomechanical performance (Young's modulus) following different amounts of fatigue loading; and 2) the location of microdamage relative to bone surfaces and resorption cavities.

### **4.3 Methods**

We performed an extended analysis of specimens described in a previous study [78]. In section 2.1 we briefly review the experimental methods of the prior study and in sections 2.2-2.5 we describe the methods novel to the current study.

#### **4.3.1 Study design**

Specimens were collected from the L3 vertebral bodies of 16 donors (10 male, 6 female, 62-92 years of age, tissue from NDRI, Philadelphia, PA). The donors had no history of metabolic bone disease and displayed no obvious vertebral deformities.

Cylinders of cancellous bone, 8 mm in diameter and nominally 25-30 mm height oriented in the cranial-caudal direction, were collected (2 specimens per donor, n=32 specimens total). Specimens were stored at -20 °C and hydration was maintained throughout the experiments. Specimens were press fit into brass endcaps with cyanoacrylate glue (as previously described [275]) and submitted to cyclic loading at 4 Hz between 0N and a normalized stress value ( $\sigma/E_0$ ) of 0.0035 (where  $E_0$  is the initial apparent Young's modulus and  $\sigma$  is the load divided by the cross sectional area in load control). Cyclic loading was stopped at a predetermined reduction in the apparent Young's modulus (Figure 4.1). The reductions in apparent Young's modulus were selected to observe microdamage in the secondary and tertiary phases of the fatigue life [78]. One group of specimens (n=5) was placed in the loading fixture but no load was applied. Following loading, the specimens were stained with lead uranyl acetate to identify microdamage [273]. Three-dimensional images of each cylinder of cancellous bone were acquired through micro-computed tomography to characterize trabecular microarchitecture and stained microdamage. A region of interest (the central 8 mm diameter, 10.2 mm height) was scanned using a micro-computed tomography device (Versa XRM-520, Xradia, Pleasanton, CA) in air at an energy of 100 kVp, a current of 90  $\mu$ A and an isotropic voxel size of 10  $\mu$ m. A Gaussian filter (sigma = 1.2, support = 1) was applied to the images and bone was segmented using a global threshold determined with the Otsu method. To segment microdamage from bone, manual thresholds were chosen by an observer blinded to the amount of loading the specimen received. Stained objects smaller than 10,000  $\mu$ m<sup>3</sup> (approximately the volume of 20 osteocyte lacunae) were considered noise and removed from the images.

The volume of stained microdamage in the entire specimen was characterized as the damaged bone volume fraction (DV/BV).

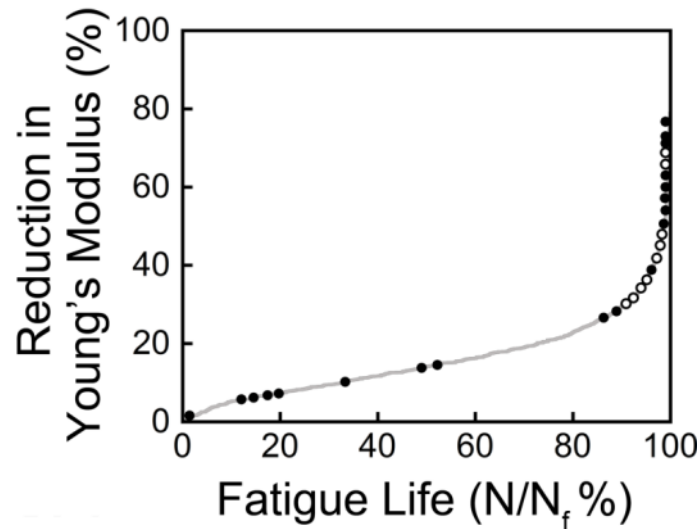


**Figure 4.1** Cyclic loading was stopped after different amounts of fatigue loading. Each circle, open and closed, represents one specimen ( $n = 32$ , 5 specimen were not loaded). The relationship between microdamage sites and resorption cavities was examined in a subset of specimens loaded to the tertiary phase (open circles only,  $n=9$ ).

#### 4.3.2 *Number, Size and Location of Microdamage*

In cortical bone, the growth of individual microdamage sites (cracks) is observed by introducing notches into specimens and tracking the growth of individual cracks while cyclic loading is applied [276]. In cancellous bone, the trabecular microstructure prevents direct observation of microdamage during mechanical testing. The accumulation of microdamage, however, occurs through a combination of the creation of new microdamage sites and/or the increase in the size of microdamage sites. The relative contribution of new microdamage sites and increases in size of microdamage sites can be inferred by examining changes in the distribution of

microdamage site sites (as illustrated in a histogram, Figure 4.2). The creation of new microdamage sites is expected to increase the height of the histogram, while an increase in the size of existing microdamage sites is expected to increase the right hand side of the histogram.

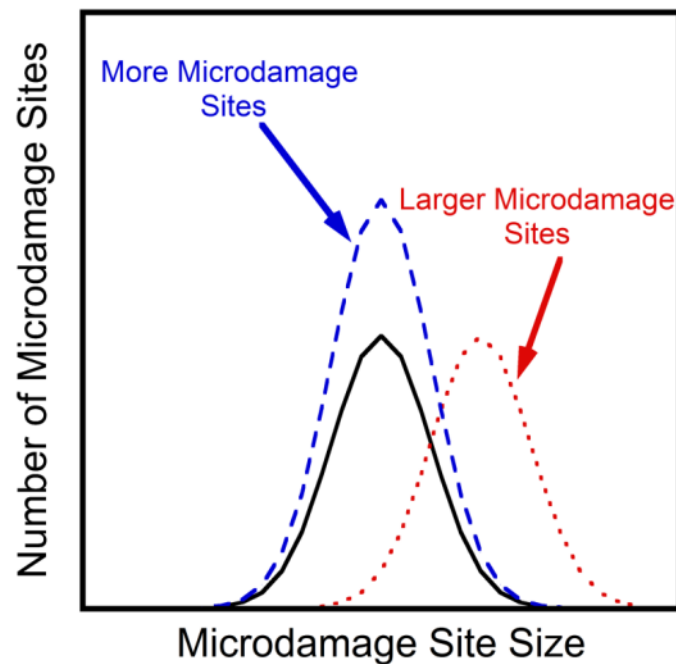


**Figure 4.2** Hypothetical normal distributions of the damage site size are shown. Following additional loading cycles there will be an increase in microdamage, either through an increase in the number of microdamage sites (blue, dashed line) or an increase in the size of microdamage sites (red, dotted line).

In cancellous bone, interstitial tissue is present in the central cores of trabeculae [266]. To determine if microdamage occurs preferentially within the interstitial regions of cancellous bone, the proportion of microdamage located more than 30  $\mu\text{m}$  from the bone surface was examined (the average maximum resorption cavity depth in human vertebral trabecular bone is 30  $\mu\text{m}$  [188]). Additionally, to

determine if microdamage was more concentrated in the interstitial tissue, the damage volume fraction of tissue near the surface ( $DV_{\text{near}}/BV_{\text{near}}$ ) and the damage volume fraction of tissue distant from the surface ( $DV_{\text{distant}}/BV_{\text{distant}}$ ) were determined.

#### **4.3.3 *Spatial correlation of microdamage and resorption cavities***

Resorption cavities on the trabecular surfaces have been implicated as stress risers that might promote microdamage formation [162, 277, 278]. To determine the effects of resorption cavities on the location of microdamage, a subset of the specimens (n=9) were submitted to higher resolution imaging (Figure 4.1). A second micro-computed tomography image was collected of the central region (3 mm diameter, 3 mm height) of each of these nine specimens using the two stage magnification capability of a micro-computed tomography device (Versa XRM-520, Xradia, Pleasanton, CA) to achieve an isotropic voxel size of 1.5  $\mu\text{m}$ , a resolution sufficient to detect individual resorption cavities based on bone surface texture [196]. Images were collected in air at an energy of 80 kVp, and a current of 7 A. Global thresholds for bone and microdamage were calculated using the two material Otsu method [256]. As above, stained microdamage sites smaller than 10,000  $\mu\text{m}^3$  were removed from the images as noise. Additionally, to eliminate non-specific surface staining (thin layers of stain that occur on bone surfaces without microdamage), lead uranyl acetate staining within 5  $\mu\text{m}$  of the surface of the trabeculae was disregarded as noise. Resorption cavities were identified based on bone surface texture (the “scaloped surface”) and traced in three-dimensions by observers blinded to the

presence of microdamage ([188], Figure 4.3). Image processing and analysis were performed using custom software written for use with Matlab (version 7.11.0, Mathworks, Natick, MA, USA) and image visualization and tracing was performed using Amira (version 5.3, Visage Imaging, San Diego, CA, USA).

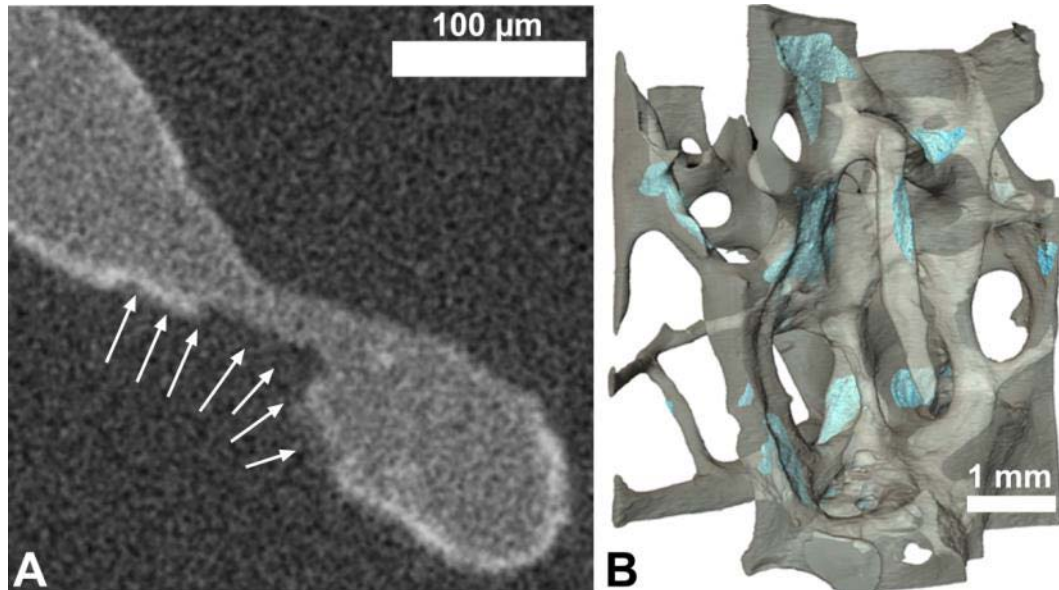


**Figure 4.3** (A) Resorption cavities were initially identified in two-dimensional micro-computed tomography images by finding eroded surfaces (arrows) and then (B) traced on three dimensional reconstructions of the micro-computed tomography images (blue).

The spatial correlation between microdamage and resorption cavities was determined using two different methodologies: 1) a volume based method; and 2) an object based method [279]. The volume based method determined the degree to which microdamage volume was more likely to be near eroded surfaces than other bone surfaces. The volume based spatial correlation was expressed as the ratio of the amount of damage volume near eroded surfaces to that of an equal amount of bone volume (selected at random) near eroded surfaces. A ratio of 1.0 indicated no spatial

correlation, a ratio greater than 1.0 indicated a positive spatial correlation (eroded surfaces were more likely to be near damage volume than other bone volume) and a value less than 1.0 indicated negative spatial correlation (eroded surfaces were less likely to be near damage volume than other bone volume). The volume based spatial correlation was then repeated to ask the converse question: if eroded surface was more likely to be near microdamage than other bone volume. The object based spatial correlation was expressed as the percentage of microdamage sites near eroded surfaces and as the percentage of resorption cavities with microdamage nearby. For both spatial correlation methods, proximity was determined at distances ranging from 8  $\mu\text{m}$  to 133  $\mu\text{m}$  (the average trabecular thickness).

#### **4.3.4 *Statistical analyses***

Regression analysis was used to determine the relationship between the number and size of microdamage sites and reductions in Young's modulus associated with fatigue loading. Donor was included as a random effect to take into account the use of multiple specimens from each donor. Differences in the damage volume fraction near and away from the bone surface were determined using a paired t-test. The spatial correlations determined using the volume based method were tested for a difference from 1.0 using a paired t-test, (a value of 1.0 indicated no spatial correlation). Statistical tests were conducted using JMP (v.20 9, SAS Institute Inc., Cary, NC, USA).

#### **4.4 Results**

Specimens experiencing greater reductions in biomechanical performance showed increased amounts of microdamage (Figure 4.4) but no significant increases in the number of microdamage sites or median microdamage site size. However, histograms of microdamage site size showed a shift to the right hand side in specimens submitted to greater amounts of fatigue loading, indicating an increased number of large microdamage sites (Figure 4.5). For the purposes of this analysis, a microdamage site was characterized as “large” if it was more than  $10^6 \mu\text{m}^3$  in volume (the 90<sup>th</sup> percentile of microdamage site volume observed in unloaded specimens). While only a small percentage of the microdamage sites were large by this criterion ( $9.9\% \pm 4.9\%$ , mean  $\pm$  SD), large microdamage sites accounted for the majority of the microdamage volume ( $69\% \pm 14\%$ ) and the number of large microdamage sites was strongly correlated with the overall damage volume fraction ( $R^2_{\text{adj}}=0.95$ ,  $p<0.001$ , Figure 4.4C). Additionally, variance in the reduction in Young’s modulus was better explained by the number of large microdamage sites ( $R^2_{\text{adj}}=0.39$ ,  $p<0.001$ , Figure 4.4B) than by the total amount of microdamage ( $R^2_{\text{adj}}=0.20$ ,  $p<0.01$ , Figure 4.4A). Reductions in Young’s modulus during cyclic loading were not correlated with the number of microdamage sites ( $p=0.16$ , Figure 4.4D) or the median size of microdamage sites ( $p=0.95$ ). Donor age was not correlated with the number or size of microdamage sites nor was donor age a covariate when comparing microdamage site number and size to reductions in Young’s modulus.

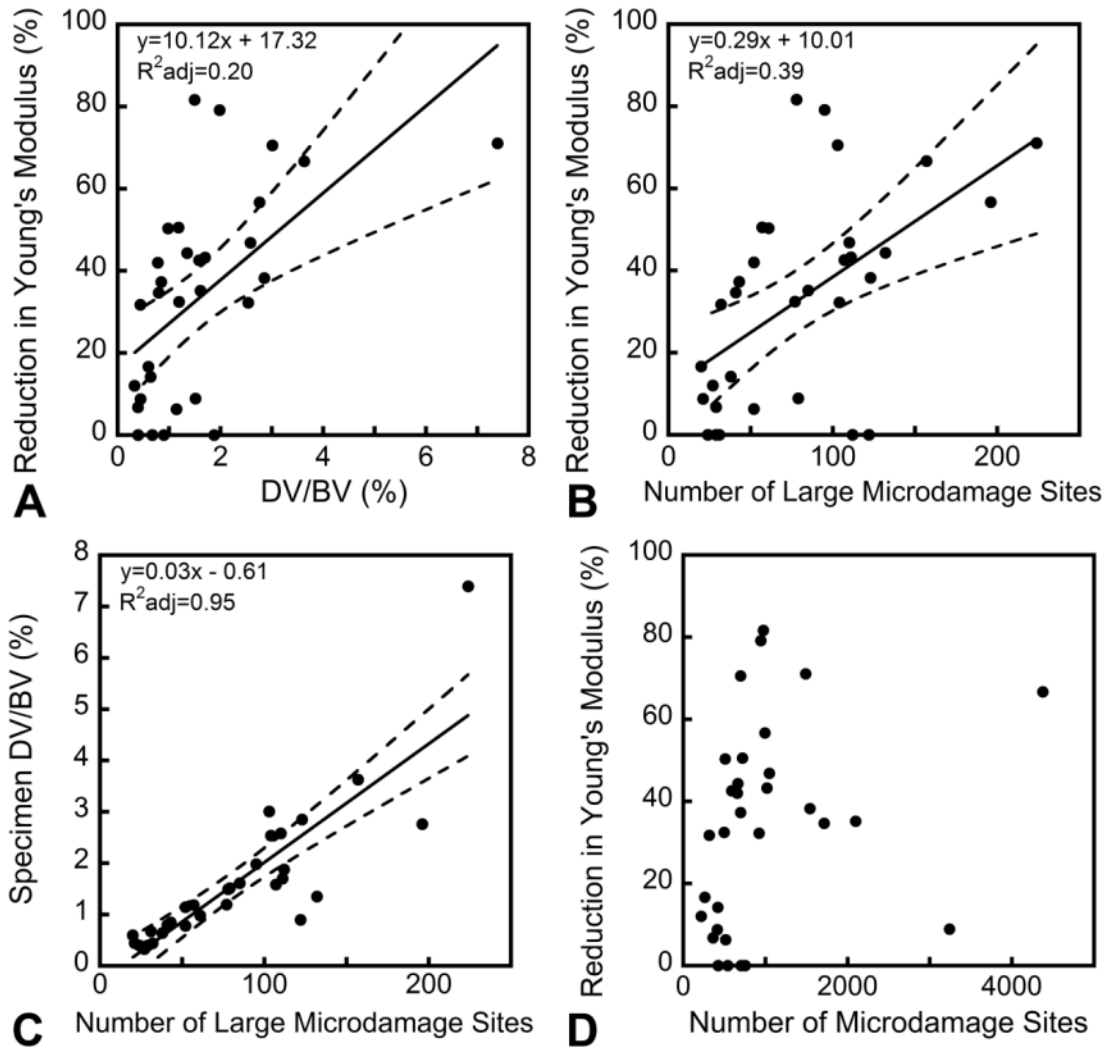


**Figure 4.4** Although the overall damage volume fraction (DV/BV) was correlated with the reduction in Young's modulus (A), the number of large microdamage sites showed a stronger correlation to the reduction in Young's modulus (B). The number of large microdamage sites was also correlated with the overall damage volume fraction (C). The overall number of microdamage sites was not correlated with the reduction in Young's modulus (D).

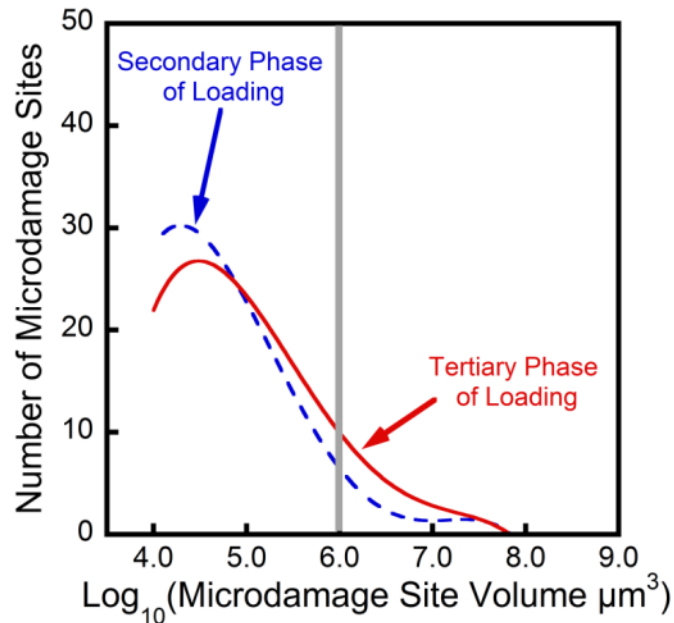


**Figure 4.5** Representative histograms of the microdamage site volumes in a specimen loaded to the secondary phase of fatigue life (dashed blue) and that of a specimen loaded to the tertiary phase of fatigue life (solid red) are shown. The grey line shows the cutoff we used for defining large microdamage sites (sites larger than  $10^6 \mu\text{m}^3$ ). The specimen loaded to the tertiary phase displayed more microdamage sites classified as large than the specimen loaded to the secondary phase.

Volume based spatial correlations indicated that microdamage was less likely to be near eroded bone surfaces than bone surfaces selected at random ( $p < 0.05$ , Figure 4.6A). Eroded surfaces were not more or less likely to have microdamage nearby (Figure 4.6B). The object-based spatial correlation indicated that most resorption cavities had microdamage nearby (Figure 4.7A), but few microdamage sites had resorption cavities nearby (Figure 4.7B). The majority ( $69.12 \pm 7.04\%$ ) of the microdamage generated by fatigue loading was distant from the bone surface ( $DV_{\text{distant}}/DV$ ). Microdamage was more concentrated distant from the bone surface ( $DV_{\text{distant}}/BV_{\text{distant}} = 2.23 \pm 1.87\%$ ) than near the trabecular surface ( $DV_{\text{near}}/BV_{\text{near}} = 0.96 \pm 0.92\%$ ,  $p < 0.001$ ).

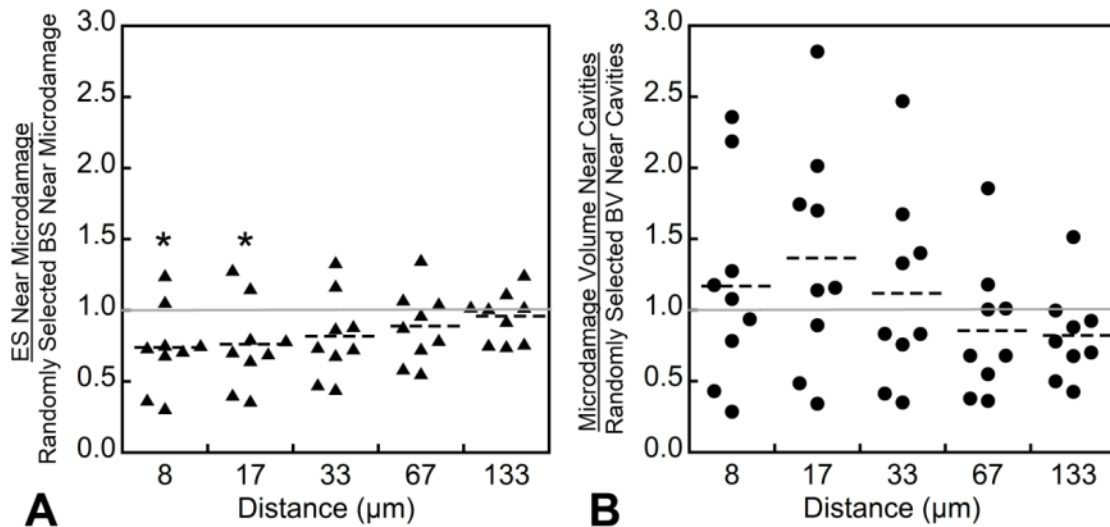


**Figure 4.6** The spatial correlations between microdamage sites and resorption cavities using the volume based method are shown. A value of 1.0 indicates no spatial correlation and a value less than 1.0 indicates a negative correlation. (A) An eroded surface was less likely to be near microdamage than regions of bone surface selected at random (at a distance of 8 and 17  $\mu\text{m}$ ). (B) No significant spatial correlations were observed when using microdamage as the predictor.

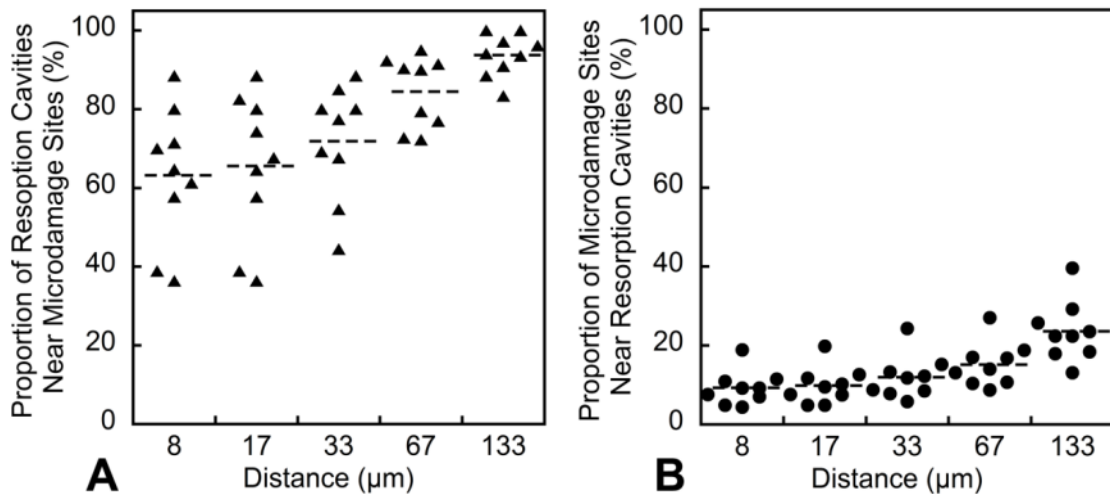


**Figure 4.7** The spatial correlations between microdamage sites and resorption cavities using the object based method are shown. While the majority of resorption cavities were near microdamage sites (A), few microdamage sites were near resorption cavities (B).

#### **4.5 Discussion**

Our finding that fatigue loading of cancellous bone leads to the creation of many small microdamage sites but most of the microdamage volume occurs in just a few large microdamage sites is consistent with the idea that bone tissue limits the growth of microdamage sites. Large microdamage sites were also more highly correlated with reductions in Young's modulus, suggesting that mechanical failure at only a few locations within the cancellous bone structure can greatly impair apparent level mechanical performance.

An increase in the number of microdamage sites following greater amounts of fatigue loading suggests initiation of new microdamage sites, while the increase in size of microdamage sites suggests the propagation or coalescence of microdamage sites later in the fatigue life. Actual observations of microdamage site extension have never been performed in a cellular solid, such as cancellous bone, and would be required to directly analyze initiation and propagation of microdamage sites. The current study did not examine microdamage morphology (crack-like v. diffuse). While some have used the ratio of the damage surface area to the damage volume (DS/DV) [127] to identify more crack-like and more diffuse like microdamage sites, because the measurement is not dimensionless (units 1/mm), DS/DV is also influenced by microdamage site size. Given the large distribution of microdamage site size in the current study, DS/DV could not reliably differentiate among microdamage morphologies. Additional analysis of microdamage morphology would be required to separate microcracks from diffuse damage.

Both the creation of new microdamage sites and the increase in size of existing microdamage sites are a result of both local tissue stresses/strains and local tissue material properties [280]. The current study examined two microstructural traits associated with increased local tissue stress/strain: resorption cavities and trabecular surfaces. Resorption cavities have received considerable attention as stress risers within cancellous bone and finite element models suggest that resorption cavities can reduce cancellous bone stiffness and strength more than would be expected from changes in bone volume fraction [162, 164, 194]. Interpretation of the spatial correlation between resorption cavities and microdamage, however, was not straightforward. In particular, our observations that microdamage volume was preferentially distant from eroded surfaces (Figure 4.6A), yet most resorption cavities had a microdamage site nearby (Figure 4.7A) at first appears contradictory. Our examination of the microdamage site size distribution (Figure 4.5), however, suggests that there were many small specks of stained microdamage in each specimen (some potentially image noise or non-specific staining), but that the large and most mechanically relevant microdamage sites were preferentially distant from resorption cavities.

The negative spatial correlation between microdamage and resorption cavities was unexpected because resorption cavities have been shown to cause local stress concentrations [162, 164]. One possible explanation is that resorption cavities in our study occurred preferentially in regions of the structure experiencing low nominal stresses such that even with the stress concentrations from resorption cavities, local stresses were not sufficient to promote microdamage. It is possible that the presence of

cavities on trabeculae may alter the load distribution within cancellous bone resulting in reduced stresses at resorption cavities. Another possible explanation is that local tissue material properties near resorption cavities influence microdamage generation. Since individual trabeculae undergo bending and torsion during apparent compression, we would expect local tissue stresses to be greater near the bone surface and therefore microdamage to be closer to the surface [88], but our analysis demonstrated just the opposite, that microdamage occurs preferentially distant from the bone surface. We suggest that the location and size of microdamage may be more influenced by tissue material properties than stress concentrations caused by micro-scale geometry.

Cancellous bone tissue displays considerable heterogeneity in tissue age and material properties. Since bone remodeling in cancellous bone occurs at trabecular surfaces, relatively younger tissue is located near the surface of trabeculae and older interstitial regions are found at the center of trabeculae [203]. We found microdamage in cancellous bone primarily distant from the bone surface, regions that we expect to contain older tissue. Our findings are consistent with previous studies that have shown that microdamage forms near the center of trabeculae [268], and are also consistent with observations in cortical bone that microdamage forms primarily in interstitial regions [135-137]. Interstitial bone tissue has been shown to have greater tissue age, reduced toughness [52], and is both stiffer and harder than the bone tissue near the surface of trabeculae [53, 77]. Therefore, the negative spatial correlation between resorption cavities and microdamage in the current study may be a result of more ductile tissue near trabecular surfaces (due to younger local tissue age). However, increased non-enzymatic glycation (a trait associated with increased tissue brittleness

[127]) has been shown to impair osteoclastic bone resorption in vitro [281] and is negatively correlated with resorption cavities in cortical bone [282]. If such a negative correlation also exists in cancellous bone it could also explain the negative correlation between microdamage and resorption cavities we observed. The possibility of a link between local tissue material properties and localization of bone resorption is intriguing and requires further study.

A strength of the study was that both microdamage sites and resorption cavities were characterized in three dimensions. Three dimensional analysis of both microdamage and resorption cavities enables characterization of the number and size of microdamage sites and reduces the variability in the measures by using the entire specimen [283]. There were also some limitations that must be considered when interpreting our findings. First, microdamage was observed using lead uranyl acetate staining. While lead uranyl acetate stains bone tissue damage, some have proposed that lead uranyl acetate stain may have limited penetration into bone surfaces [284]. However, since the majority of the microdamage we observed was distant from the bone surface, it is unlikely that limited diffusion of lead uranyl acetate influenced our conclusions. Second, as mentioned above the observed changes in microdamage site number and size suggest changes in microdamage initiation and propagation during fatigue loading, but the current study does not directly measure propagation of individual microdamage sites. The difference between our approach and direct observation of microdamage propagation was analogous to the differences between a cross-sectional clinical study (current study) and a longitudinal clinical study (where extension of individual microdamage sites is observed directly). Methods of observing

the propagation of individual microdamage sites in cancellous bone during mechanical loading are not currently available, but would be useful for understanding tissue brittleness in cancellous bone.

In conclusion, we have demonstrated that degradation in biomechanical performance of trabecular bone during fatigue loading can be attributed to a few, large microdamage sites. Microdamage appears primarily distant from resorption cavities and the trabecular surface and is consistent with the idea that the locations of microdamage initiation and propagation under fatigue loading is determined more by tissue material properties/tissue heterogeneity than stress concentrations associated with microscale geometry. Our results therefore highlight the importance of tissue material properties in failure processes in cancellous bone.

#### ***4.6 Acknowledgements***

Research reported in this publication was supported by the National Institute of Arthritis and Musculoskeletal and Skin Diseases of the National Institutes of Health (U.S) under Award Number AR057362 (PI CJH). The content is solely the responsibility of the authors and does not necessarily represent the official views of the National Institutes of Health. We acknowledge use of human vertebral bodies provided by the National Disease Research Interchange (NDRI), with support from NIH grant 8U42OD011158-22. For technical support, we thank Garry Brock, Kathy Ehlert, Daniel Brooks and Christopher Chapa for technical assistance and Mark Riccio and Fred von Stein for imaging assistance.

Authors' roles: Conceived and designed the experiments: MGG, FML, CMR, CJH.

Analyzed data: MGG, TMN, JJ, FML. Wrote the paper: MGG, CJH. Critical revision and final approval of the manuscript: MGG, FML, TMN, JJ, CMR, CJH.

## CHAPTER 5

### **Relationship Between Microdamage and Tissue Level Strains**

#### **5.1 Abstract**

High-resolution finite element models derived from micro-computed tomography images are the primary tool for relating apparent loading on cancellous bone to local tissue stresses/strains. Finite element models are often used to study the effects of trabecular microarchitecture and loading mode on tissue stress, but the degree to which existing finite element methods predict local tissue failure is not well understood. In the current study, we determined the relationship between local tissue strains determined from high resolution finite element models and tissue microdamage determined using three-dimensional imaging. Microdamage was generated in-vitro in human vertebral cancellous bone (n=14 specimens, 8 male donors, 2 female donors, 47-78 years of age). Microdamage was 50 -75% more likely to form at regions of tissue experiencing principal strains exceeding 0.4% than elsewhere. Tissue microdamage was spatially correlated with the regions of greatest tissue strain estimated using finite element models. Furthermore, the spatial correlation was most pronounced at the largest sites of microdamage, which have been associated with the largest degradation in apparent mechanical properties of cancellous bone. Additionally, 87% of the largest microdamage sites were located at tissue experiencing the principal strains exceeding 0.4%. Together, these findings

demonstrated that even simple, linear elastic finite element models were capable of predicting the locations of the most influential microdamage sites in cancellous bone.

## **5.2 Introduction**

Impaired bone tissue material toughness has been associated with increased risk of fragility fracture in patients with diabetes and patients undergoing bisphosphonate treatment [264, 265]. Recent efforts to understand failure mechanisms in bone have concentrated on tissue material toughness and resistance to the formation of tissue microdamage. Small amounts of microdamage (occupying less than 2% of the tissue) result in large reductions in stiffness, strength, and fatigue life of cancellous bone [78, 134], highlighting the potential importance of tissue microdamage to clinical fractures.

High resolution finite element models, derived from three-dimensional images of trabecular bone microstructure, are the primary means of estimating tissue level stress and strain in cancellous bone. Modern high-resolution finite element models of cancellous bone are capable of predicting apparent yield strength and are often used to estimate the amount of tissue damage generated by overloads [95, 99, 102, 285, 286]. However, there have been few attempts to relate finite element-derived tissue strains to microdamage measured using histology. The few studies that have addressed the topic have not done so directly, either demonstrating that the total volume of microdamage generated is correlated with the volume of failed tissue predicted by finite element models [110, 287] or that the locations of “severe” microdamage

display greater than average local tissue stresses [108, 269]. None of the studies reported to date have asked how well finite element models predict the locations of microdamage generation within cancellous bone. Finite element models of cancellous bone suggest that loading mode (apparent tension, compression, shear) influences tissue level yielding [95, 193]. Experimental investigations have shown that loading mode influences the amount and location of microdamage [288, 289], specifically tensile loading causes greater amounts of tissue microdamage than compressive loading [183]. Hence, the relationship between finite element derived tissue strains and microdamage generation is likely influenced by apparent loading mode.

The long-term goal of the current work is to understand how tissue level toughness in cancellous bone influences whole bone fracture. Here, we determine how well finite element models are able to predict the locations of microdamage generation in cancellous bone. Specifically we determine the spatial relationship between microdamage and tissue level strain predicted by finite element models following two different loading modes: apparent tension and apparent compression.

### ***5.3 Methods***

Here we perform an additional analysis of specimens described in a previous study [183]. In section 5.3.1 we review the experimental methods of our prior study and in sections 5.3.2-5.3.5 we describe the methods novel to the current study.

### 5.3.1 *Study design*

Specimens were collected from the L4 vertebral bodies of 10 donors (n=14, 8 male, 2 female, 47-78 years of age, tissue from NDRI, Philadelphia, PA). The donors had no history of metabolic bone disease and displayed no obvious vertebral deformities. Cylinders of cancellous bone, 8 mm diameter and nominally 25-30 mm height, oriented in the cranial-caudal direction were collected. Specimens were stored at -20 °C. Prior to loading, micro-computed tomography images of each sample were obtained at an isotropic voxel size of 10  $\mu\text{m}$  (Scanco  $\mu\text{CT}$  20, Scanco Medical AG, Brüttisellen, Switzerland). Additionally, specimens were stained with xylenol orange (0.5 mM in PBS, 2 h) prior to loading to label preexisting damage.

Specimens were potted into brass fixtures using bone cement (as previously described [290]) and submitted to 0.8% strain (apparent yield) in tension (n=6) or compression (n=8) at a rate of 0.5%/s. Apparent level yield strain and Young's Modulus were determined from the stress-strain curve. Following loading, the central 5 mm length of each specimen was cut from the center of the exposed gage length with a low speed diamond saw and the specimens were submitted to calcein staining (0.5 mM in PBS, 2h) to identify microdamage generated during loading. Specimens were then embedded undecalcified in methyl-methacrylate. Three-dimensional images of bone and fluorescent labels of microdamage were acquired at a voxel size of 0.7 x 0.7 x 5  $\mu\text{m}^3$  using serial milling [195, 291]. Bone and fluorescent labels were segmented using manually determined global thresholds. Images were then smoothed to correct for cutting marks left by the serial milling technique. The region of interest

examined included the central region of the specimen image (5.4 mm diameter, 4 mm height) thereby avoiding microdamage caused during specimen preparation. To eliminate the possibility of non-specific surface staining (thin layers of stain that occur on bone surfaces that are ignored when making manual microdamage counts), microdamage stain within 5.6  $\mu\text{m}$  of the surface of the trabeculae was removed from the images. Microdamage generated by loading was identified as bone tissue displaying calcein (post-loading stain) in the absence of xylenol orange (pre-loading stain).

### **5.3.2 *Finite element modeling***

To reduce computational expense, micro-computed tomography were down-sampled to an isotropic voxel size of 20  $\mu\text{m}$  using a region averaging technique [290]. A voxel size of 20  $\mu\text{m}$  is less than one-fourth the mean trabecular thickness and is sufficient for high resolution finite element models of bone [84, 85]. Bone was identified using a manually determined global threshold. Each voxel was converted into a linear elastic, eight node brick element. Linear elastic models indicate the locations of the greatest stresses/strains, where the majority of microdamage sites should initiate. Elements were assigned a Young's modulus of 10 GPa and a Poisson's ratio of 0.3 [290]. The caudal surface of the model was fully constrained and a 0.8% apparent strain was applied to the cranial surface to simulate the physical loading conditions (either tensile or compression). Finite element models were implemented using Olympus [292] on a Sun Constellation Linux Cluster (Ranger; TACC, TX,

USA). Tissue principal strains were measured at the centroid of every element [285]. The most positive principal strains are referred to as tissue tensile principal strains and the most negative principal strains are referred to as tissue compressive principal strains.

### **5.3.3 *Probability of microdamage at finite element modeled strain***

To determine how well local tissue strains predict the locations of microdamage, the probability of observing microdamage was determined as a function of principal strain magnitude. Images of microdamage were down-sampled from to match the image resolution used in the finite element models (20  $\mu\text{m}$ ). Regions of microdamage within 28  $\mu\text{m}$  of each other were considered to be part of the same microdamage site. Microdamage sites smaller than 64,000  $\mu\text{m}^3$  (eight voxels) were characterized as noise and removed from the images. Images of microdamage were then registered to the finite element models accounting for rotation, translation, scaling and shearing (Amira version 5.4 Visage Imaging, San Diego, CA, USA). Tissue principal strains were binned (0.04% bin size) and the probability of observing microdamage at was estimated as follows:

$$Probability = \frac{DV \text{ at strain}}{BV \text{ not at strain}} \quad \text{Eq. 1}$$

#### **5.3.4 *Spatial correlation of microdamage and highly strained tissue***

The spatial correlation between microdamage and highly strained tissue was assessed in two ways: 1) a spatial correlation based on volume (volume-based method) and 2) a spatial correlation of discrete objects (object number-based method) (Figure 5.1) [279]. The volume-based method determined the degree to which microdamage volume was more likely to be near highly strained tissue than other regions of the bone. The volume-based spatial correlation was expressed as the ratio of the amount of microdamage volume near highly strained tissue to that of an equal amount of bone volume (selected at random) that was near highly strained tissue. A ratio of 1.0 indicated no spatial correlation, a ratio greater than 1.0 indicated a positive spatial correlation (microdamage was more likely to be near highly strained tissue than other bone volume), and a value less than 1.0 indicated negative spatial correlation (microdamage was less likely to be near highly strained tissue than other bone volume). The volume-based spatial correlation was then repeated to ask the converse question: if highly strained tissue was more likely to be near microdamage than other regions of the bone. The object number-based spatial correlation was expressed as the percentage of microdamage sites near highly strained tissue as well as the converse question (the percentage of highly strained tissue sites near microdamage). For both spatial correlation methods, proximity was determined at distances ranging from 0  $\mu\text{m}$  to 60  $\mu\text{m}$  (~ half of the average trabecular thickness).

The spatial relationship between microdamage and large tissue level strains will vary based on the magnitude of tissue strains characterized as “large.” A

parametric analysis was performed to determine the tissue strain magnitude that best predicted the locations of microdamage. Highly strained tissue was defined as tissue experiencing principal strains that exceeded a value ranging from 0.1% to 1%. As with the images of microdamage, regions of highly strained tissue smaller than  $64,000 \mu\text{m}^3$  (eight voxels) were characterized as noise and not included in the spatial correlation analysis.

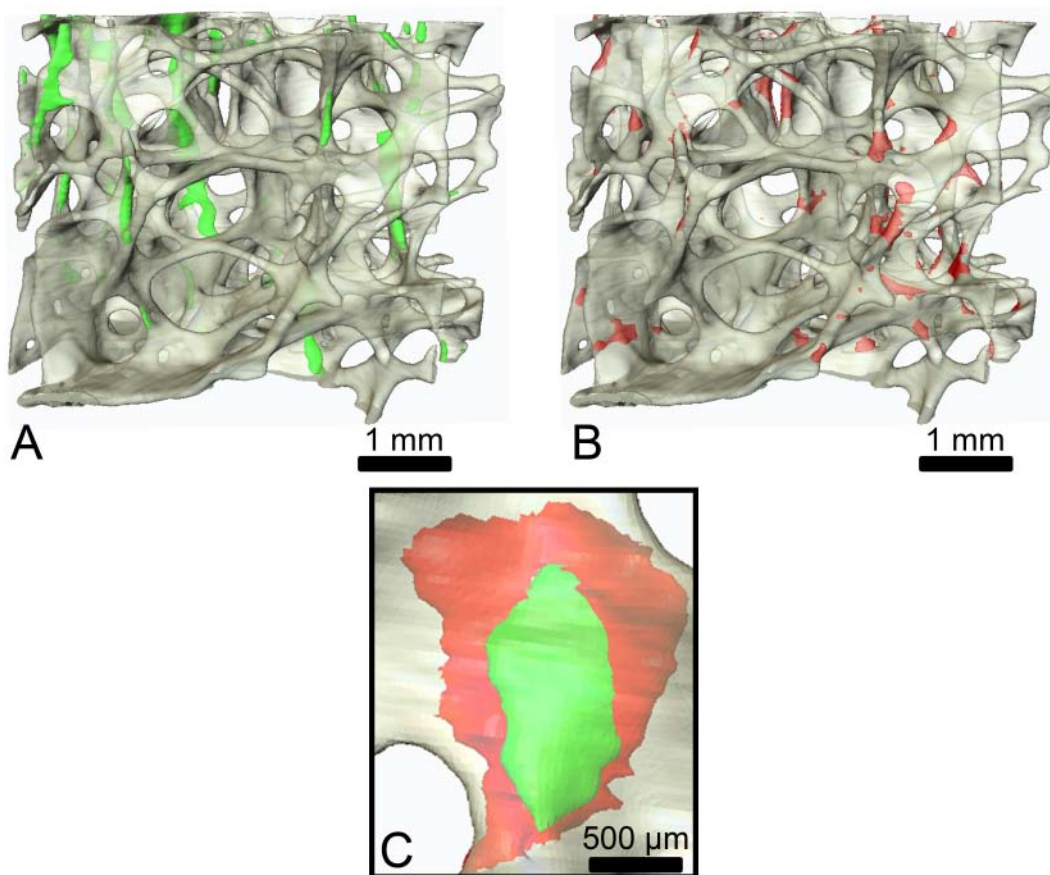


**Figure 5.1** A specimen of cancellous bone is shown. (A) Highly strained tissue is indicated in green. (B) Microdamage is indicated in red. (C) Image registration was used to determine the spatial associations between microdamage and highly strained tissue.

### **5.3.5 Statistical analyses**

The magnitudes of principal strain in regions of microdamage and the rest of the bone were compared using a two-tailed paired t-test. Regression analysis was used to determine the relationship between strain predicted by finite element modeling and the probability of microdamage. The spatial correlations determined using the volume-based method were tested for a difference from 1.0 using a two-tailed paired t-test, (a value of 1.0 indicated no spatial correlation). All data is presented as mean  $\pm$  SD. Statistical tests were conducted using JMP Pro (v.11, 2013, SAS Institute Inc., Cary, NC, USA).

### **5.4 Results**

The relationship between microdamage and local tissue strain differed between specimens loaded in tension and those loaded in compression. In specimens submitted to loading under apparent tension, the local principal strains were greater at microdamage than away from microdamage (tension:  $0.32 \pm 0.09\%$  v.  $0.20 \pm 0.05\%$ , compression:  $0.14 \pm 0.03\%$  v.  $0.11 \pm 0.02\%$ , Figure 5.2A). Additionally, the probability of observing microdamage at a location in the microstructure was positively correlated with local tensile principal strain but was not predictive ( $p < 0.0001$ ,  $R^2 = 0.30$ , Figure 5.3A). Local compressive principal strain showed no correlation with microdamage. Overall, the probability of observing microdamage was

50-75% greater at tissue tensile strains above 0.4% as compared to the average incidence of microdamage (Figure 5.3A).

In specimens submitted to apparent compression, the tissue principal strains were greater at microdamage than away from microdamage (tension:  $0.14 \pm 0.02\%$  v.  $0.12 \pm 0.01\%$ , compression:  $0.31 \pm 0.06\%$  v.  $0.22 \pm 0.03\%$ , Figure 5.2B). The probability of observing microdamage at a location in the microstructure was positively correlated with local compressive principal strains but was not predictive ( $p < 0.0001$ ,  $R^2 = 0.08$ , Figure 5.3B). No correlation between the probability of microdamage and tissue tensile principal strain was observed. Overall, the probability of microdamage was 50-75% greater at tissue tensile strains above 0.4% as compared to the average incidence of microdamage (Figure 5.3B).

Microdamage was located near highly strained tissue. The volume-based spatial correlation indicated a significant positive correlation between highly strained tissue and microdamage volume (Figure 5.4, C.1, and C.2). Over half of microdamage sites were located at tissue experiencing a principal strain of 0.4% or higher; however, less than half of the highly strained tissue sites were located at microdamage (Figure 5.5 and C.4).

The magnitude of strain used to classify highly strained tissue had limited influence on the volume-based spatial correlations. The volume-based spatial correlations were greatest when the magnitude of strain used to define highly strained tissue was 0.4% or greater (Figure 5.4B and C.2). The object number-based spatial correlation, however, was quite sensitive to the strain magnitude used to classify highly strained tissue (Figure 5.5C,D and C.4).

As large microdamage sites (sites over  $1,000,000 \mu\text{m}^3$  in volume) have been shown to be the most influential biomechanically [293], we also the spatial correlation assays looking only at large microdamage and highly strained tissue sites. Most of the microdamage volume ( $86\% \pm 8\%$ ) was located in a small number of large microdamage sites (microdamage sites exceeding  $1,000,000 \mu\text{m}^3$  in volume). Similarly, most of the highly strained tissue volume ( $89\% \pm 5\%$ ) was located in a few large sites. When only large microdamage and highly strained tissue sites were considered, strong volume based and object number-based spatial correlations were observed between microdamage sites and highly strained tissue sites (Figure 5.6A,B, C.3,and C.5).

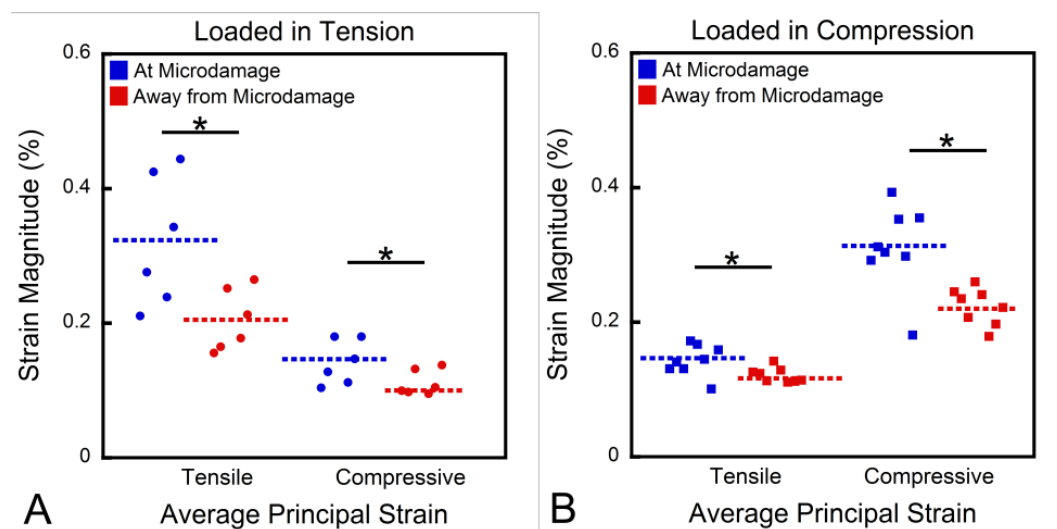


**Figure 5.2** Tissue tensile and compressive principal strains were greater at locations of microdamage as compared to other regions of the microstructure. ( $p < 0.05$ )

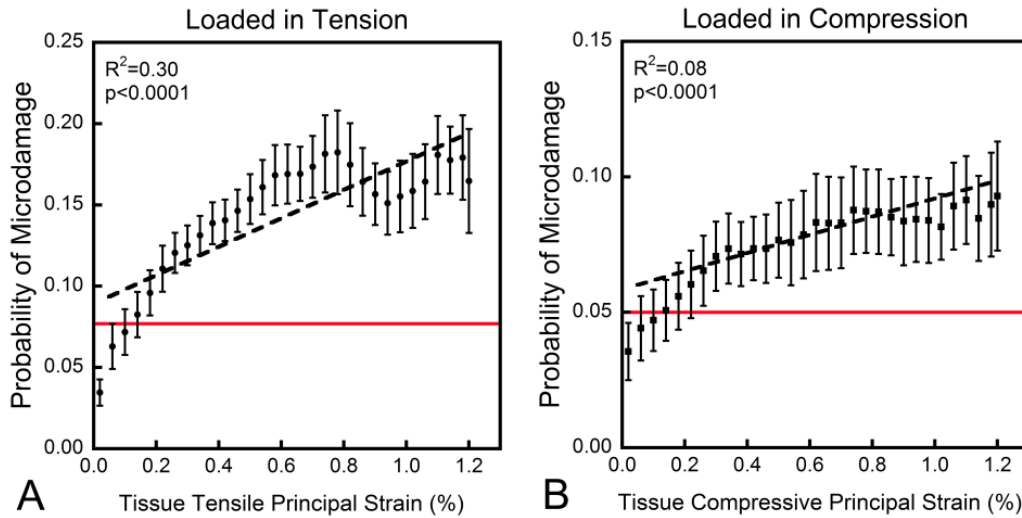


**Figure 5.3** (A) In specimens loaded in tension, the probability of microdamage was positively correlated with tissue tensile principal strains. (B) In specimens loading in compression, the probability of microdamage was positively correlated with tissue compressive principal strains. The average probability of microdamage occurring in the specimens is shown in red.

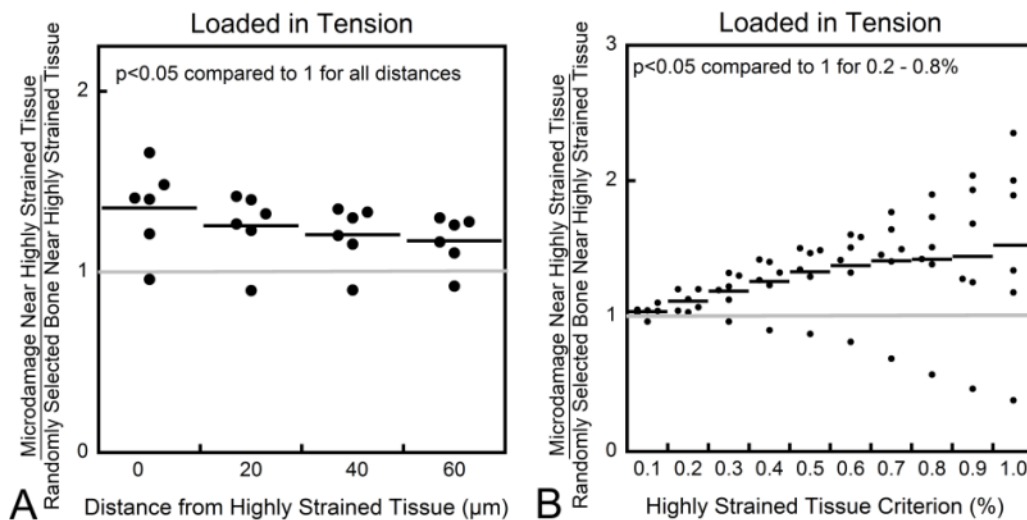


**Figure 5.4** The volume-based spatial correlations are shown. A value greater than 1.0 indicates a positive spatial correlation. (A) The spatial correlation between microdamage and highly strained tissue (defined as strain greater than 0.4%) with respect to distance between the volumes is shown. (B) The spatial correlation between microdamage and highly strained tissue was greatest when the magnitude of strain used to define highly strained tissue exceeded 0.4%. Similar trends were seen for specimens loaded in compression (see Figure C.1, C.2).

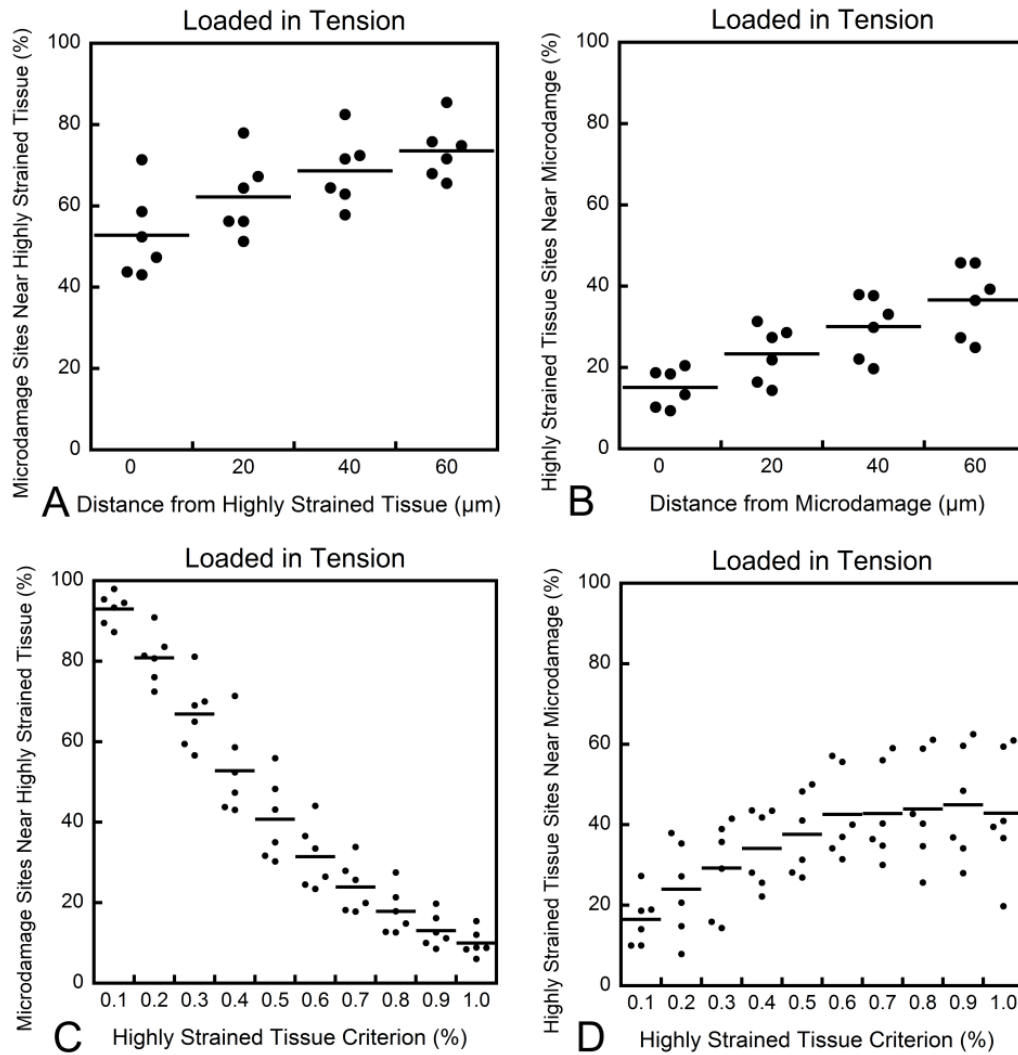


**Figure 5.5** The object number-based spatial correlations are shown. The percentage of (A) microdamage sites near highly strained tissue and (B) highly strained tissue sites near microdamage increased as the distance between the objects increased. (C) The percentage of microdamage sites near highly strained tissue was inversely proportional to the strain magnitude used to define highly strained tissue. (D) Sites of highly strained tissue were not commonly located near microdamage. Similar trends were seen for specimens loaded in compression (see Figure C.4).

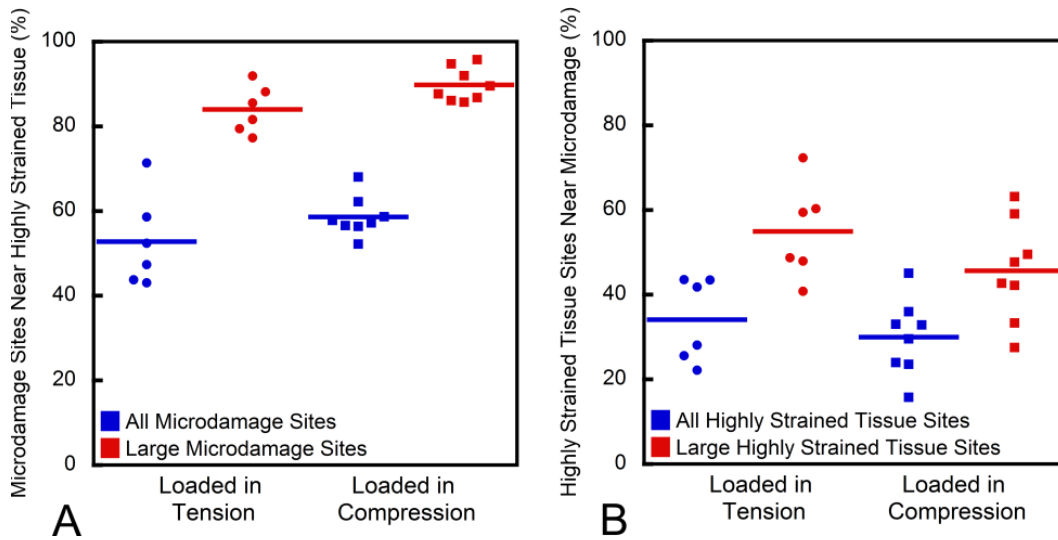


**Figure 5.6** The object number-based spatial correlation is shown for all microdamage sites as well as only the largest microdamage sites ( $>1,000,000 \mu\text{m}^3$ , shown only for coincident locations, distance =  $0 \mu\text{m}$ ). When only the largest sites were considered, both the percentage of microdamage sites near highly strained tissue (A) and the percentage of highly strained tissue sites near microdamage (B) increased.

### 5.5 Discussion

Here we present the first three dimensional examination of the spatial correlation between microdamage and local tissue strains in human cancellous bone. We found that microdamage was most likely to occur at the greatest tissue level principal strains. The largest microdamage sites were spatially correlated with the largest regions of high tissue strain determined with finite element models. Therefore our findings demonstrate surprising effectiveness of linear elastic finite element models to predict the locations of the largest (and most biomechanically relevant [293]) microdamage sites.

While the linear elastic finite element models were useful for predicting the locations of the largest microdamage sites, the models were not able to predict the

location of all of the microdamage sites. Since the strains predicted by linear elastic finite element models will deviate from the actual tissue strain once the tissue begins to yield, we did not expect the tissue strains to dictate the location of all of the microdamage but we did expect most of the sites experiencing the greatest tissue strains to coincide with microdamage. Regions with the greatest tissue strain magnitudes were more likely to develop microdamage, but even at the locations of greatest tissue strain, the probability of observing microdamage was relatively low (~20%, Figure 5.3). Furthermore, if we consider only the locations with the greatest tissue strains (right hand side of Figure 5.5B) we see that locations of the greatest tissue strains were rarely near microdamage.

There are a number of strengths to the current study that support our conclusions. First, the spatial correlation between highly strained tissue and microdamage was determined using three different assays (probability of microdamage at strain magnitudes, volume-based spatial correlation and object number-based spatial correlation). Second, both the analysis of microdamage and tissue level strain was performed in three dimensions. Three dimensional analysis reduces the variability in the microdamage measurement by using the entire specimen [283] and is able to take into consideration out-of-plane spatial relationships between microdamage and tissue level strain.

There are some limitations that must be considered in interpreting our results. First, as mentioned in our interpretation above, the current analysis used linear elastic finite element models, which do not account for the effects of tissue yielding on the stress/strain distribution within cancellous bone. However, the current study examined

loading to apparent yield and at such small magnitudes of apparent strain there are only negligible differences between linear and non-linear models in terms of the amounts of tissue exceeding yield [285]. Second, microdamage was stained using a bulk fluorochrome stain, which stains most but not all regions of permanent deformation in bone tissue [294]. Hence, the relationship seen between local tissue stress/strain and microdamage should be considered a conservative estimate.

Our findings provide insight into the best approaches for improving models of microdamage formation in cancellous bone. The most common advancement in high resolution finite element modeling is the use of a nonlinear constitutive model, which has been shown to enable prediction of apparent yield properties [95, 193] and describe changes in stress/strain distribution after tissue level yield occurs. However, initial tissue yielding in nonlinear models will coincide with regions of the greatest tissue strains observed in linear elastic models. Our observation that few of the microdamage sites were near the locations of greatest tissue strain in the linear elastic finite element models suggests that constitutive models with tissue nonlinearities alone would provide relatively little improvement toward predicting the locations of tissue microdamage. A more likely explanation for microdamage not being located at the predicted locations of greatest tissue strain is heterogeneity in tissue material properties. When a heterogeneous tissue modulus is included in linear finite element models, the distribution of stress/strain is altered [77, 87]. Therefore, incorporating tissue heterogeneity is more likely to improve the prediction of the locations of microdamage than including tissue nonlinearities.

Our findings are consistent with prior reports showing that regions of

microdamage experience greater tissue strains [108, 269]. The magnitude of tissue compressive principal strain at microdamage and away from microdamage in the current study (0.32%, 0.20%) was similar to the results reported by Narajaga and colleagues [269] (0.33%, 0.19%). Additionally, in the current work, microdamage was spatially correlated with tissue experiencing a tissue principal strain greater than 0.4%, a tissue strain similar to the tensile yield strain criterion used in prior work (0.33% - 0.61%) [95, 99, 102]. However, in prior work the compressive yield strain criterion was larger than the tensile yield strain criterion while in the current work the same strain magnitude was associated with microdamage in tension and compression. A likely explanation for the difference between our findings and others is that prior studies were estimating the tissue level yielding, which is not the same as microdamage generation.

In conclusion, we have demonstrated that linear elastic finite element models can be used to predict the locations where large microdamage sites will form in cancellous bone following either tensile or compressive loading. Furthermore, incorporating heterogeneity in tissue level material properties is more likely to improve the predictive capabilities of finite element models than including nonlinearities in the model.

## ***5.6 Acknowledgements***

Research reported in this publication was supported by the National Institute of Arthritis and Musculoskeletal and Skin Diseases of the National Institutes of Health

(U.S) under Award Number AR057362 (PI CJH). The content is solely the responsibility of the authors and does not necessarily represent the official views of the National Institutes of Health. We acknowledge use of human vertebral bodies provided by the National Disease Research Interchange (NDRI), with support from NIH grant 8U42OD011158-22. We thank Ivana H. Yi and Michael G. Jekir for performing the mechanical tests.

## CHAPTER 6

### Summary and Future Directions

#### 6.1 *Summary*

Insufficiency fractures are associated with impaired material and structural properties and primarily occur in regions of the skeleton dominated by cancellous bone [17, 18]. In cancellous bone, the accumulation of microdamage is associated with a loss in biomechanical performance [78, 134]; therefore, the objective of this research was to understand the development of microdamage in cancellous bone. Specifically, we used novel three-dimensional imaging techniques to examine how microdamage affects the biomechanical performance of cancellous bone and how microstructural features of cancellous bone influence the location of microdamage accumulation.

While the overall accumulation of microdamage in cancellous bone has been explored, the number, size and location of microdamage sites have not been examined. In cortical bone, structural features such as the cement lines around osteons deflect and arrest the progress of microcracks, and the majority of microdamage occurs in the interstitial bone tissue [135-138]. However, both the microarchitecture and ultrastructure of cancellous bone differ from cortical bone, and relatively little is known about the development of microdamage in cancellous bone. Additionally, resorption cavities in cancellous bone are believed to act as stress risers and influence the accumulation of microdamage [162, 164]. While the manner in which

microdamage accumulates in cancellous bone has been examined [186, 267-271], the spatial relationship between resorption cavities and microdamage has not been examined.

### **6.1.1 Aim 1**

In this aim, we characterized the size and location of resorption cavities in three-dimensions. The majority of resorption cavities were located at nodes. Resorption cavities not located entirely on a node were preferentially located on longitudinally oriented plate-like trabeculae. Longitudinally oriented plate-like trabeculae are expected to carry a larger portion of the load in the vertebrae, and computational models have predicted that tissue yielding preferentially occurs at longitudinally oriented plate-like trabeculae [110, 222]. On average, resorption cavities were  $30.10 \pm 8.56 \mu\text{m}$  in maximum depth,  $80.60 \pm 22.23 \times 10^3 \mu\text{m}^2$  in surface area and  $614.16 \pm 311.93 \times 10^3 \mu\text{m}^3$  in volume. The ratio of maximum cavity depth to local trabecular thickness was  $30.46 \pm 7.03\%$ , and maximum cavity depth was greater on thicker trabeculae. Additionally, cavities that formed on plate-like trabeculae were larger than cavities that formed on rod-like trabeculae. Based on the size of the resorption cavities, the local stresses around resorption cavities are increased by 2-3 times [223]. Therefore, we expected resorption cavities to play a significant role in modifying the local tissue stresses and influencing the formation of microdamage.

### 6.1.2 *Aim 2*

In this aim, we developed several spatial correlation techniques. Both spatial correlation techniques are used to determine the proximity of two sets of objects, i.e. type A and type B objects. The first spatial correlation technique is a volume based spatial correlation. The ratio of the volume of type A objects near type B objects to the volume of a random distribution of type A object volume near type B objects is calculated. If the ratio is greater than one, type A objects are preferentially located near type B objects and the spatial correlation is positive. If the ratio is equal to one, no spatial correlation exists. If the ratio is less than one, type A objects are preferentially located away from type B objects and there is a negative spatial correlation. The second spatial correlation technique is an object based spatial correlation. The percentage of type A objects near type B objects is calculated. Both spatial correlation techniques are done at several distances to determine if the spatial correlation exists at a specific distance rather than only when the objects overlap. The spatial correlation techniques were used to examine if small misalignments that occur during in-vivo loading affect where finite element models predict the regions of highest stress occur. Finite element models of rat vertebrae were created and a parametric analysis was performed to examine the effects of misalignment in orientation. In the cancellous bone portion of the model, the locations of high stress were not affected by misalignments in the loading orientation. In the cortical bone portion of the model, the locations of high stress were only affected by angular misalignments in the dorsal direction.

### **6.1.3 Aim 3**

In this aim, we examined the relationship between the number and size of microdamage sites and reductions in biomechanical performance. Additionally, we determined the spatial relationship between microdamage, bone surfaces and resorption cavities. Neither the number nor the average size of microdamage sites were correlated with reductions in biomechanical performance. However, the overall damage volume was dominated by relatively few large microdamage sites, with 10% of the microdamage sites accounting for 70% of the microdamage volume. The number of large microdamage sites was correlated with reductions in the apparent Young's modulus of the specimen. This result suggests that only a few large microdamage sites affected the biomechanical performance of cancellous bone following fatigue loading. Microdamage sites were preferentially located away from resorption cavities and 70% of the microdamage volume was located more than 30  $\mu\text{m}$  from the surface of trabeculae. Since the central regions of trabeculae are older and stiffer [52, 53, 77], material properties rather than stress concentrations caused by micro-scale geometry appear to affect the development of microdamage.

### **6.1.4 Aim 4**

In this aim, we determined the ability of finite element models to predict locations where microdamage forms in cancellous bone. Cylinders of cancellous bone were imaged using micro-computed tomography and then loaded either in tension or

compression. The distribution of strain in the cancellous bone was measured using finite element models created from the micro-computed tomography images.

Microdamage was located at regions of higher principal strain than the rest of the bone tissue. Additionally, microdamage in specimens loaded in tension was more likely to occur at high tensile principal strains while microdamage in specimens loaded in compression was more likely to occur at high compressive principal strains. Finite element models were capable of predicting the location the largest and most biomechanically relevant microdamage sites.

#### **6.1.5 *Synthesis***

The studies contained in this thesis demonstrate how microdamage forms relative to local stresses and stress concentrations. The results of the first study indicate that resorption cavities should act as stress concentrations based on the size and location of resorption cavities. Hence, based purely on the structure of cancellous bone, microdamage should preferentially form at resorption cavities. However, using the novel spatial correlation techniques developed in the second study, the results from the third study reveal that microdamage preferentially forms away from resorption cavities. Furthermore, microdamage preferentially forms near the center of trabeculae. The tissue at center of trabeculae has been shown to be older and stiffer than the tissue near surface [53, 77, 203]. Therefore, the tissue-level material properties appear to dictate the location of microdamage formation. In the fourth study, linear elastic finite element models were used to predict the location of microdamage in cancellous bone.

While linear elastic models are not able to predict the post tissue-yield distribution of stress and strain, the locations experiencing the greatest strain in the models should be coincident with microdamage sites. However, the locations in the models experiencing the greatest strains were no often co-located with microdamage. The most likely explanation for microdamage not being located at the predicted locations of greatest tissue strain is heterogeneity in tissue material properties [77, 87]. Additionally, the results of the third study demonstrate that the largest microdamage sites have the largest influence on the degradation of the biomechanical performance of cancellous bone following cyclic loading. Therefore, techniques that prevent microdamage sites from propagating will have a greater influence on the biomechanical performance of cancellous bone than techniques that prevent microdamage sites from initiating.

#### **6.1.6 *Strengths***

The primary strength of this work is that all measurements and spatial correlations were performed in three-dimensions. By making measurements in three-dimensions, we reduced the variability by incorporating information from the entire specimen [232, 283] and accounted for out-of-plane spatial relationships. Two-dimensional measures of resorption cavities require assumptions when measuring cavity depth and are unable to determine the breadth, volume, and location in the trabecular microarchitecture of resorption cavities. Additionally, resorption cavities were identified initially due to scalloped surfaces in two-dimensional images followed

by a secondary confirmation of the cavity as an indentation of the bone surface in three-dimensions.

Several other strengths support the current findings. First, all of the bone samples were from human donors. While examining animal models is a useful starting point for understanding how microdamage develops in bone tissue, the microarchitecture differs based on species [295, 296]. Therefore, examining human tissue was necessary when attempting to understand the relationship between microdamage and resorption cavities. Second, the development of microdamage was examined by using computational models and physically loaded samples. Microdamage should theoretically form at locations where the stresses and strains were highest but in cancellous bone it was not possible to directly measure the tissue level stresses and strains. By using computational models in conjunction with physically loaded bone specimens, it was possible to determine to what degree structural and material aspects of the cancellous bone influenced microdamage accumulation.

### **6.1.7 *Limitations***

Several limitations need to be considered when interpreting the current work. First, both fluorescent dyes and lead uranyl acetate potentially do not penetrate deep enough into the bone tissue to label all of the microdamage [284, 294]. However, since the majority of the microdamage was located distant from the surface, it is unlikely that under-staining of the microdamage affected the measurements in the current

work. Second, homogenous material linear elastic finite element models with homogenous material properties were used to calculate the distribution of stress/strain in the cancellous bone. The distribution of stresses and strains was altered when incorporating heterogeneous material properties into finite element models and when using non-linear finite element models [87, 94, 102, 297, 298]. Therefore, more complicated models will be necessary to understand how microdamage develops in cancellous bone following diseases and drug treatments. Third, while the findings in this thesis suggest that tissue-level heterogeneity influences the accumulation of microdamage in cancellous bone, the tissue-level material properties were not directly measured. Future work that examines the material properties around resorption cavities and microdamage will help to further elucidate the mechanisms behind microdamage development. Finally, all experiments were performed ex-vivo and unable to examine the process of microdamage repair.

## ***6.2 Future Work***

The results of the current work establish the foundation for several avenues of future study into how microdamage develops and is repaired in cancellous bone. Although the largest stresses are expected at resorption cavities, microdamage preferentially forms distant from resorption cavities. Therefore, a mechanism exists that prevents microdamage from forming at microdamage and may be elucidated by examining the material properties around resorption cavities. Furthermore, the majority of microdamage forms in the older tissue near the center of trabeculae,

suggesting that local tissue material properties influence the development of microdamage in cancellous bone. Finite element models can be used to examine how variations in tissue material properties affect the distribution of microdamage. Additionally, current research in cortical bone suggests that diffuse damage is repaired in a manner other than remodeling [158]. However, no one has examined how microdamage on trabeculae is repaired. In-vivo loading models can be used to explore the repair process of microdamage in cancellous bone.

## **6.2.1 *Continued Research Avenues***

### **6.2.1.1 *Material Properties Surrounding Cavities***

Based on the results from Chapter 2, resorption cavities should act as stress risers in cancellous bone; however, the results of Chapter 4 show that microdamage preferentially forms away from resorption cavities. One possible explanation is that resorption cavities preferentially form on regions of the trabeculae that are less susceptible to microdamage forming. Non-enzymatic glycation of bone results in advanced glycation endproducts that result in the tissue becoming more brittle [127]. Additionally, the presence of advanced glycation endproducts is negatively correlated with bone resorption [282] and has been shown to cause apoptosis in osteoclasts [281]. Therefore, if some regions of the trabecular surface have higher concentrations of advanced glycation endproducts they will be more susceptible to microdamage while being less likely to form resorption cavities. Furthermore, the interstitial regions of bone near the center of trabeculae have higher concentrations of advanced glycation

endproducts, are stiffer, and are less resistant to fracture [52, 53, 77] potentially explaining our observations regarding microdamage forming near the center of trabeculae. Another possible explanation is that during the remodeling process osteoclasts modify the local tissue material properties in a manner that decreases the likelihood of microdamage forming near resorption cavities. During remodeling, osteoclasts remove bone tissue by secreting factors that degrade the mineral and matrix of bone tissue [299-301], potentially decreasing the mineral content of tissue surrounding resorption cavities, making the tissue less likely to be damaged. The concentration of advanced glycation endproducts around cavities can be examined by looking at the auto fluorescence intensity [302]. Additionally, FTIR can be used to analyze the amount of collagen cross-linking and local mineral content [303] while nanoindentation can be used to examine the local indentation modulus and hardness [55, 304, 305].

#### ***6.2.1.2 Modeling Material Properties of Cancellous Bone***

In Chapter 4, the majority of microdamage was found to form near the center of trabeculae. Since bone remodeling occurs at the surface of trabeculae, younger bone tissue is found at the surface while older, stiffer, and less resistant to crack growth [52, 53, 77] tissue is located near the center. Therefore, tissue-level material properties appear to play a role in the development of microdamage. Finite element models of cancellous bone have shown that the distribution of stress and strain is affected by incorporating a heterogeneous tissue modulus [77, 87]. While in Chapter 5, finite

element models using homogenous tissue modulus were able to generally predict the location of microdamage, models using a heterogeneous tissue modulus could improve the predictive capability of the models. Finite element models can be created with heterogeneous tissue modulus by determining the material properties of each element based on x-ray attenuation values from micro-computed tomography images [297, 306, 307]. By performing a similar study to what was done in Chapter 5, the role that the tissue-level modulus in finite element models plays in predicting microdamage formation could be examined.

#### ***6.2.1.3 Microdamage Repair in Cancellous Bone***

In Chapter 4, the majority of microdamage was found to be located deeper than the maximum resorption cavity depth according to our results from Chapter 2. Therefore, either a large amount of microdamage is never repaired or a mechanism other than remodeling is removing damaged tissue near the center of trabecular struts. Since large amounts of microdamage accumulation would result in large reductions in biomechanical performance [78, 134], a mechanism other than remodeling removing microdamage from the center of trabeculae seems likely. In cortical bone, a process other than remodeling has been proposed to repair diffuse microdamage [158], however this has not been explored in cancellous bone. Currently, most studies that have examined microdamage in cancellous bone have been performed ex-vivo; however, an in-vivo loading model would be required to study how microdamage is repaired in cancellous bone. The rabbit femur loading is an in-vivo loading model

where a cyclic load is applied directly to the cancellous bone [308-312]. This model has been primarily used to examine how cancellous bone adapts to loading. In preliminary ex-vivo experiments, we were able to induce microdamage in cancellous bone (see *Appendix*). In addition to examining how microdamage is repaired in cancellous bone, an in-vivo model can be used to examine the effects of disease and drug treatment of microdamage development and repair.

## **6.2.2 *New Research Avenues***

### **6.2.2.1 *Spatial Relationship Between Microdamage and Structural Features***

While in Chapter 4 microdamage was found to be preferentially located away from resorption cavities, other microstructural features of cancellous bone may still influence microdamage development. Osteocyte lacunae have been shown to influence in the initiation and propagation of microdamage in murine cortical bone [313-315]. Furthermore, osteocyte lacunae may act as defects or stress risers in the bone tissue and therefore be preferential locations of microdamage initiation and propagation [316, 317]. Additionally in cortical bone, cement lines affect the development of microcracks. Transverse microcracks are arrested at cement lines while longitudinal microcracks travel along cement lines [131, 318, 319]. Therefore, examining the spatial relationship between osteocytes, cement lines, and microdamage may elucidate a role of cancellous microstructure in microdamage development. The spatial correlation techniques determined in chapters 3 and 4 could be used to examine if microdamage is preferentially located near osteocytes and cement lines. Serial milling

is capable of imaging both osteocyte lacunae and cement lines, although software still needs to be developed to automate these tasks. In chapter 4, microdamage was found to be preferentially located near the center of trabeculae. Since both osteocyte lacunae and cement lines in cancellous bone are located below the surface of trabeculae, one or both of these features may explain the location of microdamage development in cancellous bone. Furthermore, since both osteocytes and resorption cavities should act as stress concentrations, a positive spatial relationship between osteocyte lacunae and microdamage would further highlight effects of tissue material properties on microdamage development.

#### ***6.2.2.2 Modeling Variations in Cancellous Bone Tissue-Level Ductility***

While traditional engineering techniques harden the surface of materials to improve mechanical performance, cancellous bone appears to resist fracture by having a pliable surface with the majority of damage accumulating in the center of trabeculae. While comparing the toughness or ductility of the surface of trabeculae to the center of trabeculae cannot be done directly, modeling this behavior would give insight into how cancellous bone resists fracture. Nonlinear finite element models have been used to examine the effect of tissue-level ductility on apparent bone strength [102]. However, no one has examined the effects of spatial variations in tissue-level ductility. By creating finite element models with brittle elements at the center and ductile elements at the surface, the effects of tissue-level ductility can be examined. Understanding how cancellous bone resists fracture will is not only biologically

relevant but can also be used to inform the development of next generation foam materials.

## REFERENCES

- [1] Riggs BL, Melton LJ, 3rd. Involutional osteoporosis. *N Engl J Med* 1986;314: 1676-86.
- [2] Riggs BL, Melton LJ, 3rd. The worldwide problem of osteoporosis: insights afforded by epidemiology. *Bone* 1995;17: 505S-511S.
- [3] Burge R, Dawson-Hughes B, Solomon DH, Wong JB, King A, Tosteson A. Incidence and economic burden of osteoporosis-related fractures in the United States, 2005-2025. *Journal of Bone and Mineral Research* 2007;22: 465-475.
- [4] Braithwaite RS, Col NF, Wong JB. Estimating hip fracture morbidity, mortality and costs. *J Am Geriatr Soc* 2003;51: 364-70.
- [5] Hasserijs R, Karlsson MK, Jonsson B, Redlund-Johnell I, Johnell O. Long-term morbidity and mortality after a clinically diagnosed vertebral fracture in the elderly--a 12- and 22-year follow-up of 257 patients. *Calcif Tissue Int* 2005;76: 235-42.
- [6] Peris P. Stress fractures. *Best Pract Res Clin Rheumatol* 2003;17: 1043-61.
- [7] Patel DS, Roth M, Kapil N. Stress Fractures: Diagnosis, Treatment, and Prevention. *American Family Physician* 2011;83: 39-46.
- [8] Patel DR. Stress Fractures: Diagnosis and Management in the Primary Care Setting. *Pediatr Clin N Am* 2010;57: 819-827.
- [9] Snyder RA, Koester MC, Dunn WR. Epidemiology of stress fractures. *Clin Sports Med* 2006;25: 37-52, viii.
- [10] Anderson MW, Greenspan A. Stress fractures. *Radiology* 1996;199: 1-12.
- [11] Chen YT, Tenforde AS, Fredericson M. Update on stress fractures in female athletes: epidemiology, treatment, and prevention. *Curr Rev Musculoskelet Med* 2013;6: 173-81.

- [12] Fredericson M, Jennings F, Beaulieu C, Matheson GO. Stress fractures in athletes. *Top Magn Reson Imaging* 2006;17: 309-25.
- [13] Gilchrist J, Jones BH, Sleet DA, Kimsey CD. Exercise-related injuries among women: strategies for prevention from civilian and military studies. *MMWR Recomm Rep* 2000;49: 15-33.
- [14] Matheson GO, Clement DB, McKenzie DC, Taunton JE, Lloyd-Smith DR, MacIntyre JG. Stress fractures in athletes. A study of 320 cases. *Am J Sports Med* 1987;15: 46-58.
- [15] Pentecost RL, Murray RA, Brindley HH. Fatigue, Insufficiency, and Pathologic Fractures. *JAMA* 1964;187: 1001-4.
- [16] Daffner RH, Pavlov H. Stress fractures: current concepts. *AJR Am J Roentgenol* 1992;159: 245-52.
- [17] Cummings SR, Melton LJ. Epidemiology and outcomes of osteoporotic fractures. *Lancet* 2002;359: 1761-7.
- [18] Linstrom NJ, Heiserman JE, Kortman KE, Crawford NR, Baek S, Anderson RL, Pitt AM, Karis JP, Ross JS, Lekovic GP, Dean BL. Anatomical and biomechanical analyses of the unique and consistent locations of sacral insufficiency fractures. *Spine (Phila Pa 1976)* 2009;34: 309-15.
- [19] Cooper C, Atkinson EJ, O'Fallon WM, Melton LJ, 3rd. Incidence of clinically diagnosed vertebral fractures: a population-based study in Rochester, Minnesota, 1985-1989. *J Bone Miner Res* 1992;7: 221-7.
- [20] Cowin SC. *Bone mechanics handbook*. New York: Informa Healthcare; 2008.
- [21] Fratzl P, Gupta HS, Paschalis EP, Roschger P. Structure and mechanical quality of the collagen-mineral nano-composite in bone. *J Mater Chem* 2004;14: 2115-2123.
- [22] Clarke B. Normal bone anatomy and physiology. *Clin J Am Soc Nephrol* 2008;3 Suppl 3: S131-9.

- [23] Brodsky B, Persikov AV. Molecular structure of the collagen triple helix. *Adv Protein Chem* 2005;70: 301-39.
- [24] Rho JY, Kuhn-Spearing L, Zioupos P. Mechanical properties and the hierarchical structure of bone. *Med Eng Phys* 1998;20: 92-102.
- [25] Landis WJ. The strength of a calcified tissue depends in part on the molecular structure and organization of its constituent mineral crystals in their organic matrix. *Bone* 1995;16: 533-44.
- [26] Rho JY, Pharr GM. Effects of drying on the mechanical properties of bovine femur measured by nanoindentation. *J Mater Sci Mater Med* 1999;10: 485-8.
- [27] Currey JD. The effects of drying and re-wetting on some mechanical properties of cortical bone. *J Biomech* 1988;21: 439-41.
- [28] Evans FG, Lebow M. Regional Differences in Some of the Physical Properties of the Human Femur. *Journal of Applied Physiology* 1951;3: 563-572.
- [29] Dempster WT, Liddicoat RT. Compact bone as a non-isotropic material. *Am J Anat* 1952;91: 331-62.
- [30] Evans FG. Factors Affecting Mechanical Properties of Bone. *B New York Acad Med* 1973;49: 751-764.
- [31] Smith JW, Walmsley R. Factors affecting the elasticity of bone. *J Anat* 1959;93: 503-23.
- [32] Townsend PR, Rose RM, Radin EL. Buckling studies of single human trabeculae. *J Biomech* 1975;8: 199-201.
- [33] Currey JD. Anelasticity in Bone and Echinoderm Skeletons. *Journal of Experimental Biology* 1965;43: 279-&.
- [34] Parfitt AM. The two faces of growth: benefits and risks to bone integrity. *Osteoporos Int* 1994;4: 382-98.

- [35] Ruth EB. Bone studies. II. An experimental study of the Haversian-type vascular channels. *Am J Anat* 1953;93: 429-55.
- [36] Burr DB, Schaffler MB, Frederickson RG. Composition of the cement line and its possible mechanical role as a local interface in human compact bone. *J Biomech* 1988;21: 939-45.
- [37] Jaschouz D, Paris O, Roschger P, Hwang HS, Fratzl P. Pole figure analysis of mineral nanoparticle orientation in individual trabecula of human vertebral bone. *J Appl Crystallogr* 2003;36: 494-498.
- [38] Liu XS, Sajda P, Saha PK, Wehrli FW, Bevill G, Keaveny TM, Guo XE. Complete volumetric decomposition of individual trabecular plates and rods and its morphological correlations with anisotropic elastic moduli in human trabecular bone. *J Bone Miner Res* 2008;23: 223-35.
- [39] Dempster DW, Compston JE, Drezner MK, Glorieux FH, Kanis JA, Malluche H, Meunier PJ, Ott SM, Recker RR, Parfitt AM. Standardized nomenclature, symbols, and units for bone histomorphometry: a 2012 update of the report of the ASBMR Histomorphometry Nomenclature Committee. *J Bone Miner Res* 2013;28: 2-17.
- [40] Odgaard A. Three-dimensional methods for quantification of cancellous bone architecture. *Bone* 1997;20: 315-28.
- [41] Hildebrand T, Ruegsegger P. Quantification of Bone Microarchitecture with the Structure Model Index. *Comput Methods Biomech Biomed Engin* 1997;1: 15-23.
- [42] Parfitt AM. Osteonal and hemi-osteonal remodeling: the spatial and temporal framework for signal traffic in adult human bone. *Journal of cellular biochemistry* 1994;55: 273-86.
- [43] Hadjidakis DJ, Androulakis, II. Bone remodeling. *Ann N Y Acad Sci* 2006;1092: 385-96.
- [44] Ritchie RO, Koester KJ, Ionova S, Yao W, Lane NE, Ager JW, 3rd. Measurement of the toughness of bone: a tutorial with special reference to small animal studies. *Bone* 2008;43: 798-812.

- [45] Cole JH, van der Meulen MC. Whole bone mechanics and bone quality. *Clin Orthop Relat Res* 2011;469: 2139-49.
- [46] Turner CH, Burr DB. Basic biomechanical measurements of bone: a tutorial. *Bone* 1993;14: 595-608.
- [47] Zimmermann EA, Schaible E, Bale H, Barth HD, Tang SY, Reichert P, Busse B, Alliston T, Ager JW, 3rd, Ritchie RO. Age-related changes in the plasticity and toughness of human cortical bone at multiple length scales. *Proc Natl Acad Sci U S A* 2011;108: 14416-21.
- [48] Koester KJ, Barth HD, Ritchie RO. Effect of aging on the transverse toughness of human cortical bone: evaluation by R-curves. *J Mech Behav Biomed Mater* 2011;4: 1504-13.
- [49] Zimmermann EA, Launey ME, Ritchie RO. The significance of crack-resistance curves to the mixed-mode fracture toughness of human cortical bone. *Biomaterials* 2010;31: 5297-305.
- [50] Koester KJ, Ager JW, 3rd, Ritchie RO. The true toughness of human cortical bone measured with realistically short cracks. *Nat Mater* 2008;7: 672-7.
- [51] Yang QD, Cox BN, Nalla RK, Ritchie RO. Re-evaluating the toughness of human cortical bone. *Bone* 2006;38: 878-87.
- [52] Nalla RK, Kruzic JJ, Kinney JH, Ritchie RO. Effect of aging on the toughness of human cortical bone: evaluation by R-curves. *Bone* 2004;35: 1240-6.
- [53] Burket JC, Brooks DJ, MacLeay JM, Baker SP, Boskey AL, van der Meulen MC. Variations in nanomechanical properties and tissue composition within trabeculae from an ovine model of osteoporosis and treatment. *Bone* 2013;52: 326-36.
- [54] Burket J, Gourion-Arsiquaud S, Havill LM, Baker SP, Boskey AL, van der Meulen MC. Microstructure and nanomechanical properties in osteons relate to tissue and animal age. *J Biomech* 2011;44: 277-84.
- [55] Kim G, Cole JH, Boskey AL, Baker SP, van der Meulen MC. Reduced tissue-level stiffness and mineralization in osteoporotic cancellous bone. *Calcif Tissue Int*

2014;95: 125-31.

[56] Silva MJ, Brodt MD, Fan Z, Rho JY. Nanoindentation and whole-bone bending estimates of material properties in bones from the senescence accelerated mouse SAMP6. *J Biomech* 2004;37: 1639-46.

[57] Choi K, Kuhn JL, Ciarelli MJ, Goldstein SA. The elastic moduli of human subchondral, trabecular, and cortical bone tissue and the size-dependency of cortical bone modulus. *J Biomech* 1990;23: 1103-13.

[58] Currey JD. Effects of differences in mineralization on the mechanical properties of bone. *Philos Trans R Soc Lond B Biol Sci* 1984;304: 509-18.

[59] Reilly DT, Burstein AH, Frankel VH. The elastic modulus for bone. *J Biomech* 1974;7: 271-5.

[60] Zioupos P, Currey JD. Changes in the stiffness, strength, and toughness of human cortical bone with age. *Bone* 1998;22: 57-66.

[61] Reilly DT, Burstein AH. The elastic and ultimate properties of compact bone tissue. *J Biomech* 1975;8: 393-405.

[62] Pattin CA, Caler WE, Carter DR. Cyclic mechanical property degradation during fatigue loading of cortical bone. *J Biomech* 1996;29: 69-79.

[63] Zioupos P, Currey JD, Casinos A. Tensile fatigue in bone: are cycles-, or time to failure, or both, important? *J Theor Biol* 2001;210: 389-99.

[64] Nalla RK, Kinney JH, Ritchie RO. Mechanistic fracture criteria for the failure of human cortical bone. *Nat Mater* 2003;2: 164-8.

[65] Carter DR, Hayes WC. The compressive behavior of bone as a two-phase porous structure. *J Bone Joint Surg Am* 1977;59: 954-62.

[66] Lakes RS, Katz JL, Sternstein SS. Viscoelastic properties of wet cortical bone-I. Torsional and biaxial studies. *J Biomech* 1979;12: 657-78.

- [67] Park HC, Lakes RS. Cosserat micromechanics of human bone: strain redistribution by a hydration sensitive constituent. *J Biomech* 1986;19: 385-97.
- [68] Rho JY, Tsui TY, Pharr GM. Elastic properties of human cortical and trabecular lamellar bone measured by nanoindentation. *Biomaterials* 1997;18: 1325-30.
- [69] Turner CH, Cowin SC, Rho JY, Ashman RB, Rice JC. The fabric dependence of the orthotropic elastic constants of cancellous bone. *J Biomech* 1990;23: 549-61.
- [70] Goldstein SA, Goulet R, McCubbrey D. Measurement and significance of three-dimensional architecture to the mechanical integrity of trabecular bone. *Calcif Tissue Int* 1993;53 Suppl 1: S127-32; discussion S132-3.
- [71] Ding M, Odgaard A, Linde F, Hvid I. Age-related variations in the microstructure of human tibial cancellous bone. *J Orthop Res* 2002;20: 615-21.
- [72] Silva MJ, Gibson LJ. Modeling the mechanical behavior of vertebral trabecular bone: effects of age-related changes in microstructure. *Bone* 1997;21: 191-9.
- [73] Michel MC, Guo XD, Gibson LJ, McMahon TA, Hayes WC. Compressive fatigue behavior of bovine trabecular bone. *J Biomech* 1993;26: 453-63.
- [74] Bowman SM, Guo XE, Cheng DW, Keaveny TM, Gibson LJ, Hayes WC, McMahon TA. Creep contributes to the fatigue behavior of bovine trabecular bone. *J Biomech Eng* 1998;120: 647-54.
- [75] Haddock SM, Yeh OC, Mummaneni PV, Rosenberg WS, Keaveny TM. Similarity in the fatigue behavior of trabecular bone across site and species. *J Biomech* 2004;37: 181-7.
- [76] Moore TL, Gibson LJ. Fatigue of bovine trabecular bone. *J Biomech Eng* 2003;125: 761-8.
- [77] Mulder L, Koolstra JH, den Toonder JM, van Eijden TM. Intratrabecular distribution of tissue stiffness and mineralization in developing trabecular bone. *Bone* 2007;41: 256-65.

- [78] Lambers FM, Bouman AR, Rinnac CM, Hernandez CJ. Microdamage caused by fatigue loading in human cancellous bone: relationship to reductions in bone biomechanical performance. *PLoS One* 2013;8: e83662.
- [79] Keaveny TM, Wachtel EF, Ford CM, Hayes WC. Differences between the tensile and compressive strengths of bovine tibial trabecular bone depend on modulus. *J Biomech* 1994;27: 1137-46.
- [80] Keaveny TM, Guo XE, Wachtel EF, McMahon TA, Hayes WC. Trabecular bone exhibits fully linear elastic behavior and yields at low strains. *J Biomech* 1994;27: 1127-36.
- [81] Taddei F, Schileo E, Helgason B, Cristofolini L, Viceconti M. The material mapping strategy influences the accuracy of CT-based finite element models of bones: an evaluation against experimental measurements. *Med Eng Phys* 2007;29: 973-9.
- [82] Currey J. Measurement of the mechanical properties of bone: a recent history. *Clin Orthop Relat Res* 2009;467: 1948-54.
- [83] Yeni YN, Wu B, Huang L, Oravec D. Mechanical loading causes detectable changes in morphometric measures of trabecular structure in human cancellous bone. *J Biomech Eng* 2013;135: 54505.
- [84] Niebur GL, Yuen JC, Hsia AC, Keaveny TM. Convergence behavior of high-resolution finite element models of trabecular bone. *J Biomech Eng* 1999;121: 629-35.
- [85] Guldberg RE, Hollister SJ, Charras GT. The accuracy of digital image-based finite element models. *J Biomech Eng* 1998;120: 289-95.
- [86] Harrigan TP, Jasty M, Mann RW, Harris WH. Limitations of the continuum assumption in cancellous bone. *J Biomech* 1988;21: 269-75.
- [87] Renders GA, Mulder L, van Ruijven LJ, Langenbach GE, van Eijden TM. Mineral heterogeneity affects predictions of intratrabecular stress and strain. *J Biomech* 2011;44: 402-7.
- [88] Mulder L, van Ruijven LJ, Koolstra JH, van Eijden TM. The influence of mineralization on intratrabecular stress and strain distribution in developing trabecular

bone. *Ann Biomed Eng* 2007;35: 1668-77.

[89] Carretta R, Lorenzetti S, Muller R. Towards patient-specific material modeling of trabecular bone post-yield behavior. *Int J Numer Method Biomed Eng* 2013;29: 250-72.

[90] Niebur GL, Feldstein MJ, Yuen JC, Chen TJ, Keaveny TM. High-resolution finite element models with tissue strength asymmetry accurately predict failure of trabecular bone. *J Biomech* 2000;33: 1575-83.

[91] Morgan EF, Keaveny TM. Dependence of yield strain of human trabecular bone on anatomic site. *J Biomech* 2001;34: 569-77.

[92] Morgan EF, Yeh OC, Chang WC, Keaveny TM. Nonlinear behavior of trabecular bone at small strains. *J Biomech Eng* 2001;123: 1-9.

[93] Niebur GL, Feldstein MJ, Keaveny TM. Biaxial failure behavior of bovine tibial trabecular bone. *J Biomech Eng* 2002;124: 699-705.

[94] Bayraktar HH, Gupta A, Kwon RY, Papadopoulos P, Keaveny TM. The modified super-ellipsoid yield criterion for human trabecular bone. *J Biomech Eng* 2004;126: 677-84.

[95] Morgan EF, Bayraktar HH, Yeh OC, Majumdar S, Burghardt A, Keaveny TM. Contribution of inter-site variations in architecture to trabecular bone apparent yield strains. *J Biomech* 2004;37: 1413-20.

[96] Bevill G, Eswaran SK, Gupta A, Papadopoulos P, Keaveny TM. Influence of bone volume fraction and architecture on computed large-deformation failure mechanisms in human trabecular bone. *Bone* 2006;39: 1218-25.

[97] Nawathe S, Yang H, Fields AJ, Boussein ML, Keaveny TM. Theoretical effects of fully ductile versus fully brittle behaviors of bone tissue on the strength of the human proximal femur and vertebral body. *J Biomech* 2015;48: 1264-9.

[98] Bayraktar HH, Keaveny TM. Mechanisms of uniformity of yield strains for trabecular bone. *Journal of biomechanics* 2004;37: 1671-1678.

- [99] Bayraktar HH, Morgan EF, Niebur GL, Morris GE, Wong EK, Keaveny TM. Comparison of the elastic and yield properties of human femoral trabecular and cortical bone tissue. *J Biomech* 2004;37: 27-35.
- [100] Bevill G, Keaveny TM. Trabecular bone strength predictions using finite element analysis of micro-scale images at limited spatial resolution. *Bone* 2009;44: 579-584.
- [101] Morgan EF, Bayraktar HH, Yeh OC, Majumdar S, Burghardt A, Keaveny TM. Contribution of inter-site variations in architecture to trabecular bone apparent yield strains. *Journal of biomechanics* 2004;37: 1413-1420.
- [102] Nawathe S, Juillard F, Keaveny TM. Theoretical bounds for the influence of tissue-level ductility on the apparent-level strength of human trabecular bone. *J Biomech* 2013;46: 1293-9.
- [103] Bourne BC, van der Meulen MC. Finite element models predict cancellous apparent modulus when tissue modulus is scaled from specimen CT-attenuation. *J Biomech* 2004;37: 613-21.
- [104] Vanrietbergen B, Weinans H, Huiskes R, Odgaard A. A New Method to Determine Trabecular Bone Elastic Properties and Loading Using Micromechanical Finite-Element Models. *J Biomech* 1995;28: 69-&.
- [105] Mischinski S, Ural A. Interaction of microstructure and microcrack growth in cortical bone: a finite element study. *Comput Methods Biomech Biomed Engin* 2013;16: 81-94.
- [106] Ural A, Vashishth D. Cohesive finite element modeling of age-related toughness loss in human cortical bone. *Journal of biomechanics* 2006;39: 2974-2982.
- [107] Ural A, Zioupos P, Buchanan D, Vashishth D. The effect of strain rate on fracture toughness of human cortical bone: A finite element study. *J Mech Behav Biomed* 2011;4: 1021-1032.
- [108] Nagaraja S, Couse TL, Guldborg RE. Trabecular bone microdamage and microstructural stresses under uniaxial compression. *J Biomech* 2005;38: 707-16.

[109] Nagaraja S, Skrinjar O, Guldberg RE. Spatial correlations of trabecular bone microdamage with local stresses and strains using rigid image registration. *J Biomech Eng* 2011;133: 064502.

[110] Shi X, Liu XS, Wang X, Guo XE, Niebur GL. Effects of trabecular type and orientation on microdamage susceptibility in trabecular bone. *Bone* 2010;46: 1260-6.

[111] Guo XE, McMahon TA, Keaveny TM, Hayes WC, Gibson LJ. Finite element modeling of damage accumulation in trabecular bone under cyclic loading. *J Biomech* 1994;27: 145-55.

[112] Ural A, Bruno P, Zhou B, Shi XT, Guo XE. A new fracture assessment approach coupling HR-pQCT imaging and fracture mechanics-based finite element modeling. *J Biomech* 2013;46: 1305-11.

[113] Keaveny TM. Biomechanical computed tomography-noninvasive bone strength analysis using clinical computed tomography scans. *Ann Ny Acad Sci* 2010;1192: 57-65.

[114] Kettner M, Ramsthaler F, Potente S, Bockenheimer A, Schmidt PH, Schrodtt M. Blunt force impact to the head using a teeball bat: systematic comparison of physical and finite element modeling. *Forensic Sci Med Pat* 2014;10: 513-517.

[115] Muir P, Johnson KA, Ruaux-Mason CP. In vivo matrix microdamage in a naturally occurring canine fatigue fracture. *Bone* 1999;25: 571-6.

[116] Diab T, Vashishth D. Morphology, localization and accumulation of in vivo microdamage in human cortical bone. *Bone* 2007;40: 612-8.

[117] Burr DB, Forwood MR, Fyhrie DP, Martin RB, Schaffler MB, Turner CH. Bone microdamage and skeletal fragility in osteoporotic and stress fractures. *J Bone Miner Res* 1997;12: 6-15.

[118] Follet H, Viguet-Carrin S, Burt-Pichat B, Depalle B, Bala Y, Gineyts E, Munoz F, Arlot M, Boivin G, Chapurlat RD, Delmas PD, Bouxsein ML. Effects of preexisting microdamage, collagen cross-links, degree of mineralization, age, and architecture on compressive mechanical properties of elderly human vertebral trabecular bone. *J Orthop Res* 2011;29: 481-8.

- [119] Wenzel TE, Schaffler MB, Fyhrie DP. In vivo trabecular microcracks in human vertebral bone. *Bone* 1996;19: 89-95.
- [120] Vashishth D, Koontz J, Qiu SJ, Lundin-Cannon D, Yeni YN, Schaffler MB, Fyhrie DP. In vivo diffuse damage in human vertebral trabecular bone. *Bone* 2000;26: 147-52.
- [121] Burr DB. Why bones bend but don't break. *J Musculoskelet Neuronal Interact* 2011;11: 270-85.
- [122] Burr DB, Stafford T. Validity of the bulk-staining technique to separate artifactual from in vivo bone microdamage. *Clin Orthop Relat Res* 1990: 305-8.
- [123] Seref-Ferlengez Z, Kennedy OD, Schaffler MB. Bone microdamage, remodeling and bone fragility: how much damage is too much damage? *Bonekey Rep* 2015;4: 644.
- [124] Boyce TM, Fyhrie DP, Glotkowski MC, Radin EL, Schaffler MB. Damage type and strain mode associations in human compact bone bending fatigue. *J Orthop Res* 1998;16: 322-9.
- [125] Parsamian GP, Norman TL. Diffuse damage accumulation in the fracture process zone of human cortical bone specimens and its influence on fracture toughness. *J Mater Sci Mater Med* 2001;12: 779-83.
- [126] Vashishth D, Tanner KE, Bonfield W. Contribution, development and morphology of microcracking in cortical bone during crack propagation. *J Biomech* 2000;33: 1169-74.
- [127] Tang SY, Vashishth D. Non-enzymatic glycation alters microdamage formation in human cancellous bone. *Bone* 2010;46: 148-54.
- [128] Karim L, Vashishth D. Role of Trabecular Microarchitecture in the Formation, Accumulation, and Morphology of Microdamage in Human Cancellous Bone. *Journal of Orthopaedic Research* 2011;29: 1739-1744.
- [129] Chapurlat RD, Delmas PD. Bone microdamage: a clinical perspective. *Osteoporos Int* 2009;20: 1299-308.

- [130] Burr DB, Turner CH, Naick P, Forwood MR, Ambrosius W, Hasan MS, Pidaparti R. Does microdamage accumulation affect the mechanical properties of bone? *J Biomech* 1998;31: 337-45.
- [131] Schaffler MB, Radin EL, Burr DB. Mechanical and morphological effects of strain rate on fatigue of compact bone. *Bone* 1989;10: 207-14.
- [132] Keaveny TM, Wachtel EF, Guo XE, Hayes WC. Mechanical behavior of damaged trabecular bone. *J Biomech* 1994;27: 1309-18.
- [133] Jepsen KJ, Davy DT. Comparison of damage accumulation measures in human cortical bone. *J Biomech* 1997;30: 891-4.
- [134] Hernandez CJ, Lambers FM, Widjaja J, Chapa C, Rinnac CM. Quantitative relationships between microdamage and cancellous bone strength and stiffness. *Bone* 2014;66: 205-13.
- [135] Carter DR, Hayes WC. Compact bone fatigue damage: a microscopic examination. *CLINICAL ORTHOPAEDICS AND RELATED RESEARCH* 1977: 265-74.
- [136] O'Brien FJ, Taylor D, Clive Lee T. The effect of bone microstructure on the initiation and growth of microcracks. *J Orthop Res* 2005;23: 475-80.
- [137] Saha S. Longitudinal Shear Properties of Human Compact Bone and Its Constituents, and Associated Failure Mechanisms. *J Mater Sci* 1977;12: 1798-1806.
- [138] Nalla RK, Kruzic JJ, Kinney JH, Balooch M, Ager JW, Ritchie RO. Role of microstructure in the aging-related deterioration of the toughness of human cortical bone. *Mat Sci Eng C-Bio S* 2006;26: 1251-1260.
- [139] Norman TL, Wang Z. Microdamage of human cortical bone: incidence and morphology in long bones. *Bone* 1997;20: 375-9.
- [140] Akkus O, Jepsen KJ, Rinnac CM. Microstructural aspects of the fracture process in human cortical bone. *J Mater Sci* 2000;35: 6065-6074.

- [141] Ritchie RO. Mechanisms of fatigue-crack propagation in ductile and brittle solids. *Int J Fracture* 1999;100: 55-83.
- [142] Launey ME, Buehler MJ, Ritchie RO. On the Mechanistic Origins of Toughness in Bone. *Annu Rev Mater Res* 2010;40: 25-53.
- [143] Vashishth D, Tanner KE, Bonfield W. Contribution, development and morphology of microcracking in cortical bone during crack propagation. *J Biomech* 2000;33: 1169-1174.
- [144] Vashishth D, Behiri JC, Bonfield W. Crack growth resistance in cortical bone: Concept of microcrack toughening. *J Biomech* 1997;30: 763-769.
- [145] Nalla RK, Kruzic JJ, Ritchie RO. On the origin of the toughness of mineralized tissue: microcracking or crack bridging? *Bone* 2004;34: 790-798.
- [146] Nalla RK, Kinney JH, Ritchie RO. Effect of orientation on the in vitro fracture toughness of dentin: the role of toughening mechanisms. *Biomaterials* 2003;24: 3955-3968.
- [147] Burr DB, Martin RB, Schaffler MB, Radin EL. Bone Remodeling in Response to In vivo Fatigue Microdamage. *J Biomech* 1985;18: 189-&.
- [148] Martin RB. Toward a unifying theory of bone remodeling. *Bone* 2000;26: 1-6.
- [149] Schaffler MB. Role of bone turnover in microdamage. *Osteoporos Int* 2003;14 Suppl 5: S73-7; discussion S77-80.
- [150] Mori S, Burr DB. Increased intracortical remodeling following fatigue damage. *Bone* 1993;14: 103-9.
- [151] Burr DB, Martin RB, Schaffler MB, Radin EL. Bone remodeling in response to in vivo fatigue microdamage. *J Biomech* 1985;18: 189-200.
- [152] Bentolila V, Boyce TM, Fyhrie DP, Drumb R, Skerry TM, Schaffler MB. Intracortical remodeling in adult rat long bones after fatigue loading. *Bone* 1998;23: 275-81.

[153] Mashiba T, Hirano T, Turner CH, Forwood MR, Johnston CC, Burr DB. Suppressed bone turnover by bisphosphonates increases microdamage accumulation and reduces some biomechanical properties in dog rib. *J Bone Miner Res* 2000;15: 613-20.

[154] Allen MR, Iwata K, Phipps R, Burr DB. Alterations in canine vertebral bone turnover, microdamage accumulation, and biomechanical properties following 1-year treatment with clinical treatment doses of risedronate or alendronate. *Bone* 2006;39: 872-9.

[155] Verborgt O, Gibson GJ, Schaffler MB. Loss of osteocyte integrity in association with microdamage and bone remodeling after fatigue in vivo. *J Bone Miner Res* 2000;15: 60-7.

[156] Verborgt O, Tatton NA, Majeska RJ, Schaffler MB. Spatial distribution of Bax and Bcl-2 in osteocytes after bone fatigue: complementary roles in bone remodeling regulation? *J Bone Miner Res* 2002;17: 907-14.

[157] Herman BC, Cardoso L, Majeska RJ, Jepsen KJ, Schaffler MB. Activation of bone remodeling after fatigue: differential response to linear microcracks and diffuse damage. *Bone* 2010;47: 766-72.

[158] Seref-Ferlengez Z, Basta-Pljakic J, Kennedy OD, Philemon CJ, Schaffler MB. Structural and mechanical repair of diffuse damage in cortical bone in vivo. *J Bone Miner Res* 2014;29: 2537-44.

[159] Eriksen EF. Normal and pathological remodeling of human trabecular bone: three dimensional reconstruction of the remodeling sequence in normals and in metabolic bone disease. *Endocr Rev* 1986;7: 379-408.

[160] Mosekilde L. The effect of modelling and remodelling on human vertebral body architecture. *Technol Health Care* 1998;6: 287-97.

[161] Gourion-Arsiquaud S, Burket JC, Havill LM, DiCarlo E, Doty SB, Mendelsohn R, van der Meulen MC, Boskey AL. Spatial variation in osteonal bone properties relative to tissue and animal age. *J Bone Miner Res* 2009;24: 1271-81.

[162] Hernandez CJ. How can bone turnover modify bone strength independent of bone mass? *Bone* 2008;42: 1014-20.

- [163] McNamara LM, Prendergast PJ. Perforation of cancellous bone trabeculae by damage-stimulated remodelling at resorption pits: a computational analysis. *Eur J Morphol* 2005;42: 99-109.
- [164] McNamara LM, Van der Linden JC, Weinans H, Prendergast PJ. Stress-concentrating effect of resorption lacunae in trabecular bone. *J Biomech* 2006;39: 734-41.
- [165] Manolagas SC, Jilka RL. Bone marrow, cytokines, and bone remodeling. Emerging insights into the pathophysiology of osteoporosis. *N Engl J Med* 1995;332: 305-11.
- [166] Sambrook P, Cooper C. Osteoporosis. *Lancet* 2006;367: 2010-8.
- [167] Manolagas SC. Birth and death of bone cells: basic regulatory mechanisms and implications for the pathogenesis and treatment of osteoporosis. *Endocr Rev* 2000;21: 115-37.
- [168] Parfitt AM, Mathews CH, Villanueva AR, Kleerekoper M, Frame B, Rao DS. Relationships between surface, volume, and thickness of iliac trabecular bone in aging and in osteoporosis. Implications for the microanatomic and cellular mechanisms of bone loss. *J Clin Invest* 1983;72: 1396-409.
- [169] Parfitt AM. Age-related structural changes in trabecular and cortical bone: cellular mechanisms and biomechanical consequences. *Calcif Tissue Int* 1984;36 Suppl 1: S123-8.
- [170] Garnero P. Markers of bone turnover for the prediction of fracture risk. *Osteoporos. Int.* 2000;11 Suppl 6: S55-65.
- [171] Gerdhem P, Ivaska KK, Alatalo SL, Halleen JM, Hellman J, Isaksson A, Pettersson K, Vaananen HK, Akesson K, Obrant KJ. Biochemical markers of bone metabolism and prediction of fracture in elderly women. *J. Bone Miner. Res.* 2004;19: 386-93.
- [172] Garnero P. Biomarkers for osteoporosis management : utility in diagnosis, fracture risk prediction and therapy monitoring. *Mol Diagn Ther* 2008;12: 157-70.

- [173] Johnell O, Oden A, De Laet C, Garnero P, Delmas PD, Kanis JA. Biochemical indices of bone turnover and the assessment of fracture probability. *Osteoporos. Int.* 2002;13: 523-6.
- [174] Smit TH, Burger EH. Is BMU-coupling a strain-regulated phenomenon? A finite element analysis. *J Bone Miner Res* 2000;15: 301-7.
- [175] Easley SK, Chang MT, Shindich D, Hernandez CJ, Keaveny TM. Biomechanical effects of simulated resorption cavities in cancellous bone across a wide range of bone volume fractions. *J Bone Miner Res* 2012;27: 1927-35.
- [176] Poundarik AA, Vashishth D. Multiscale imaging of bone microdamage. *Connect Tissue Res* 2015;56: 87-98.
- [177] Bouxsein ML, Boyd SK, Christiansen BA, Guldberg RE, Jepsen KJ, Muller R. Guidelines for assessment of bone microstructure in rodents using micro-computed tomography. *J Bone Miner Res* 2010;25: 1468-86.
- [178] Bigley RF, Singh M, Hernandez CJ, Kazakia GJ, Martin RB, Keaveny TM. Validity of serial milling-based imaging system for microdamage quantification. *Bone* 2008;42: 212-5.
- [179] Zioupos P, Currey JD. The Extent of Microcracking and the Morphology of Microcracks in Damaged Bone. *J Mater Sci* 1994;29: 978-986.
- [180] Frost HM, Villanueva AR, Roth H, Stanisavljevic S. Tetracycline bone labeling. *J New Drugs* 1961;1: 206-16.
- [181] Frost HM. Tetracycline-based histological analysis of bone remodeling. *Calcif Tissue Res* 1969;3: 211-37.
- [182] O'Brien FJ, Taylor D, Lee TC. An improved labelling technique for monitoring microcrack growth in compact bone. *J Biomech* 2002;35: 523-6.
- [183] Lambers FM, Bouman AR, Tkachenko EV, Keaveny TM, Hernandez CJ. The Effects of tensile-compressive loading mode and microarchitecture on microdamage in Human vertebral cancellous bone. *J Biomech* 2014.

[184] Leng HJ, Wang X, Ross RD, Niebur GL, Roeder RK. Micro-computed tomography of fatigue microdamage in cortical bone using a barium sulfate contrast agent. *J Mech Behav Biomed* 2008;1: 68-75.

[185] Li J, Miller MA, Hutchins GD, Burr DB. Imaging bone microdamage in vivo with positron emission tomography. *Bone* 2005;37: 819-24.

[186] Lee TC, Arthur TL, Gibson LJ, Hayes WC. Sequential labelling of microdamage in bone using chelating agents. *J Orthop Res* 2000;18: 322-5.

[187] Zarrinkalam KH, Kuliwaba JS, Martin RB, Wallwork MA, Fazzalari NL. New insights into the propagation of fatigue damage in cortical bone using confocal microscopy and chelating fluorochromes. *Eur J Morphol* 2005;42: 81-90.

[188] Goff MG, Slyfield CR, Kummari SR, Tkachenko EV, Fischer SE, Yi YH, Jekir MG, Keaveny TM, Hernandez CJ. Three-dimensional characterization of resorption cavity size and location in human vertebral trabecular bone. *Bone* 2012;51: 28-37.

[189] Eriksen EF, Melsen F, Mosekilde L. Reconstruction of the resorptive site in iliac trabecular bone: a kinetic model for bone resorption in 20 normal individuals. *Metab Bone Dis Relat Res* 1984;5: 235-42.

[190] Griffith JF, Genant HK. New advances in imaging osteoporosis and its complications. *Endocrine* 2012;42: 39-51.

[191] Link TM. Osteoporosis imaging: state of the art and advanced imaging. *Radiology* 2012;263: 3-17.

[192] Bevill G, Keaveny TM. Trabecular bone strength predictions using finite element analysis of micro-scale images at limited spatial resolution. *Bone* 2009;44: 579-84.

[193] Bayraktar HH, Keaveny TM. Mechanisms of uniformity of yield strains for trabecular bone. *J Biomech* 2004;37: 1671-8.

[194] van Oers RF, van Rietbergen B, Ito K, Huiskes R, Hilbers PA. Simulations of trabecular remodeling and fatigue: is remodeling helpful or harmful? *Bone* 2011;48:

1210-5.

[195] Slyfield CR, Jr., Niemeyer KE, Tkachenko EV, Tomlinson RE, Steyer GG, Patthanacharoenphon CG, Kazakia GJ, Wilson DL, Hernandez CJ. Three-dimensional surface texture visualization of bone tissue through epifluorescence-based serial block face imaging. *J Microsc* 2009;236: 52-9.

[196] Tkachenko EV, Slyfield CR, Tomlinson RE, Daggett JR, Wilson DL, Hernandez CJ. Voxel size and measures of individual resorption cavities in three-dimensional images of cancellous bone. *Bone* 2009;45: 487-92.

[197] Daims H, Wagner M. In Situ Techniques and Digital Image Analysis Methods for Quantifying Spatial Localization Patterns of Nitrifiers and Other Microorganisms in Biofilm and Flocs. *Method Enzymol* 2011;496: 185-215.

[198] Reed MG, Howard CV. Stereological estimation of covariance using linear dipole probes. *J Microsc-Oxford* 1999;195: 96-103.

[199] Reed MG, Howard CV, De Yanes GS. One-Stop Stereology: the estimation of 3D parameters using Isotropic Rulers. *Journal of Microscopy* 2010;239: 54-65.

[200] Morgan EF, Salisbury Palomares KT, Gleason RE, Bellin DL, Chien KB, Unnikrishnan GU, Leong PL. Correlations between local strains and tissue phenotypes in an experimental model of skeletal healing. *J Biomech* 2010;43: 2418-24.

[201] Terrier A, Rakotomanana RL, Ramaniraka AN, Leyvraz PF. Adaptation Models of Anisotropic Bone. *Comput Methods Biomech Biomed Engin* 1997;1: 47-59.

[202] Goff MG, Chang KL, Litts EN, Hernandez CJ. The effects of misalignment during in vivo loading of bone: Techniques to detect the proximity of objects in three-dimensional models. *J Biomech* 2014;47: 3156-3161.

[203] Qiu S, Rao DS, Palnitkar S, Parfitt AM. Age and distance from the surface but not menopause reduce osteocyte density in human cancellous bone. *Bone* 2002;31: 313-8.

[204] Goff MG, Lambers FM, Nguyen TM, Sung J, Rimnac CM, Hernandez CJ.

Fatigue-induced microdamage in cancellous bone occurs distant from resorption cavities and trabecular surfaces. *Bone* 2015;79: 8-14.

[205] Wang X, Sanyal A, Cawthon PM, Palermo L, Jekir M, Christensen J, Ensrud KE, Cummings SR, Orwoll E, Black DM, Keaveny TM. Prediction of new clinical vertebral fractures in elderly men using finite element analysis of CT scans. *J Bone Miner Res* 2012;27: 808-16.

[206] Herblum R, Beek M, Whyne CM. muFEA successfully exhibits higher stresses and strains in microdamaged regions of whole vertebrae. *J Orthop Res* 2013;31: 1653-60.

[207] Garnero P, Hausherr E, Chapuy MC, Marcelli C, Grandjean H, Muller C, Cormier C, Breart G, Meunier PJ, Delmas PD. Markers of bone resorption predict hip fracture in elderly women: the EPIDOS Prospective Study. *J Bone Miner Res* 1996;11: 1531-8.

[208] Dempster DW. The contribution of trabecular architecture to cancellous bone quality. *J Bone Miner Res* 2000;15: 20-3.

[209] Parfitt AM. High bone turnover is intrinsically harmful: two paths to a similar conclusion. The Parfitt view. *J Bone Miner Res* 2002;17: 1558-9.

[210] Kragstrup J, Gundersen HJ, Melsen F, Mosekilde L. Estimation of the three-dimensional wall thickness of completed remodeling sites in iliac trabecular bone. *Metab Bone Dis Relat Res* 1982;4: 113-9.

[211] Parfitt AM, Drezner MK, Glorieux FH, Kanis JA, Malluche H, Meunier PJ, Ott SM, Recker RR. Bone histomorphometry: standardization of nomenclature, symbols, and units. Report of the ASBMR Histomorphometry Nomenclature Committee. *J Bone Miner Res* 1987;2: 595-610.

[212] Eriksen EF, Hodgson SF, Eastell R, Cedel SL, O'Fallon WM, Riggs BL. Cancellous bone remodeling in type I (postmenopausal) osteoporosis: quantitative assessment of rates of formation, resorption, and bone loss at tissue and cellular levels. *Journal of Bone and Mineral Research* 1990;5: 311-9.

[213] Garrahan NJ, Croucher PI, Compston JE. A computerised technique for the quantitative assessment of resorption cavities in trabecular bone. *Bone* 1990;11: 241-

5.

[214] Cohen-Solal ME, Shih MS, Lundy MW, Parfitt AM. A new method for measuring cancellous bone erosion depth: application to the cellular mechanisms of bone loss in postmenopausal osteoporosis [see comments]. *Journal of Bone and Mineral Research* 1991;6: 1331-1338.

[215] Recker RR, Kimmel DB, Dempster D, Weinstein RS, Wronski TJ, Burr DB. Issues in modern bone histomorphometry. *Bone* 2011;49: 955-64.

[216] Dempster DW, Shane E, Horbert W, Lindsay R. A simple method for correlative light and scanning electron microscopy of human iliac crest bone biopsies: qualitative observations in normal and osteoporotic subjects. *J Bone Miner Res* 1986;1: 15-21.

[217] Mosekilde L. Consequences of the remodelling process for vertebral trabecular bone structure: a scanning electron microscopy study (uncoupling of unloaded structures). *Bone Miner* 1990;10: 13-35.

[218] Gentsch C, Junge M, Puschel K, Delling G, Kaiser E. A scanning electron microscopy-based approach to quantify resorption lacunae applied to the trabecular bone of the femoral head. *J Bone Miner Metab* 2005;23: 205-11.

[219] Boyde A, Dillon CE, Jones SJ. Measurement of osteoclastic resorption pits with a tandem scanning microscope. *J Microsc* 1990;158 ( Pt 2): 261-5.

[220] Boyde A, Jones SJ. Pitfalls in pit measurement. *Calcif Tissue Int* 1991;49: 65-70.

[221] Parfitt AM. The physiologic and clinical significance of bone histomorphometric data. In: Recker RR, editor. *Bone histomorphometry: techniques and interpretation*. Boca Raton, FL: CRC Press; 1983, p. 143-223.

[222] Liu XS, Bevill G, Keaveny TM, Sajda P, Guo XE. Micromechanical analyses of vertebral trabecular bone based on individual trabeculae segmentation of plates and rods. *J Biomech* 2009;42: 249-56.

[223] Kummari SR, Coan TA, Hernandez CJ. Stress concentration factors of

Remodeling Cavities on Rod-like and Plate-like Trabeculae. In: Trans. Orthopaedic Research Society. Long Beach, CA, USA; 2011. p. 2200.

[224] Bigley RF, Singh M, Hernandez CJ, Kazakia GJ, Martin RB, Keaveny TM. Validity of serial milling-based imaging system for microdamage quantification. *Bone* 2008;42: 212-215.

[225] Kazakia GJ, Lee JJ, Singh M, Bigley RF, Martin RB, Keaveny TM. Automated high-resolution three-dimensional fluorescence imaging of large biological specimens. *J Microsc* 2007;225: 109-17.

[226] Tkachenko EV, Slyfield CR, Tomlinson RE, Daggett JR, Wilson DL, Hernandez CJ. Voxel size and measures of individual resorption cavities in three-dimensional images of cancellous bone. *Bone* 2009;45: 487-492.

[227] Carr JC, Fright WR, Beatson RK. Surface interpolation with radial basis functions for medical imaging. *IEEE Trans Med Imaging* 1997;16: 96-107.

[228] Buckley MJ. Fast Computation of a Discretized Thin-Plate Smoothing Spline for Image Data. *Biometrika* 1994;81: 247-258.

[229] Slyfield CR, Tkachenko EV, Wilson DL, Hernandez CJ. Three-dimensional dynamic bone histomorphometry. *J Bone Miner Res* 2011.

[230] Doube M, Klosowski MM, Arganda-Carreras I, Cordelieres FP, Dougherty RP, Jackson JS, Schmid B, Hutchinson JR, Shefelbine SJ. BoneJ Free and extensible bone image analysis in ImageJ. *Bone* 2010;47: 1076-1079.

[231] Liu XS, Sajda P, Saha PK, Wehrli FW, Bevill G, Keaveny TM, Guo XE. Complete volumetric decomposition of individual trabecular plates and rods and its morphological correlations with anisotropic elastic moduli in human trabecular bone. *J Bone Miner Res* 2008;23: 223-35.

[232] Compston JE, Croucher PI. Histomorphometric assessment of trabecular bone remodelling in osteoporosis. *Bone Miner* 1991;14: 91-102.

[233] Parfitt AM. Osteonal and Hemi-Osteonal Remodeling - the Spatial and Temporal Framework for Signal Traffic in Adult Human Bone. *J Cell Biochem*

1994;55: 273-286.

[234] Vesterby A, Kragstrup J, Gundersen HJ, Melsen F. Unbiased stereologic estimation of surface density in bone using vertical sections. *Bone* 1987;8: 13-7.

[235] Croucher PI, Garrahan NJ, Mellish RW, Compston JE. Age-related changes in resorption cavity characteristics in human trabecular bone. *Osteoporos Int* 1991;1: 257-61.

[236] Hauge EM, Mosekilde L, Melsen F. Stereological considerations concerning the measurement of individual osteoid seams and resorption cavities. *Bone Miner* 1994;26: 89-90.

[237] Gentsch C, Delling G, Kaiser E. Microstructural classification of resorption lacunae and perforations in human proximal femora. *Calcif Tissue Int* 2003;72: 698-709.

[238] Gentsch C, Pueschel K, Deuretzbacher G, Delling G, Kaiser E. First inventory of resorption lacunae on rods and plates of trabecular bone as observed by scanning electron microscopy. *Calcif Tissue Int* 2005;76: 154-62.

[239] Parfitt AM, Mundy GR, Roodman GD, Hughes DE, Boyce BF. A new model for the regulation of bone resorption, with particular reference to the effects of bisphosphonates. *J Bone Miner Res* 1996;11: 150-9.

[240] Riggs BL, Parfitt AM. Drugs used to treat osteoporosis: the critical need for a uniform nomenclature based on their action on bone remodeling. *J Bone Miner Res* 2005;20: 177-84.

[241] Parfitt AM. Skeletal heterogeneity and the purposes of bone remodeling. In: Marcus R, Feldman D, Nelson DA, Rosen CJ, editors. *Osteoporosis*. 3rd Edition ed. San Diego, CA, USA: Elsevier Academic Press; 2008, p. 71-92.

[242] Leung P, Pickarski M, Zhuo Y, Masarachia PJ, Duong LT. The effects of the cathepsin K inhibitor odanacatib on osteoclastic bone resorption and vesicular trafficking. *Bone* 2011;49: 623-35.

[243] Soe K, Delaisse JM. Glucocorticoids Maintain Human Osteoclasts in the

Active Mode of Their Resorption Cycle. *Journal of Bone and Mineral Research* 2010;25: 2184-2192.

[244] Jinnai H, Watashiba H, Kajihara T, Nishikawa Y, Takahashi M, Ito M. Surface curvatures of trabecular bone microarchitecture. *Bone* 2002;30: 191-194.

[245] Huiskes R, Ruimerman R, van Lenthe GH, Janssen JD. Effects of mechanical forces on maintenance and adaptation of form in trabecular bone. *Nature* 2000;405: 704-6.

[246] Turner CH. Toward a mathematical description of bone biology: the principle of cellular accommodation. *Calcified Tissue Int* 1999;65: 466-71.

[247] van der Meulen MC HC. Adaptation of Skeletal Structure to Mechanical Loading. In: Marcus R FD, Dempster D, Cauley J, Luckey M, editor. *Osteoporosis*. San Diego, CA, USA: Academic Press; 2013.

[248] Schulte FA, Ruffoni D, Lambers FM, Christen D, Webster DJ, Kuhn G, Muller R. Local mechanical stimuli regulate bone formation and resorption in mice at the tissue level. *PLoS One* 2013;8: e62172.

[249] Schulte FA, Zwahlen A, Lambers FM, Kuhn G, Ruffoni D, Betts D, Webster DJ, Muller R. Strain-adaptive in silico modeling of bone adaptation--a computer simulation validated by in vivo micro-computed tomography data. *Bone* 2013;52: 485-92.

[250] Lambers FM, Schulte FA, Kuhn G, Webster DJ, Muller R. Mouse tail vertebrae adapt to cyclic mechanical loading by increasing bone formation rate and decreasing bone resorption rate as shown by time-lapsed in vivo imaging of dynamic bone morphometry. *Bone* 2011;49: 1340-50.

[251] Lambers FM, Koch K, Kuhn G, Ruffoni D, Weigt C, Schulte FA, Muller R. Trabecular bone adapts to long-term cyclic loading by increasing stiffness and normalization of dynamic morphometric rates. *Bone* 2013;55: 325-34.

[252] Guo XE, Eichler MJ, Takai E, Kim CH. Quantification of a rat tail vertebra model for trabecular bone adaptation studies. *J Biomech* 2002;35: 363-8.

[253] Kim CH, Takai E, Zhou H, von Stechow D, Muller R, Dempster DW, Guo XE. Trabecular bone response to mechanical and parathyroid hormone stimulation: the role of mechanical microenvironment. *Journal of Bone and Mineral Research* 2003;18: 2116-25.

[254] Webster DJ, Morley PL, van Lenthe GH, Muller R. A novel in vivo mouse model for mechanically stimulated bone adaptation--a combined experimental and computational validation study. *Computer Methods in Biomechanics and Biomedical Engineering* 2008;11: 435-41.

[255] Chambers TJ, Evans M, Gardner TN, Turner-Smith A, Chow JW. Induction of bone formation in rat tail vertebrae by mechanical loading. *Bone Miner* 1993;20: 167-78.

[256] Otsu N. Threshold Selection Method from Gray-Level Histograms. *Ieee T Syst Man Cyb* 1979;9: 62-66.

[257] Lynch ME, Main RP, Xu Q, Walsh DJ, Schaffler MB, Wright TM, van der Meulen MC. Cancellous bone adaptation to tibial compression is not sex dependent in growing mice. *Journal of Applied Physiology* 2010;109: 685-91.

[258] Elliott DM, Sarver JJ. Young investigator award winner: validation of the mouse and rat disc as mechanical models of the human lumbar disc. *Spine* 2004;29: 713-22.

[259] Webster D, Wirth A, van Lenthe GH, Muller R. Experimental and finite element analysis of the mouse caudal vertebrae loading model: prediction of cortical and trabecular bone adaptation. *Biomech Model Mechanobiol* 2012;11: 221-30.

[260] Kim CH, Takai E, Culella N, Guo XE. Measurements of In Vivo Strains in the Rat Tail Vertebra. *ASME Conference Proceedings* 2002;2002: 303-304.

[261] Daims H, Wagner M. In situ techniques and digital image analysis methods for quantifying spatial localization patterns of nitrifiers and other microorganisms in biofilm and flocs. *Methods in Enzymology* 2011;496: 185-215.

[262] Reed MG, Howard CV. Stereological estimation of covariance using linear dipole probes. *Journal of Microscopy* 1999;195: 96-103.

[263] Reed MG, Howard CV, GS DEY. One-stop stereology: the estimation of 3D parameters using isotropic rulers. *J Microsc* 2010;239: 54-65.

[264] Shane E, Burr D, Abrahamsen B, Adler RA, Brown TD, Cheung AM, Cosman F, Curtis JR, Dell R, Dempster DW, Ebeling PR, Einhorn TA, Genant HK, Geusens P, Klaushofer K, Lane JM, McKiernan F, McKinney R, Ng A, Nieves J, O'Keefe R, Papapoulos S, Howe TS, van der Meulen MC, Weinstein RS, Whyte MP. Atypical subtrochanteric and diaphyseal femoral fractures: second report of a task force of the American Society for Bone and Mineral Research. *J Bone Miner Res* 2014;29: 1-23.

[265] de Waard EA, van Geel TA, Savelberg HH, Koster A, Geusens PP, van den Bergh JP. Increased fracture risk in patients with type 2 diabetes mellitus: An overview of the underlying mechanisms and the usefulness of imaging modalities and fracture risk assessment tools. *Maturitas* 2014.

[266] Birkenhager-Frenkel DH, Nigg AL, Hens CJ, Birkenhager JC. Changes of interstitial bone thickness with age in men and women. *Bone* 1993;14: 211-6.

[267] Arthur Moore TL, Gibson LJ. Microdamage accumulation in bovine trabecular bone in uniaxial compression. *J Biomech Eng* 2002;124: 63-71.

[268] Fyhrie DP, Schaffler MB. Failure mechanisms in human vertebral cancellous bone. *Bone* 1994;15: 105-9.

[269] Nagaraja S, Skrinjar O, Guldborg RE. Spatial correlations of trabecular bone microdamage with local stresses and strains using rigid image registration. *J Biomech Eng* 2011;133: 064502.

[270] Moore TL, Gibson LJ. Fatigue microdamage in bovine trabecular bone. *J Biomech Eng* 2003;125: 769-76.

[271] Green JO, Wang J, Diab T, Vidakovic B, Guldborg RE. Age-related differences in the morphology of microdamage propagation in trabecular bone. *J Biomech* 2011;44: 2659-66.

[272] Mouton PR. *Unbiased Stereology: A Concise Guide*: Johns Hopkins University Press; 2013.

[273] Tang SY, Vashishth D. A non-invasive in vitro technique for the three-dimensional quantification of microdamage in trabecular bone. *Bone* 2007;40: 1259-64.

[274] Karim L, Vashishth D. Role of trabecular microarchitecture in the formation, accumulation, and morphology of microdamage in human cancellous bone. *J Orthop Res* 2011;29: 1739-44.

[275] Keaveny TM, Pinilla TP, Crawford RP, Kopperdahl DL, Lou A. Systematic and random errors in compression testing of trabecular bone. *J Orthop Res* 1997;15: 101-10.

[276] Bonfield W. Advances in the fracture mechanics of cortical bone. *J Biomech* 1987;20: 1071-81.

[277] Hernandez CJ, Gupta A, Keaveny TM. A biomechanical analysis of the effects of resorption cavities on cancellous bone strength. *J Bone Miner Res* 2006;21: 1248-55.

[278] Lambers FM, Bouman AR, Tkachenko EV, Keaveny TM, Hernandez CJ. The effects of tensile-compressive loading mode and microarchitecture on microdamage in human vertebral cancellous bone. *J Biomech* 2014;47: 3605-3612.

[279] Goff MG, Chang KL, Litts EN, Hernandez CJ. The effects of misalignment during in vivo loading of bone: Techniques to detect the proximity of objects in three-dimensional models. *J Biomech* 2014.

[280] Launey ME, Buehler MJ, Ritchie RO. On the Mechanistic Origins of Toughness in Bone. *Annual Review of Materials Research* 2010;40: 25-53.

[281] Valcourt U, Merle B, Gineyts E, Viguet-Carrin S, Delmas PD, Garnero P. Non-enzymatic glycation of bone collagen modifies osteoclastic activity and differentiation. *J Biol Chem* 2007;282: 5691-703.

[282] Ural A, Janeiro C, Karim L, Diab T, Vashishth D. Association between non-enzymatic glycation, resorption, and microdamage in human tibial cortices. *Osteoporos Int* 2014.

- [283] Ehlert K, O'Brien R, Hernandez C. Statistical power in measures of microscopic tissue damage in cancellous bone. American Society for Bone and Mineral Research. San Diego, CA, USA. pp. MO0052 2011.
- [284] Brock GR, Kim G, Ingraffea AR, Andrews JC, Pianetta P, van der Meulen MC. Nanoscale examination of microdamage in sheep cortical bone using synchrotron radiation transmission x-ray microscopy. PLoS One 2013;8: e57942.
- [285] Niebur GL, Yuen JC, Burghardt AJ, Keaveny TM. Sensitivity of damage predictions to tissue level yield properties and apparent loading conditions. J Biomech 2001;34: 699-706.
- [286] Baumann AP, Shi X, Roeder RK, Niebur GL. The sensitivity of nonlinear computational models of trabecular bone to tissue level constitutive model. Comput Methods Biomech Biomed Engin 2015: 1-9.
- [287] Yeni YN, Hou FJ, Ciarelli T, Vashishth D, Fyhrie DP. Trabecular shear stresses predict in vivo linear microcrack density but not diffuse damage in human vertebral cancellous bone. Ann Biomed Eng 2003;31: 726-32.
- [288] Wang X, Guyette J, Liu X, Roeder RK, Niebur GL. Axial-shear interaction effects on microdamage in bovine tibial trabecular bone. Eur J Morphol 2005;42: 61-70.
- [289] Wu Z, Laneve AJ, Niebur GL. In vivo microdamage is an indicator of susceptibility to initiation and propagation of microdamage in human femoral trabecular bone. Bone 2013;55: 208-15.
- [290] Bevill G, Eswaran SK, Farahmand F, Keaveny TM. The influence of boundary conditions and loading mode on high-resolution finite element-computed trabecular tissue properties. Bone 2009;44: 573-8.
- [291] Slyfield CR, Tkachenko EV, Wilson DL, Hernandez CJ. Three-dimensional dynamic bone histomorphometry. J Bone Miner Res 2012;27: 486-95.
- [292] Adams MF, Bayraktar HH, Keaveny TM, Papadopoulos P. Ultrascaleable Implicit Finite Element Analyses in Solid Mechanics with over a Half a Billion Degrees of Freedom. In: Proceedings of the 2004 ACM/IEEE Conference: IEEE Computer Society; 2004. p. 34.

- [293] Goff MG, Lambers FM, Nguyen TM, Sung J, Rimnac CM, Hernandez CJ. Fatigue-induced microdamage in cancellous bone occurs distant from resorption cavities and trabecular surfaces. *Bone* 2015.
- [294] Sun X, Hoon Jeon J, Blendell J, Akkus O. Visualization of a phantom post-yield deformation process in cortical bone. *J Biomech* 2010;43: 1989-96.
- [295] Mullender MG, Huiskes R, Versleyen H, Buma P. Osteocyte density and histomorphometric parameters in cancellous bone of the proximal femur in five mammalian species. *J Orthop Res* 1996;14: 972-9.
- [296] Currey JD. The structure and mechanics of bone. *J Mater Sci* 2012;47: 41-54.
- [297] Mulder L, Koolstra JH, den Toonder JM, van Eijden TM. Relationship between tissue stiffness and degree of mineralization of developing trabecular bone. *J Biomed Mater Res A* 2008;84: 508-15.
- [298] Bevill G, Farhamand F, Keaveny TM. Heterogeneity of yield strain in low-density versus high-density human trabecular bone. *J Biomech* 2009;42: 2165-70.
- [299] Drake FH, Dodds RA, James IE, Connor JR, Debouck C, Richardson S, Lee-Rykaczewski E, Coleman L, Rieman D, Barthlow R, Hastings G, Gowen M. Cathepsin K, but not cathepsins B, L, or S, is abundantly expressed in human osteoclasts. *J Biol Chem* 1996;271: 12511-6.
- [300] Bossard MJ, Tomaszek TA, Thompson SK, Amegadzie BY, Hanning CR, Jones C, Kurdyla JT, McNulty DE, Drake FH, Gowen M, Levy MA. Proteolytic activity of human osteoclast cathepsin K. Expression, purification, activation, and substrate identification. *J Biol Chem* 1996;271: 12517-24.
- [301] Suda T, Takahashi N, Martin TJ. Modulation of osteoclast differentiation. *Endocr Rev* 1992;13: 66-80.
- [302] Dong XN, Qin A, Xu J, Wang X. In situ accumulation of advanced glycation endproducts (AGEs) in bone matrix and its correlation with osteoclastic bone resorption. *Bone* 2011;49: 174-83.
- [303] Figueiredo M, Martins A, Gamelas J. Characterization of bone and bone-based

graft materials using FTIR spectroscopy: INTECH Open Access Publisher; 2012.

[304] Brennan O, Kennedy OD, Lee TC, Rackard SM, O'Brien FJ. Biomechanical properties across trabeculae from the proximal femur of normal and ovariectomised sheep. *J Biomech* 2009;42: 498-503.

[305] Donnelly E, Baker SP, Boskey AL, van der Meulen MC. Effects of surface roughness and maximum load on the mechanical properties of cancellous bone measured by nanoindentation. *J Biomed Mater Res A* 2006;77: 426-35.

[306] Currey JD. What determines the bending strength of compact bone? *J Exp Biol* 1999;202: 2495-503.

[307] Mulder L, Koolstra JH, Van Eijden TM. Accuracy of microCT in the quantitative determination of the degree and distribution of mineralization in developing bone. *Acta Radiol* 2004;45: 769-77.

[308] Morgan TG, Bostrom MP, van der Meulen MC. Tissue-level remodeling simulations of cancellous bone capture effects of in vivo loading in a rabbit model. *J Biomech* 2015;48: 875-82.

[309] Grosso MJ, Courtland HW, Yang X, Sutherland JP, Stoner K, Nguyen J, Fahlgren A, Ross FP, van der Meulen MC, Bostrom MP. Intermittent PTH administration and mechanical loading are anabolic for periprosthetic cancellous bone. *J Orthop Res* 2015;33: 163-73.

[310] Fahlgren A, Yang X, Ciani C, Ryan JA, Kelly N, Ko FC, van der Meulen MC, Bostrom MP. The effects of PTH, loading and surgical insult on cancellous bone at the bone-implant interface in the rabbit. *Bone* 2013;52: 718-24.

[311] van der Meulen MC, Yang X, Morgan TG, Bostrom MP. The effects of loading on cancellous bone in the rabbit. *Clin Orthop Relat Res* 2009;467: 2000-6.

[312] Yang X, Willie BM, Beach JM, Wright TM, van der Meulen MC, Bostrom MP. Trabecular bone adaptation to loading in a rabbit model is not magnitude-dependent. *J Orthop Res* 2013;31: 930-4.

[313] Voide R, Schneider P, Stauber M, Wyss P, Stampanoni M, Sennhauser U, van

Lenthe GH, Muller R. Time-lapsed assessment of microcrack initiation and propagation in murine cortical bone at submicrometer resolution. *Bone* 2009;45: 164-73.

[314] Voide R, Schneider P, Stauber M, van Lenthe GH, Stampanoni M, Muller R. The importance of murine cortical bone microstructure for microcrack initiation and propagation. *Bone* 2011;49: 1186-93.

[315] Schneider P, Voide R, Stampanoni M, Donahue LR, Muller R. The importance of the intracortical canal network for murine bone mechanics. *Bone* 2013;53: 120-8.

[316] Nicoletta DP, Moravits DE, Gale AM, Bonewald LF, Lankford J. Osteocyte lacunae tissue strain in cortical bone. *J Biomech* 2006;39: 1735-43.

[317] Bonivitch AR, Bonewald LF, Nicoletta DP. Tissue strain amplification at the osteocyte lacuna: a microstructural finite element analysis. *J Biomech* 2007;40: 2199-206.

[318] Ritchie RO, Buehler MJ, Hansma P. Plasticity and toughness in bone. *Phys Today* 2009;62: 41-47.

[319] Schaffler MB, Choi K, Milgrom C. Aging and matrix microdamage accumulation in human compact bone. *Bone* 1995;17: 521-25.

## **APPENDIX A: CHAPTER 3 SUPPLEMENTARY MATERIAL**

### **Inflate Algorithm SOP**

#### **Purpose**

The purpose of this SOP is to explain how to use the software in the Volume Based Spatial Correlation Code to calculate the spatial correlation using the “inflate” algorithm. Reference the following paper for more information on the technique (Daims and Wagner 2011). The paper should be saved with this SOP.

#### **Methods**

1. Collect and organize all the images that you want to use as your type A object images in a folder with a recognizable name. (The images must be in tif or tiff format. The images should preferably be logical or saved as 0's and 1's.)
  - a. In the Ref Data example, this folder is the Type\_A\_image\_directory
2. Collect and organize all the images that you want to use as your type B object images in a folder with a recognizable name. (The images must be in tif or tiff format. The images should preferably be logical or saved as 0's and 1's.)
  - a. In the Ref Data example, this folder is the Type\_B\_image\_directory
3. Collect and organize all the images that you want to use as your random type B material images in a folder with a recognizable name. (The images must be in tif or tiff format. The images should preferably be logical or saved as 0's and 1's. Should be created using the Randomly distributed image creator. See Randomly\_distributed\_image\_creator\_SOP.)

- a. In the Ref Data example, this folder is the  
Random\_type\_B\_Volume\_image\_directory
4. Create a folder to hold the output Matlab variable
  - a. In the Ref Data, this folder is the Matlab\_variable\_output
5. Create a folder to hold the random code that is created during usage of this program
  - a. In the Ref Data, this folder is the Random\_code\_storage\_directory
6. Create a folder to hold the subfolders created for dilation during usage of this program
  - a. In the Ref Data, this folder is the Inflate\_folder\_directory
7. Put all the folders in a main folder with a recognizable name.
8. Decide on the name for your Matlab output variable (DO NOT PUT any .mat etc in the name)
  - a. In the Ref Data, this is called Inflate\_results\_9\_15\_2014
9. Decide on the radii you want to search with this method (These values should be in  $\mu\text{m}$ 's and should preferably be multiples of your image voxel size. Do not input units.)
  - a. In the Ref Data, the values used were 1.5, 3, 6, 15, 30, and 60  $\mu\text{m}$   
(Folders are listed as rounded to the nearest non-decimal number).
10. Determine the voxel size of your images (Your type A, type B, and random type B images should all be the same voxel size and should be isotropic voxels (i.e. cubic voxels). You should list this in  $\mu\text{m}$  but without including the units.)
  - a. In the Ref Data, the voxel size is 1.5  $\mu\text{m}$

11. Unzip the Volume\_based\_Spatial\_Correlation\_software.rar
  - a. Make sure both Volume\_based\_spatial\_correlation and Amira\_grown\_surface are in the same folder
12. Open the Volume\_based\_spatial\_correlation in Matlab
  - a. Run this program by opening it and pressing either the Run button or F5
    - i. You will possibly be prompted: “To run this file, you can either change the MATLAB current folder or add its folder to the MATLAB path”
      1. Choose “Change Folder”
13. Follow the prompts from the program
  - a. Choose the folders and input the information that is requested
14. Unless you have significant experience with Matlab do not attempt to change code or use debug mode known as matt\_mode

### **Inflate Algorithm Software**

```
function Volume_based_spatial_correlation(Code_storage_directory,
Type_A_img_directory,Type_B_img_directory,
Rand_type_B_img_directory,... Matlab_save_directory,Inflate_main_folders,save_variable,...
radii_to_examine,vox_size)
% Purpose: The purpose of this code is to perform the inflate algorithm
% and calculate the volume based spatial correlation metric

% Last Edited on 2_25_2015 by MGG this version takes into consideration all different types
of situations where the images are not quite the same size

% Additional functions to have in the same directory as this function:
% Amira_grown_surface.m

% Inputs if nargin
if nargin==0
```

```

Main_directory = uigetdir('Pick the folder to act as the main folder for the rest of the
folders');
Type_A_img_directory = uigetdir([Main_directory,'\'],'Pick the folder that contains the type
A images (these are the ones that will be inflated)');
Type_B_img_directory = uigetdir([Main_directory,'\'],'Pick the folder that contains the type
B images (these are the ones that will be searched for)');
Rand_type_B_img_directory = uigetdir([Main_directory,'\'],...
'Pick the folder that contains the random type B images (these are the ones created with
the Randomly distributed image creator)');

Name_code_folder = input('What do you want to call the folder that will contain
incidentally created codes?');
Code_storage_directory = [Main_directory,'\Name_code_folder];

Name_save_folder = input('What do you want to call the folder containing the output
matlab variable?');
Matlab_save_directory = [Main_directory,'\Name_save_folder];

Name_inflate_main_folder = input('What do you want to call the folder that will contain all
the sub-folders used in the inflate program?');
Inflate_main_folders = [Main_directory,'\Name_inflate_main_folder];

save_variable=input('What do you want call the output matlab variable (do not include
.mat)?');

display('Input all radii and voxel sizes in um but do not include units only type numbers');
x=1;
radii_to_examine=[];
while x~=0
    x=input('Input the radii you want to inspect one at a time pressing enter after each one
and input 0 to finish (no units): ');
    if x~=0
        radii_to_examine=[radii_to_examine;x];
    end
end
vox_size=input('What is the voxel size for these images? (only type number no units)');

end

% Set up directories based on input
Type_A_img_directory=[Type_A_img_directory,'\'];
Type_B_img_directory=[Type_B_img_directory,'\'];
Rand_type_B_img_directory=[Rand_type_B_img_directory,'\'];

% Set up new directories
Code_storage_directory=[Code_storage_directory,'\'];
Matlab_save_directory=[Matlab_save_directory,'\'];
Inflate_main_folders=[Inflate_main_folders,'\'];

% Make sure directories exist

```

```

if ~exist(Code_storage_directory,'dir')
    mkdir(Code_storage_directory);
end
if ~exist(Matlab_save_directory,'dir')
    mkdir(Matlab_save_directory);
end
if ~exist(Inflate_main_folders,'dir')
    mkdir(Inflate_main_folders);
end

% Set up the number of voxels to search based off voxel size and radii
num_of_vox_to_search=round(radii_to_examine/vox_size);

% Setup current image names
type_B_imgs=dir([Type_B_img_directory,'*tif*']);
rand_type_B_imgs=dir([Rand_type_B_img_directory,'*tif*']);

% Setup inflate grown directories
Inflate_folder_names=cell(size(num_of_vox_to_search,1),1);
To_inflate_or_already_inflated_images=ones(size(num_of_vox_to_search,1),1);

back_slash_pos=strfind(Type_A_img_directory,'\');
Grow_img_directory=[Type_A_img_directory(back_slash_pos(end-1):back_slash_pos(end)-
1),'_dilated_images'];

for i=1:size(num_of_vox_to_search,1)

Inflate_folder_names{i}=[Inflate_main_folders,Grow_img_directory,'_grown_',num2str(round
d(radii_to_examine(i))),'_um\'];
    if ~exist(Inflate_folder_names{i},'dir')
        mkdir(Inflate_folder_names{i});
    else
        cur_imgs=dir([Inflate_folder_names{i},'*tif*']);
        if size(cur_imgs,1)<size(type_B_imgs,1)
            To_inflate_or_already_inflated_images(i)=1;
        else
            To_inflate_or_already_inflated_images(i)=0;
        end
    end
end

% Grow directories that need to be grown
for i=1:size(radii_to_examine,1)
    if To_inflate_or_already_inflated_images(i)==1
        % Grow Seed Images

Amira_grown_surface(Code_storage_directory,Type_A_img_directory,Inflate_folder_names{
i},num_of_vox_to_search(i));
    end
end

```

```

% Set up volume storage arrays
type_B_volume=zeros(size(num_of_vox_to_search,1),1);
rand_type_B_volume=zeros(size(num_of_vox_to_search,1),1);

type_B_near_type_A_volume=zeros(size(num_of_vox_to_search,1),1);
rand_type_B_near_type_A_volume=zeros(size(num_of_vox_to_search,1),1);

% Setup the ratio metric for inflate
perc_type_B_near_type_A=zeros(size(num_of_vox_to_search,1),1);
perc_rand_type_B_near_type_A=zeros(size(num_of_vox_to_search,1),1);
metric_output=zeros(size(num_of_vox_to_search,1),1);

% Set up dilated image names
dilated_imgs=dir([Inflate_folder_names{1},'*tif*']);

% Examine overlap of dilated type A images and type B/rand type B images
display(['Analyzing for savevar : ',save_variable]);
for radius=1:size(radii_to_examine,1)
    for image_slice=1:size(dilated_imgs,1)

        % Read in dilated image on current slice
        dilated_img=imread([Inflate_folder_names{radius},dilated_imgs(image_slice).name]);

        % Read in type B images but ensure they are the same size as type A
        % images (Padding may occur in some processing steps from Amira)

type_B_img=imread([Type_B_img_directory,type_B_imgs(image_slice+((size(type_B_imgs,
1)-size(dilated_imgs,1))/2)).name]);

        % Read in rand type B images but ensure they are the same size as type A
        % images (Padding may occur in some processing steps from Amira)

rand_type_B_img=imread([Rand_type_B_img_directory,rand_type_B_imgs(image_slice+(siz
e(rand_type_B_imgs,1)-size(dilated_imgs,1))/2).name]);

        if size(type_B_img,1)>=size(dilated_img,1)

            % Resize type B and rand type B images if necessary
            type_B_padding_x=(size(type_B_img,1)-size(dilated_img,1))/2;
            type_B_padding_y=(size(type_B_img,2)-size(dilated_img,2))/2;
            type_B_img=type_B_img(1+ceil(type_B_padding_x):end-((2*type_B_padding_x)-
ceil(type_B_padding_x)),...
                1+ceil(type_B_padding_y):end-((2*type_B_padding_y)-ceil(type_B_padding_y)));

            rand_type_B_padding_x=(size(rand_type_B_img,1)-size(dilated_img,1))/2;
            rand_type_B_padding_y=(size(rand_type_B_img,2)-size(dilated_img,2))/2;
            rand_type_B_img=rand_type_B_img(1+ceil(rand_type_B_padding_x):end-
((2*rand_type_B_padding_x)-ceil(rand_type_B_padding_x)),...

```

```

        1+ceil(rand_type_B_padding_y):end-((2*rand_type_B_padding_y)-
ceil(rand_type_B_padding_y)));
    else
        dilated_padding_x=(size(dilated_img,1)-size(type_B_img,1))/2;
        dilated_padding_y=(size(dilated_img,2)-size(type_B_img,2))/2;
        dilated_img=dilated_img(1+ceil(dilated_padding_x):end-((2*dilated_padding_x)-
ceil(dilated_padding_x)),...
        1+ceil(dilated_padding_y):end-((2*dilated_padding_y)-ceil(dilated_padding_y)));
    end

    % Calculate the volume in type B and rand type B images
    type_B_volume(radius)=type_B_volume(radius)+sum(sum(type_B_img>0));

rand_type_B_volume(radius)=rand_type_B_volume(radius)+sum(sum(rand_type_B_img>0));

    % Calculate the volume in the overlap between dilated type A and type B and rand type
B images

type_B_near_type_A_volume(radius)=type_B_near_type_A_volume(radius)+sum(sum((logic
al(type_B_img).*logical(dilated_img)>0)));

rand_type_B_near_type_A_volume(radius)=rand_type_B_near_type_A_volume(radius)+sum
(sum((rand_type_B_img.*dilated_img)>0));
    end

    % Calculate the ratio metric for the volume based method

perc_type_B_near_type_A(radius)=type_B_near_type_A_volume(radius)/type_B_volume(rad
ius);

perc_rand_type_B_near_type_A(radius)=rand_type_B_near_type_A_volume(radius)/rand_ty
pe_B_volume(radius);

metric_output(radius)=perc_type_B_near_type_A(radius)/perc_rand_type_B_near_type_A(ra
dius);

    % Display outputs from this method
    display(['Here are the results for the current sample at a dilated radius of
',num2str(round(rad_ii_to_examine(radius))),' um']);
    display(['The percentage of type B material near type A material is
',num2str(perc_type_B_near_type_A(radius))]);
    display(['The percentage of rand type B material near type B material is
',num2str(perc_rand_type_B_near_type_A(radius))]);
    display(['The volume based spatial correlation ratio metric is:
',num2str(metric_output(radius))]);
end

save([Matlab_save_directory,save_variable],'type_B_volume','rand_type_B_volume','type_B_
near_type_A_volume',...

```

```
'rand_type_B_near_type_A_volume','perc_type_B_near_type_A','perc_rand_type_B_near_type_A','metric_output','-v7.3');  
end
```

## Object Based Spatial Correlation Algorithm SOP

### Purpose

The purpose of this SOP is to explain how to use the software in the Object Number Based Spatial Correlation Code to calculate percentage of type B objects near type A objects. This method is qualitative rather than quantitative. For a more quantitative method, look at the Volume Based Spatial Correlation SOP.

### Methods

1. 1. Collect and organize all the images that you want to use as your type A object images in a folder with a recognizable name. (The images must be in tif or tiff format. The images should preferably be logical or saved as 0's and 1's.)
  - a. In the Ref Data example, this folder is the Type\_A\_image\_directory
2. Collect and organize all the images that you want to use as your type B object images in a folder with a recognizable name. (The images must be in png or tif or tiff format. The images should be of labeled objects and every object in the image stack should have a unique object number other than 0. The background should be 0.)
  - a. In the Ref Data example, this folder is the Type\_B\_image\_directory
3. Create a folder to hold the output Matlab variable
  - a. In the Ref Data, this folder is the Matlab\_variable\_output
4. Create a folder to hold the random code that is created during usage of this program
  - a. In the Ref Data, this folder is the Random\_code\_storage\_directory

5. Create a folder to hold the subfolders created for dilation during usage of this program
  - a. In the Ref Data, this folder is the Inflate\_folder\_directory
6. Put all the folders in a main folder with a recognizable name.
7. Decide on the name for your Matlab output variable (DO NOT PUT any .mat etc in the name)
  - a. In the Ref Data, this is called Object\_based\_results\_9\_16\_2014
8. Decide on the radii you want to search with this method (These values should be in  $\mu\text{m}$ 's and should preferably be multiples of your image voxel size. Do not input units.)
  - a. In the Ref Data, the values used were 1.5, 3, 6, 15, 30, 60, and 150  $\mu\text{m}$   
(Folders are listed as rounded to the nearest non-decimal number).
9. Determine the voxel size of your images (Your type A and type B should all be the same voxel size and should be isotropic voxels (i.e. cubic voxels). You should list this in  $\mu\text{m}$  but without including the units.)
  - a. In the Ref Data, the voxel size is 1.5  $\mu\text{m}$
10. Unzip the Object\_number\_based\_spatial\_correlation.rar
  - a. Make sure both Object\_number\_based\_spatial\_correlation and Amira\_grown\_surface are in the same folder
11. Open the Object\_number\_based\_spatial\_correlation in Matlab
  - a. Run this program by opening it and pressing either the Run button or F5

i. You will possibly be prompted: “To run this file, you can either change the MATLAB current folder or add its folder to the MATLAB path”

1. Choose “Change Folder”

12. Follow the prompts from the program

a. Choose the folders and input the information that is requested

13. Unless you have significant experience with Matlab do not attempt to change code or use debug mode known as `matt_mode`

### **Object Based Spatial Correlation Algorithm Software**

```
Function Object_number_based_spatial_correlation(  
Code_storage_directory,Type_A_img_directory,Type_B_img_directory,...  
Matlab_save_directory,Inflate_main_folders,save_variable,... radii_to_examine,vox_size)
```

```
% Purpose: The purpose of this code is to calculate the qualitative measure  
% of the number of type B objects near type A objects
```

```
% Last Edited on 9_16_2015 by MGG
```

```
% Additional functions to have in the same directory as this function:  
% Amira_grown_surface.m
```

```
% Inputs if nargin  
if nargin==0
```

```
    Main_directory = uigetdir('Pick the folder to act as the main folder for the rest of the  
folders');
```

```
    Type_A_img_directory = uigetdir([Main_directory,'\'],'Pick the folder that contains the type  
A images (these are the ones that will be inflated)');
```

```
    Type_B_img_directory = uigetdir([Main_directory,'\'],'Pick the folder that contains the type  
B images (these are the ones that will be searched for)');
```

```
    Name_code_folder = input('What do you want to call the folder that will contain  
incidentally created codes?');
```

```
    Code_storage_directory = [Main_directory,'\Name_code_folder];
```

```
    Name_save_folder = input('What do you want to call the folder containing the output  
matlab variable?');
```

```

Matlab_save_directory = [Main_directory,'\Name_save_folder];

Name_inflate_main_folder = input('What do you want to call the folder that will contain all
the sub-folders used in the inflate program?');
Inflate_main_folders = [Main_directory,'\Name_inflate_main_folder];

save_variable=input('What do you want call the output matlab variable (do not include
.mat)?');

display('Input all radii and voxel sizes in um but do not include units only type numbers');
x=1;
radii_to_examine=[];
while x~=0
    x=input('Input the radii you want to inspect one at a time pressing enter after each one
and input 0 to finish (no units): ');
    if x~=0
        radii_to_examine=[radii_to_examine;x];
    end
end
vox_size=input('What is the voxel size for these images? (only type number no units));

end

% Set up directories based on input
Type_A_img_directory=[Type_A_img_directory,'\];
Type_B_img_directory=[Type_B_img_directory,'\];

% Set up new directories
Code_storage_directory=[Code_storage_directory,'\];
Matlab_save_directory=[Matlab_save_directory,'\];
Inflate_main_folders=[Inflate_main_folders,'\];

% Make sure directories exist
if ~exist(Code_storage_directory,'dir')
    mkdir(Code_storage_directory);
end
if ~exist(Matlab_save_directory,'dir')
    mkdir(Matlab_save_directory);
end
if ~exist(Inflate_main_folders,'dir')
    mkdir(Inflate_main_folders);
end

% Set up the number of voxels to search based off voxel size and radii
num_of_vox_to_search=round(radii_to_examine/vox_size);

% Setup type A image names
type_A_imgs=dir([Type_A_img_directory,'*tif*']);

% Set up type B image names (may be png or tif or tiff)

```

```

type_B_imgs=dir([Type_B_img_directory,'*tif*']);
if size(type_B_imgs,1)==0
    type_B_imgs=dir([Type_B_img_directory,'*png*']);
end

% Setup inflate grown directories
Inflate_folder_names=cell(size(num_of_vox_to_search,1),1);
To_inflate_or_already_inflated_images=ones(size(num_of_vox_to_search,1),1);

back_slash_pos=strfind(Type_A_img_directory,'\');
Grow_img_directory=[Type_A_img_directory(back_slash_pos(end-1):back_slash_pos(end)-
1),'_dilated_images'];

for i=1:size(num_of_vox_to_search,1)

Inflate_folder_names{i}=[Inflate_main_folders,Grow_img_directory,'_grown_',num2str(roun
d(radii_to_examine(i))),'_um'];
    if ~exist(Inflate_folder_names{i},'dir')
        mkdir(Inflate_folder_names{i});
    else
        cur_imgs=dir([Inflate_folder_names{i},'*tif*']);
        if size(cur_imgs,1)<size(type_A_imgs,1)
            To_inflate_or_already_inflated_images(i)=1;
        else
            To_inflate_or_already_inflated_images(i)=0;
        end
    end
end

% Grow directories that need to be grown
for i=1:size(radii_to_examine,1)
    if To_inflate_or_already_inflated_images(i)==1
        % Grow Seed Images

Amira_grown_surface(Code_storage_directory,Type_A_img_directory,Inflate_folder_names{
i},num_of_vox_to_search(i));
    end
end

% Set up number of object storage arrays
num_type_B_objects=zeros(size(num_of_vox_to_search,1),1);
num_type_B_objects_near_type_A_objects=zeros(size(num_of_vox_to_search,1),1);
type_B_objects=cell(size(num_of_vox_to_search,1),1);
type_B_objects_near_type_A_objects=cell(size(num_of_vox_to_search,1),1);

% Set up percentage storage array
perc_type_B_objects_near_type_A_obejcts=zeros(size(num_of_vox_to_search,1),1);

% Set up dilated image names
dilated_imgs=dir([Inflate_folder_names{1},'*tif*']);

```

```

% Examine overlap
display(['Analyzing for savevar : ',save_variable]);
for radius=1:size(radii_to_examine,1)
    num_type_B_objects_holder=[];
    num_type_B_objects_near_type_B_holder=[];
    for image_slice=1:size(type_B_imgs,1)
        % Read in dilated image on current slice
        dilated_img=imread([Inflate_folder_names{radius},dilated_imgs(image_slice).name]);

        % Read in type B images but ensure they are the same size as type A
        % images (Padding may occur in some processing steps from Amira)

type_B_img=imread([Type_B_img_directory,type_B_imgs(image_slice+((size(type_B_imgs,
1)-size(dilated_imgs,1))/2)).name]);

        % Calculate the type B objects that overlap with the dilated type A
        % objects
        type_B_near_type_A_img=uint32(type_B_img).*uint32(logical(dilated_img));

        num_type_B_objects_holder=[num_type_B_objects_holder;unique(type_B_img)];

num_type_B_objects_near_type_B_holder=[num_type_B_objects_near_type_B_holder;unique
(type_B_near_type_A_img)];
    end

    % Store number of object data
    num_type_B_objects(radius)=size(unique(num_type_B_objects_holder),1)-1;

num_type_B_objects_near_type_A_objects(radius)=size(unique(num_type_B_objects_near_t
ype_B_holder),1)-1;

    % Store object data
    type_B_objects{radius}=num_type_B_objects_holder;
    type_B_objects_near_type_A_objects{radius}=num_type_B_objects_near_type_B_holder;

    % Calculate the percentage of type B objects near type A objects

perc_type_B_objects_near_type_A_obejcts(radius)=num_type_B_objects_near_type_A_objec
ts(radius)/num_type_B_objects(radius);

    display(['Here are the results for the current sample at a radius searched of
',num2str(round(radii_to_examine(radius))),' um']);
    display(['The number of base objects is ',num2str(num_type_B_objects(radius))]);
    display(['The number of base objects near grown objects is
',num2str(num_type_B_objects_near_type_A_objects(radius))]);
    display(['The percentage of base objects near grown objects is
',num2str(perc_type_B_objects_near_type_A_obejcts(radius))]);
end

```

```
save([Matlab_save_directory,save_variable],'num_type_B_objects','num_type_B_objects_near_type_A_objects',...  
  
'type_B_objects','type_B_objects_near_type_A_objects','perc_type_B_objects_near_type_A_objects','-v7.3');  
end
```

## **Image Randomization SOP**

### **Purpose**

The purpose of this SOP is to explain how to use the software in the Randomly Distributed Image Creator Code to either create a stack of images that contain a random distribution of surface voxels or volume voxels. The output of this code will be used with the Volume Based Spatial Correlation software as well as possible future code.

### **Methods**

1. Collect and organize all the images that you want to use to calculate the number of voxels to use for randomization in a folder with a recognizable name. (The images must be in tif or tiff format)
  - a. In the Ref Data example, this folder is the To\_randomize\_directory
2. Collect and organize all the images that you want to use as the base of the structure where the random voxels will be placed in a folder with a recognizable name. (The images must be in tif or tiff format)
  - a. In the Ref Data example, this folder is the Base\_image\_directory
3. Create a folder to hold all the randomized images with a recognizable name.
  - a. In the Ref Data, this folder is the Randomly\_distributed\_directory
4. Create a folder to hold the output Matlab variable
  - a. In the Ref Data, this folder is the Matlab\_variable\_output
5. Put all the folders in a main folder with a recognizable name.
6. Decide on a name for your Matlab output variable (DO NOT PUT any .mat etc in the name)

- a. In the Ref Data, this is called voxel\_locations
7. Open the Random\_image\_creator in Matlab
    - a. Run this program by opening it and pressing either the Run button or F5
      - i. You will possibly be prompted: “To run this file, you can either change the MATLAB current folder or add its folder to the MATLAB path”
        1. Choose “Change Folder”
  8. Follow prompts from the program
    - a. Choose the folders and input the information that is requested
  9. Unless you have significant experience with Matlab do not attempt to change code or use debug mode known as matt\_mode

### **Image Randomization Software**

```
function Random_image_creator(To_randomize_dir,Base_image_dir,...
Randomly_dist_dir,Save_dir,save_variable)
% Purpose: The purpose of this code is to determine the volume of material in
% the To_randomize_dir, determine the structure of the Base_image_dir,
% create an output of randomly distributed images in the Randomly_dist_dir
% and save the positions of the original image voxels, the main structures voxels
% and the randomly distributed voxels into the save_variable in the Save_dir

% Last Edited on 2_25_2015 by MGG

% Inputs if nargin
if nargin==0
    Main_directory = uigetdir(['Pick the folder will to act as the main folder for the rest of the
folders',...
    'and contain the folders that have the volumes to randomize/structure/outputs']);
    To_randomize_dir = uigetdir([Main_directory,'\'],'Pick the folder that contains the images
that you want to randomize (i.e. Damage images)');
    Base_image_dir = uigetdir([Main_directory,'\'],'Pick the folder that contains the images that
you want to use as the base structure (i.e. Bone Images)');
```

```

Name_random_dist_dir = input('What do you want to call the folder containing the random
images?');
Randomly_dist_dir = [Main_directory,'\Name_random_dist_dir];

Name_save_folder = input('What do you want to call the folder containing the output
matlab variable?');
Save_dir = [Main_directory,'\Name_save_folder];

save_variable=input('What do you want call the output matlab variable (do not include
.mat)?');
end

% Set up input directory list
To_randomize_dir=[To_randomize_dir,'\];
Base_image_dir=[Base_image_dir,'\];

% Set up output directory list
Randomly_dist_dir=[Randomly_dist_dir,'\];
Save_dir=[Save_dir,'\];
save_variable=[save_variable,'.mat'];

if ~exist(Randomly_dist_dir,'dir')
    mkdir(Randomly_dist_dir);
end
if ~exist(Save_dir,'dir')
    mkdir(Save_dir);
end

% Set up input image names
To_rand_imgs=dir([To_randomize_dir,'*tif*']);
Base_imgs=dir([Base_image_dir,'*tif*']);

% Create output image names
output_names=cell(size(Base_imgs,1),1);
for i=1:size(output_names,1)
    output_names{i}=sprintf('Randomly_distributed_image_%04d.tif', i);
end
Output_images=struct('name',output_names);

continue_variable=1;

% Check to make sure you aren't going to overwrite the previously save
% images
if continue_variable
    img_write=1;
else
    img_write=input('The save variable already exists which suggests this code has already
been run. Are you sure you want to continue and overwrite old images? (1=yes, 0=no)');
end

```

```

if continue_variable
    % Calculate the amount of voxels in the To_randomize_dir and the
    % position of the voxels in the To_randomize_dir
    to_randomize_voxels=[];
    time_spent=[];
    n=0;
    fprintf('Calculating position and number of voxels to randomize \n');
    for i=1:size(To_rand_imgs)
        tic;

        fprintf(repmat('\b',1,n));
        msg=['Percent done: ',num2str(100*i/size(To_rand_imgs,1)), ' perc ',...
            'Estimated Time Left: ',num2str((mean(time_spent)*(size(To_rand_imgs,1)-i))/60),'
min'];
        fprintf(msg);
        n=numel(msg);

        to_randomize_img=imread([To_randomize_dir,To_rand_imgs(i).name], 'tif');

        [x_val,y_val]=find(to_randomize_img);
        new_z=i*ones(size(x_val));

        to_randomize_voxels=[to_randomize_voxels;x_val,y_val,new_z];
        time_spent=[time_spent;toc];
    end
    num_voxels_to_randomize=size(to_randomize_voxels,1);

    % Calculate the position of all the voxels in the Base_image_dir
    base_img_voxels=[];
    time_spent=[];
    n=0;
    fprintf('\nCalculating position of the base image voxels \n');
    for i=1:size(Base_imgs)
        tic;

        fprintf(repmat('\b',1,n));
        msg=['Percent done: ',num2str(100*i/size(Base_imgs,1)), ' perc ', ...
            'Estimated Time Left: ',num2str((mean(time_spent)*(size(Base_imgs,1)-i))/60),' min'];
        fprintf(msg);
        n=numel(msg);

        base_img=imread([Base_image_dir,Base_imgs(i).name], 'tif');

        [x_val,y_val]=find(base_img);
        new_z=i*ones(size(x_val));

        base_img_voxels=[base_img_voxels;x_val,y_val,new_z];
        time_spent=[time_spent;toc];
    end
end

```

```

fprintf('\n');

% Calculate the position of all the random voxels
rand_vox_mat=randperm(size(base_img_voxels,1));
rand_vox_pos=rand_vox_mat(1:num_voxels_to_randomize);
clear rand_vox_mat

random_img_voxels=base_img_voxels(rand_vox_pos,:);

else
    load([Save_dir,save_variable],'random_img_voxels');
end

if img_write
    % Save variable

save([Save_dir,save_variable],'to_randomize_voxels','base_img_voxels','random_img_voxels',
'-v7.3');
clear to_randomize_voxels base_img_voxels

% Organize random img voxel array
random_img_voxels=sortrows(random_img_voxels,3);
[vals,pos]=unique(random_img_voxels(:,3));
if pos(1)==1
    pos=[pos;size(random_img_voxels(:,3),1)];
else
    pos=[1;pos];
end

% Create blank image stack in Random_dmg_dir
tmp_img=imread([Base_image_dir,Base_imgs(1).name],'tif');
[x_size,y_size]=size(tmp_img);
clear tmp_img

imwrite(zeros(x_size,y_size),[Randomly_dist_dir,Output_images(1).name],'tif');
for i=2:size(Output_images,1)

copyfile([Randomly_dist_dir,Output_images(1).name],[Randomly_dist_dir,Output_images(i).
name]);
end

% Write out randomly distributed images
for i=1:size(vals,1)
    cur_img=zeros(x_size,y_size);
    x_positions=random_img_voxels(pos(i)+1:pos(i+1),1);
    y_positions=random_img_voxels(pos(i)+1:pos(i+1),2);
    ind=sub2ind(size(cur_img),double(x_positions),double(y_positions));
    cur_img(ind)=1;
    imwrite(uint8(cur_img),[Randomly_dist_dir,Output_images(vals(i)).name],'tif');
end

```

end

## Additional Necessary Software

```
function Amira_grown_surface(main_dir,files_to_grow,...
grown_folder,number_times_grow)
% This function will allow you to create a surface and then grow the
% surface of a tiffstack using amira

tcl_file=[main_dir,'grown_surface.tcl'];

tcl_grow_folder=strrep(files_to_grow,'\','/');
tcl_grow_folder=["",tcl_grow_folder,""];
tcl_coarsened_dir=strrep(grown_folder(1:end-1),'\','/');
num_times_close=number_times_grow;

fid2=fopen(tcl_file,'w');
fprintf(fid2,['# Amira-Script-Object V3.0\n\n set NumGrow ',num2str(num_times_close+1),'\n
set specimen 1\n\n']);
fprintf(fid2,'# ~~~~~~LOADING
IMAGES~~~~~\n echo -> Loading
Images...\n\n');
fprintf(fid2,['set path ', tcl_grow_folder, '\n cd $path\n\n']);
fprintf(fid2,'set imageName [glob "*.tif"]\nset Nims [length $imageName]\nset imageName
[index $imageName 0]\nset initIm "$path/$imageName"\n');
fprintf(fid2,'load -tif +box 0 1 0 1 0 1 +mode 2 $initIm\n$imageName setLabel test\n');
fprintf(fid2,'set imageSize [test getDims]\necho \tX-DIM: [index $imageSize 0] \t Y-DIM:
[index $imageSize 1] \t Z-DIM: $Nims\nremove test\n\n');
fprintf(fid2,'set images [glob "*.tif"]\n eval load -tif +box 0 [expr 1*([index $imageSize 0]-
1)] 0 [expr 1*([index $imageSize 1]-1)] 0 [expr 1*($Nims-1)] +mode 2 $images\n');
fprintf(fid2,['index $images 0] setLabel $specimen\\.FIT.ROI.PTD\n\n');
fprintf(fid2,'# ~~~~~~LABEL
VOXELS~~~~~\n');
fprintf(fid2,'echo -> Labeling...\n\n create HxLabelVoxel LABELS.$specimen\n
LABELS.$specimen data connect $specimen\\.FIT.ROI.PTD\nLABELS.$specimen regions
setValue "Background Signal"\n');
fprintf(fid2,'LABELS.$specimen boundary01 setValue 0\n LABELS.$specimen create\n
remove LABELS.$specimen\n # $specimen\\.Labels setLabel $specimen\\.Labels\n\n');
fprintf(fid2,'#
~~~~~CLOSING~~~~~
~~~~~\ncreate HxGiEditor EDIT.$specimen\n\n');
fprintf(fid2,['EDIT.$specimen attach $specimen\\.FIT.ROI.Labels\n EDIT.$specimen
selectMaterial2 1\n echo -> CLOSING WITH STREL OF ',num2str(num_times_close+1),'
\n']);
% grows 1 voxel in all directions
fprintf(fid2,'for {set d 1} {$d < $NumGrow} {incr d} {EDIT.$specimen
growSelection3D}\n');
```

```

fprintf(fid2,'EDIT.$specimen add 1\n EDIT.$specimen detach\n remove EDIT.$specimen\n');
fprintf(fid2,['$specimen\\.FIT.ROI.Labels save "2D Tiff"
"',tcl_coarsened_dir,'/images####.tif"\n']);
fclose(fid2);

tcl_file=strrep(tcl_file,'\','/');
tcl_file=["'",tcl_file,"'"];

if exist('C:/Program Files/Amira 5.4.1/bin/arch-Win64VC9-Optimize/amiramain.exe','file')
    location=["C:/Program Files/Amira 5.4.1/bin/arch-Win64VC9-Optimize/amiramain" -
nogui ', tcl_file];
elseif exist('C:/Program Files/Amira 5.3.3/bin/arch-Win64VC9-Optimize/amiramain.exe','file')
    location=["C:/Program Files/Amira 5.3.3/bin/arch-Win64VC9-Optimize/amiramain" -
nogui ', tcl_file];
else
    file_location= subdir([pwd,'*amiramain.exe']);
    filename= file_location.name;
    location=["'",filename(1:end-4)," -nogui ', tcl_file];
end
% location=["C:/Program Files/Amira 5.4.1/bin/arch-Win64VC9-Optimize/amiramain" ',
tcl_file];

system(location);

to_delete=dir([tcl_coarsened_dir,'/*info']);
delete([tcl_coarsened_dir,'/',to_delete.name]);

end

```

## Inflate Algorithm Validation

### Code used to perform Validation

```
% Inflate validation code
main_dir='N:\Inflate_validate\';

nobj=200;
size_obj=5;
max_distance=10;

min_dist_from_surf_1A=20;
max_dist_from_surf_1A=50;

min_dist_from_surf_1B=60;

step_1=0;
step_2=0;
step_3=0;
step_4=1;

radii_to_examine=0:100;
radii_to_examine=radii_to_examine';
vox_size=1;

seed_dir=[main_dir,'Seed_imgs\'];
seach_dir=[main_dir,'Search_imgs\',num2str(nobj),'_cubes_with_size_legnth_',num2str(size_
obj),'\'];
full_img_dir=[main_dir,'Full_imgs\',num2str(nobj),'_cubes_with_size_legnth_',num2str(size_
obj),'\'];
random_var_dir=[main_dir,'Random_vars\',num2str(nobj),'_cubes_with_size_legnth_',num2st
r(size_obj),'\'];
random_img_dir=[main_dir,'Random_img\',num2str(nobj),'_cubes_with_size_legnth_',num2st
r(size_obj),'\'];
grown_dir=[main_dir,'Grown_imgs\',num2str(nobj),'_cubes_with_size_legnth_',num2str(size_
obj),'\'];
code_dir=[main_dir,'Code_dir\',num2str(nobj),'_cubes_with_size_legnth_',num2str(size_obj),'
\'];
inflate_results_dir=[main_dir,'Inflate_results\',num2str(nobj),'_cubes_with_size_legnth_',num
2str(size_obj),'\'];
validation_results_dir=[main_dir,'Validation_results\',num2str(nobj),'_cubes_with_size_legnth
_',num2str(size_obj),'\'];

% Step 1: Create images for validations
if step_1
    % 1A Create 1 set of images that is 200 x 200 x 200 voxels with nobj cubic
    % objects of size_obj^3 voxels that are randomly place more than min_dist_from_surf_1A
voxels
    % from the surface and less than max_dist_from_surf_1A voxels from the surface
```

```

blk_img=zeros(200,200,200);

shell_img=zeros(size(blk_img,1)-2*min_dist_from_surf_1A,size(blk_img,2)-
2*min_dist_from_surf_1A,size(blk_img,3)-2*min_dist_from_surf_1A);
shell_img(max_dist_from_surf_1A-min_dist_from_surf_1A/2:size(blk_img,1)-
(max_dist_from_surf_1A-min_dist_from_surf_1A/2),...
max_dist_from_surf_1A-min_dist_from_surf_1A/2:size(blk_img,2)-
(max_dist_from_surf_1A-min_dist_from_surf_1A/2),...
max_dist_from_surf_1A-min_dist_from_surf_1A/2:size(blk_img,3)-
(max_dist_from_surf_1A-min_dist_from_surf_1A/2))=1;
shell_img=~shell_img;

[x_pos,y_pos,z_pos]=ind2sub(size(shell_img),find(shell_img == 1));
shell_pos=sub2ind(size(blk_img),x_pos+min_dist_from_surf_1A,...
y_pos+min_dist_from_surf_1A,...
z_pos+min_dist_from_surf_1A);

rand_shell_pts=randperm(size(shell_pos,1));
rand_vox_pos=rand_shell_pts(1:nobj);

seed_pts=shell_pos(rand_vox_pos);

blk_img(seed_pts)=1;

[x_seed_1a,y_seed_1a,z_seed_1a]=ind2sub(size(blk_img),seed_pts);

for i1=1:size_obj
    for i2=1:size_obj
        for i3=1:size_obj
            cur_pts=sub2ind(size(blk_img),x_seed_1a+i1-1,y_seed_1a+i2-1,z_seed_1a+i3-1);
            blk_img(cur_pts)=1;
        end
    end
end

seed_1A_name=['Seed_',num2str(min_dist_from_surf_1A),'_to_',num2str(max_dist_from_surf_1A),'_from_surf'];
seed_1A_dir=[seed_dir,seed_1A_name,'\'];

if ~exist(seed_1A_dir)
    mkdir(seed_1A_dir);
end

for img=1:size(blk_img,3)
    cur_img_name=sprintf('Seed_img_%04d.tif',img);
    imwrite(blk_img(:,:,img),[seed_1A_dir,cur_img_name]);
end

```

```

% 1B Create 1 set of images that is 200 x 200 x 200 voxels with nobj cubic
% objects of size_obj^3 voxels that are randomly places more than min_dist_from_surf_1B
voxesl
% from the surface
blk_img=zeros(200,200,200);

shell_img=zeros(200,200,200);
shell_img(min_dist_from_surf_1B:size(blk_img,1)-min_dist_from_surf_1B,...
    min_dist_from_surf_1B:size(blk_img,2)-min_dist_from_surf_1B,...
    min_dist_from_surf_1B:size(blk_img,3)-min_dist_from_surf_1B)=1;

[x_pos,y_pos,z_pos]=ind2sub(size(shell_img),find(shell_img == 1));
shell_pos=sub2ind(size(blk_img),x_pos,y_pos,z_pos);

rand_shell_pts=randperm(size(shell_pos,1));
rand_vox_pos=rand_shell_pts(1:nobj);

seed_pts=shell_pos(rand_vox_pos);

[x_seed_1b,y_seed_1b,z_seed_1b]=ind2sub(size(blk_img),seed_pts);

for i1=1:size_obj
    for i2=1:size_obj
        for i3=1:size_obj
            cur_pts=sub2ind(size(blk_img),x_seed_1b+i1-1,y_seed_1b+i2-1,z_seed_1b+i3-1);
            blk_img(cur_pts)=1;
        end
    end
end

seed_1B_name=['Seed_more_',num2str(min_dist_from_surf_1B),'_from_surf'];
seed_1B_dir=[seed_dir,seed_1B_name,'\'];

if ~exist(seed_1B_dir)
    mkdir(seed_1B_dir);
end

for img=1:size(blk_img,3)
    cur_img_name=sprintf('Seed_img_%04d.tif',img);
    imwrite(blk_img(:,:,img),[seed_1B_dir,cur_img_name]);
end

% 1C Create 5 additional sets of images from 1A where each object is moved
% to the left 1 extra voxel in each set of images resulting in 5 sets of
% images with nobj objects that are between 0 to max_distance voxels away from the
% original images
seed_1C_name_dir=cell(6,1);
for dist=1:max_distance
    blk_img=zeros(200,200,200);

```

```

x_seed_1c=x_seed_1a;
y_seed_1c=y_seed_1a+dist-1;
z_seed_1c=z_seed_1a;

for i1=1:size_obj
    for i2=1:size_obj
        for i3=1:size_obj
            cur_pts=sub2ind(size(blk_img),x_seed_1c+i1-1,y_seed_1c+i2-1,z_seed_1c+i3-
1);
            blk_img(cur_pts)=1;
        end
    end
end

seed_1C_name_dir{dist}=[seach_dir,'Seed_',num2str(min_dist_from_surf_1A),'_to_',num2str
(max_dist_from_surf_1A),'_from_surf_shifted_',num2str(dist),'\'];

if ~exist(seed_1C_name_dir{dist})
    mkdir(seed_1C_name_dir{dist});
end

for img=1:size(blk_img,3)
    cur_img_name=sprintf('Search_img_%04d.tif',img);
    imwrite(blk_img(:,:,img),[seed_1C_name_dir{dist},cur_img_name]);
end
end

% 1D Do the same thing for as in 1C for 1B
seed_1D_name_dir=cell(6,1);
for dist=1:max_distance
    blk_img=zeros(200,200,200);

    x_seed_1d=x_seed_1b;
    y_seed_1d=y_seed_1b+dist-1;
    z_seed_1d=z_seed_1b;

    for i1=1:size_obj
        for i2=1:size_obj
            for i3=1:size_obj
                cur_pts=sub2ind(size(blk_img),x_seed_1d+i1-1,y_seed_1d+i2-1,z_seed_1d+i3-
1);
                blk_img(cur_pts)=1;
            end
        end
    end
end

```

```

seed_1D_name_dir{dist}=[seach_dir,'Seed_more_',num2str(min_dist_from_surf_1B),'_from_
surf_shifted_',num2str(dist),'\'];

    if ~exist(seed_1D_name_dir{dist})
        mkdir(seed_1D_name_dir{dist});
    end

    for img=1:size(blk_img,3)
        cur_img_name=sprintf('Search_img_%04d.tif',img);
        imwrite(blk_img(:,:,img),[seed_1D_name_dir{dist},cur_img_name]);
    end
end
end
% Step 2: Create random images

if step_2
    % 2A create black full image
    blk_img=ones(200,200,200);

    if ~exist(full_img_dir)
        mkdir(full_img_dir);
    end

    for img=1:size(blk_img,3)
        cur_img_name=sprintf('Full_img%04d.tif',img);
        imwrite(blk_img(:,:,img),[full_img_dir,cur_img_name]);
    end

    % 2B create random image that works for 1C and 1D
    random_1C_img_dir=cell(6,1);
    random_1C_var_dir=cell(6,1);
    for dist=1:max_distance
        random_1C_img_dir{dist}=[random_img_dir,'Rand_1C_dist_',num2str(dist),'\'];
        random_1C_var_dir{dist}=[random_var_dir,'Rand_1C_dist_',num2str(dist),'\'];

        if ~exist(random_1C_img_dir{dist})
            mkdir(random_1C_img_dir{dist});
        end

        rand_dmg_save_variable='random_var';

        Random_image_creator(seed_1C_name_dir{dist},full_img_dir,random_1C_img_dir{dist}(1:
end-1),random_1C_var_dir{dist}(1:end-1),rand_dmg_save_variable);
    end

    random_1D_img_dir=cell(6,1);
    random_1D_var_dir=cell(6,1);
    for dist=1:max_distance
        random_1D_img_dir{dist}=[random_img_dir,'Rand_1D_dist_',num2str(dist),'\'];

```

```

random_1D_var_dir{dist}=[random_var_dir,'Rand_1D_dist_',num2str(dist),'\'];

if ~exist(random_1D_img_dir{dist})
    mkdir(random_1D_img_dir{dist});
end

rand_dmg_save_variable='random_var';

Random_image_creator(seed_1D_name_dir{dist},full_img_dir,random_1D_img_dir{dist})(1:
end-1),random_1D_var_dir{dist}(1:end-1),rand_dmg_save_variable);
end
end
% Step 3: Run inflate

if step_3
    %3A Run inflate with 1A as the seed and 1C as the search for distances of 1
    %to 5 voxels
    for dist=1:max_distance
        Type_A_img_directory=seed_1A_dir;
        Type_B_img_directory=seed_1C_name_dir{dist};
        Rand_type_B_img_directory=random_1C_img_dir{dist};
        Matlab_save_directory=[inflate_results_dir,'1A_seed_1C_search'];
        Inflate_main_folders=[grown_dir,'1A_seed'];
        save_variable=['1A_seed_1C_search_dist_',num2str(dist)];
        if ~exist(Matlab_save_directory,'dir')
            mkdir(Matlab_save_directory)
        end
        if ~exist(Inflate_main_folders,'dir')
            mkdir(Inflate_main_folders)
        end
        Volume_based_spatial_correlation(code_dir(1:end-
1),Type_A_img_directory,Type_B_img_directory,Rand_type_B_img_directory,...
Matlab_save_directory,Inflate_main_folders,save_variable,radii_to_examine,vox_size);
    end

    %3B Run inflate with 1B as the seed and 1D as the search for distances of 1
    %to 5 voxels
    for dist=1:max_distance
        Type_A_img_directory=seed_1B_dir;
        Type_B_img_directory=seed_1D_name_dir{dist};
        Rand_type_B_img_directory=random_1D_img_dir{dist};
        Matlab_save_directory=[inflate_results_dir,'1B_seed_1D_search'];
        Inflate_main_folders=[grown_dir,'1B_seed'];
        save_variable=['1B_seed_1D_search_dist_',num2str(dist)];
        if ~exist(Matlab_save_directory,'dir')
            mkdir(Matlab_save_directory)
        end
        if ~exist(Inflate_main_folders,'dir')
            mkdir(Inflate_main_folders)
        end
    end
end

```

```

    end
    Volume_based_spatial_correlation(code_dir(1:end-
1),Type_A_img_directory,Type_B_img_directory,Rand_type_B_img_directory,...
Matlab_save_directory,Inflate_main_folders,save_variable,radii_to_examine,vox_size);
end

%3C Run inflate with 1A as the seed and 1D as the search for distances of 1
%to 5 voxels
for dist=1:max_distance
    Type_A_img_directory=seed_1A_dir;
    Type_B_img_directory=seed_1D_name_dir{dist};
    Rand_type_B_img_directory=random_1D_img_dir{dist};
    Matlab_save_directory=[inflate_results_dir,'1A_seed_1D_search'];
    Inflate_main_folders=[grown_dir,'1A_seed'];
    save_variable=['1A_seed_1D_search_dist_',num2str(dist)];
    if ~exist(Matlab_save_directory,'dir')
        mkdir(Matlab_save_directory)
    end
    if ~exist(Inflate_main_folders,'dir')
        mkdir(Inflate_main_folders)
    end
    Volume_based_spatial_correlation(code_dir(1:end-
1),Type_A_img_directory,Type_B_img_directory,Rand_type_B_img_directory,...
Matlab_save_directory,Inflate_main_folders,save_variable,radii_to_examine,vox_size);
end

%3D Run inflate with 1B as the seed and 1C as the search for distances of 1
%to 5 voxels
for dist=1:max_distance
    Type_A_img_directory=seed_1B_dir;
    Type_B_img_directory=seed_1C_name_dir{dist};
    Rand_type_B_img_directory=random_1C_img_dir{dist};
    Matlab_save_directory=[inflate_results_dir,'1B_seed_1C_search'];
    Inflate_main_folders=[grown_dir,'1C_seed'];
    save_variable=['1B_seed_1C_search_dist_',num2str(dist)];
    if ~exist(Matlab_save_directory,'dir')
        mkdir(Matlab_save_directory)
    end
    if ~exist(Inflate_main_folders,'dir')
        mkdir(Inflate_main_folders)
    end
    Volume_based_spatial_correlation(code_dir(1:end-
1),Type_A_img_directory,Type_B_img_directory,Rand_type_B_img_directory,...
Matlab_save_directory,Inflate_main_folders,save_variable,radii_to_examine,vox_size);
end
end

```

```

% Step 4: Collect data from inflate
inflate_output_1A_1C=cell(size(radii_to_examine,1)+1,max_distance+1);
inflate_output_1B_1D=cell(size(radii_to_examine,1)+1,max_distance+1);
inflate_output_1A_1D=cell(size(radii_to_examine,1)+1,max_distance+1);
inflate_output_1B_1C=cell(size(radii_to_examine,1)+1,max_distance+1);
if step_4
    inflate_output_1A_1C{1,1}='Distance_from_seed';
    for i=1:size(radii_to_examine,1)
        inflate_output_1A_1C{i+1,1}=i;
        inflate_output_1B_1D{i+1,1}=i;
        inflate_output_1A_1D{i+1,1}=i;
        inflate_output_1B_1C{i+1,1}=i;
    end
    for i=1:max_distance
        inflate_output_1A_1C{1,i+1}=['Shifted_by_',num2str(i),'_voxel'];

load([inflate_results_dir,'1A_seed_1C_search','\','1A_seed_1C_search_dist_',num2str(i)]);
    for i2=1:size(metric_output,1)
        inflate_output_1A_1C{i2+1,i+1}=metric_output(i2);
    end

        inflate_output_1B_1D{1,i+1}=['Shifted_by_',num2str(i),'_voxel'];

load([inflate_results_dir,'1B_seed_1D_search','\','1B_seed_1D_search_dist_',num2str(i)]);
    for i2=1:size(metric_output,1)
        inflate_output_1B_1D{i2+1,i+1}=metric_output(i2);
    end

        inflate_output_1A_1D{1,i+1}=['Shifted_by_',num2str(i),'_voxel'];

load([inflate_results_dir,'1A_seed_1D_search','\','1A_seed_1D_search_dist_',num2str(i)]);
    for i2=1:size(metric_output,1)
        inflate_output_1A_1D{i2+1,i+1}=metric_output(i2);
    end

        inflate_output_1B_1C{1,i+1}=['Shifted_by_',num2str(i),'_voxel'];
load([inflate_results_dir,'1B_seed_1C_search','\','1B_seed_1C_search_dist_',num2str(i)]);
    for i2=1:size(metric_output,1)
        inflate_output_1B_1C{i2+1,i+1}=metric_output(i2);
    end

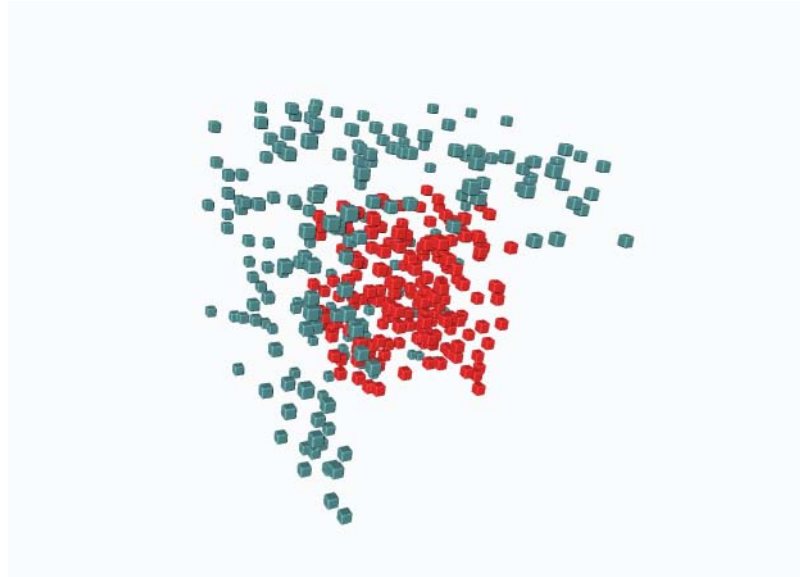
end
end

if ~exist(validation_results_dir(1:end-1))
    mkdir(validation_results_dir(1:end-1));
end

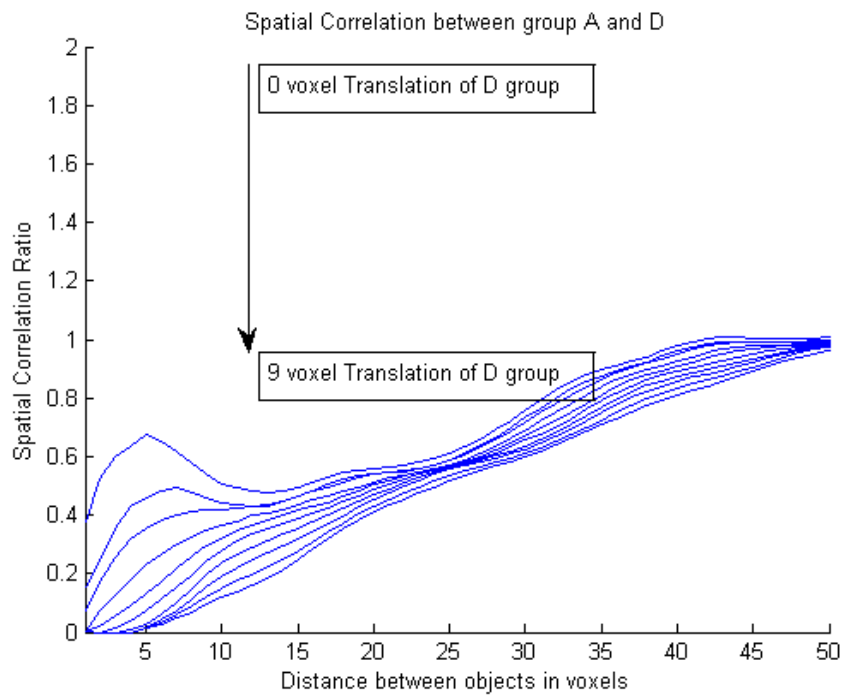
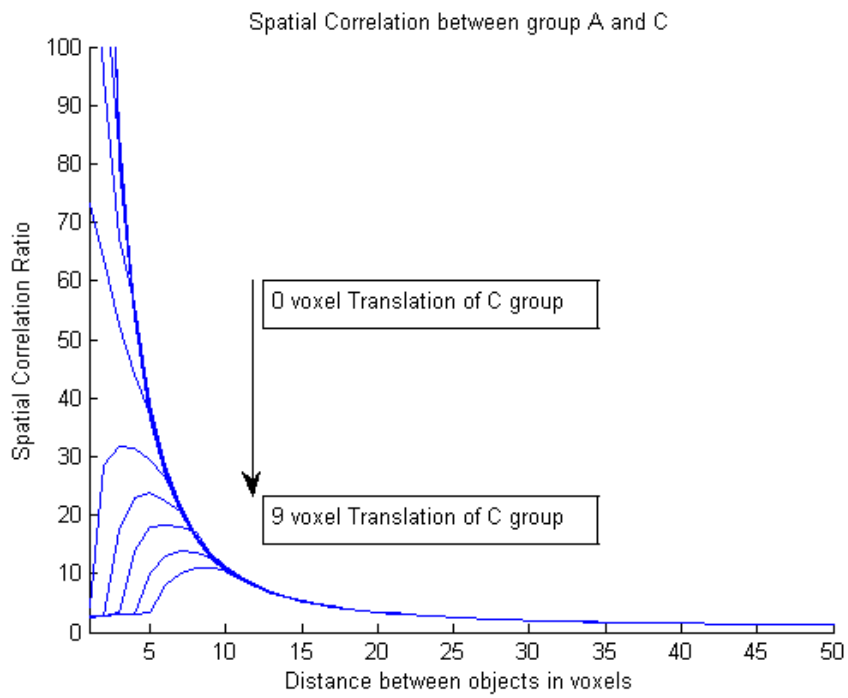
```

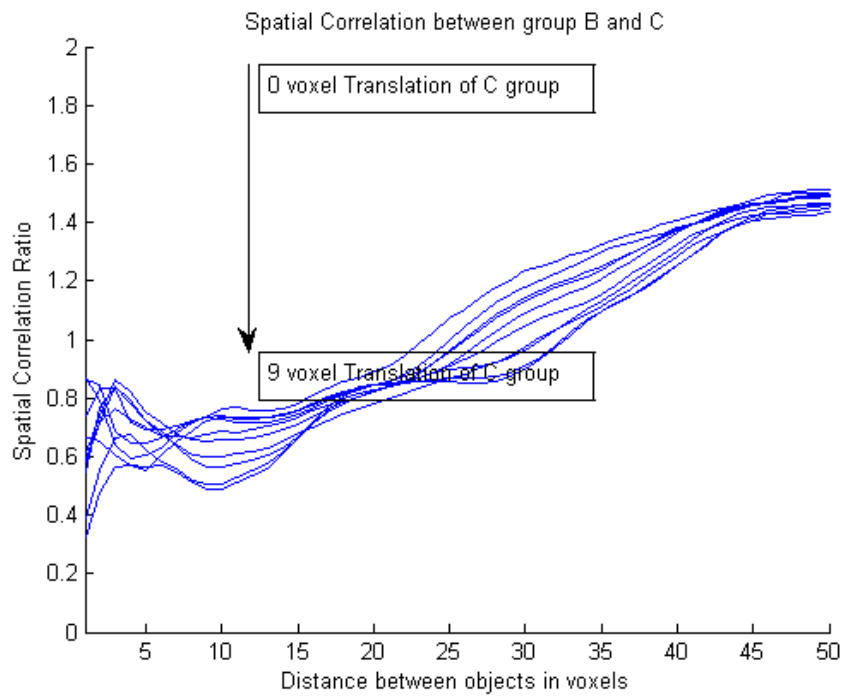
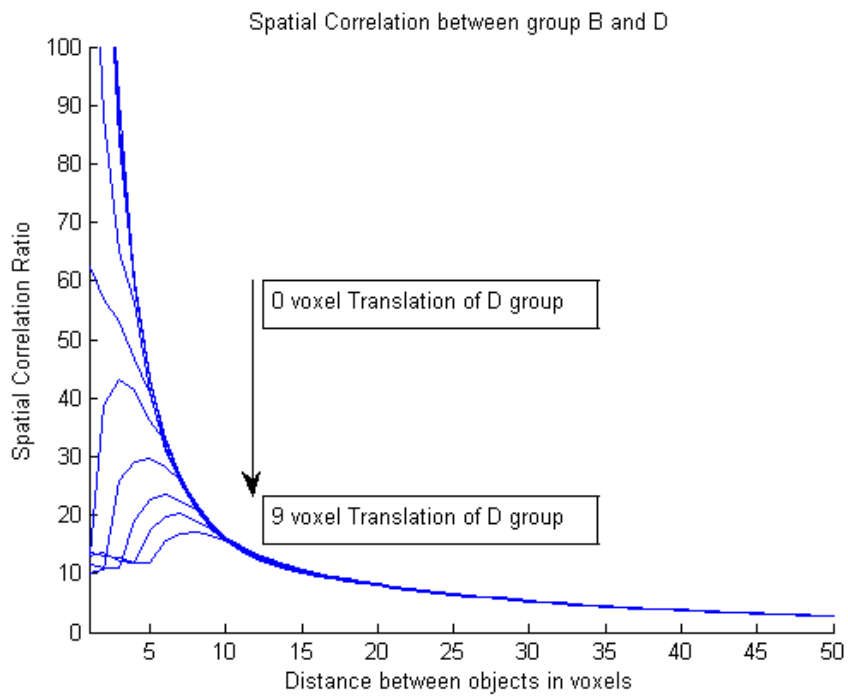
```
save([validation_results_dir,'validation_results.mat'],'inflate_output_1A_1C','inflate_output_1B_1D','inflate_output_1A_1D','inflate_output_1B_1C');
```

**Below is an Image of the Distribution of Objects Used for Validation**

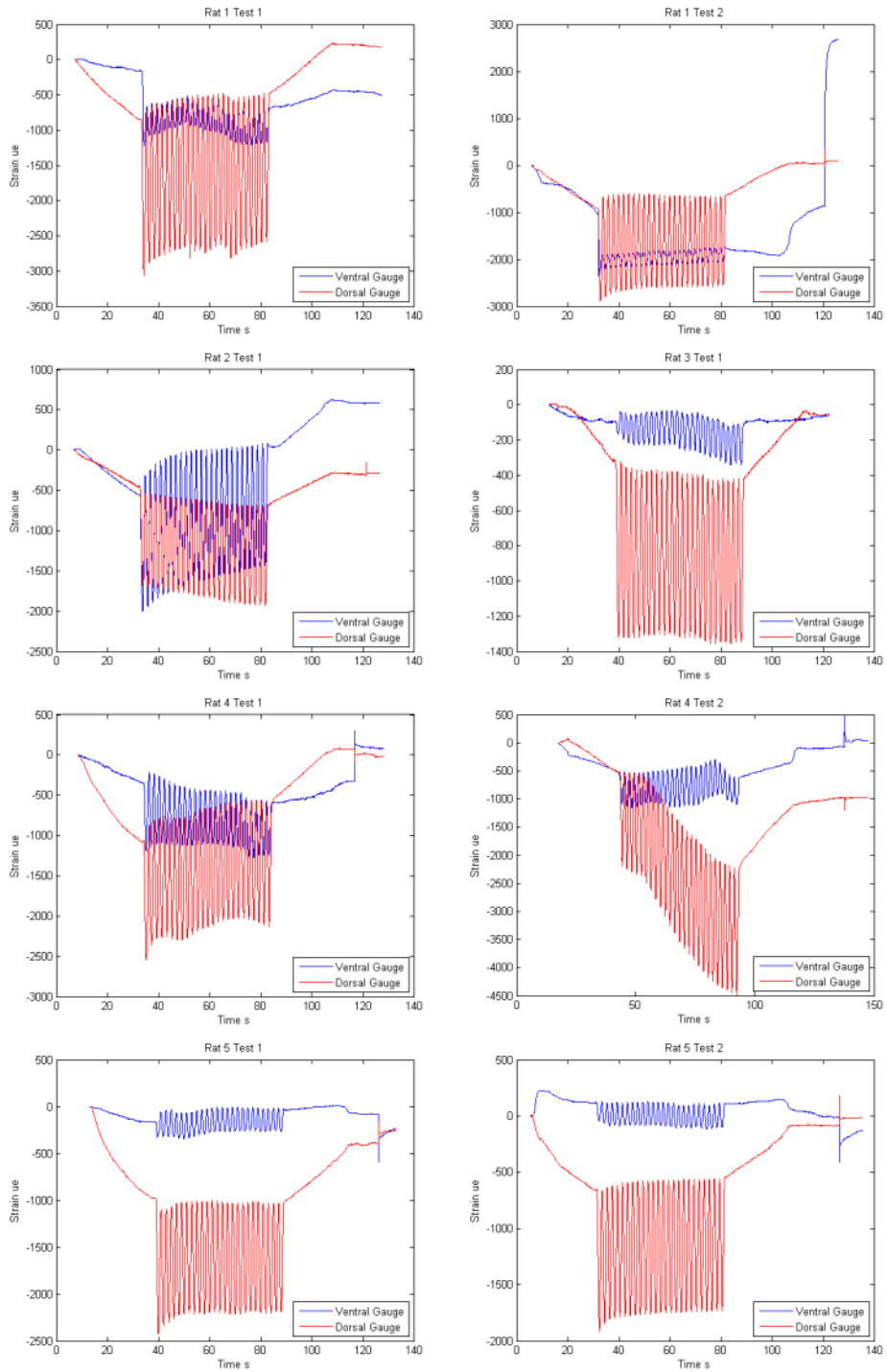


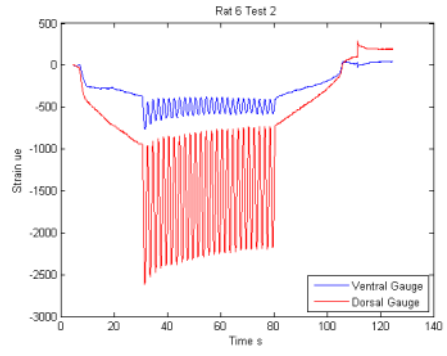
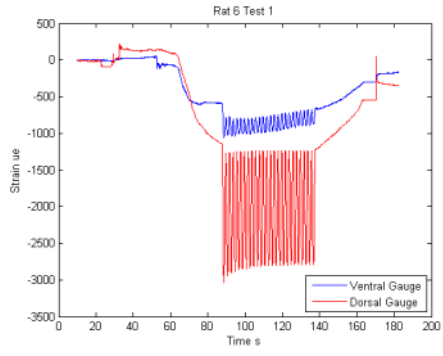
**Results of Validation:** Group A are the green cubes in the previous image, Group B are the red cubes in the previous image, Group C are several sets of objects that are the Group A objects translated by one voxel at a time, Group D are several sets of objects that are Group B objects translated by one voxel at a time. Group A and Group C objects should be spatially correlated and Group B and Group D objects should be spatially correlated. Group A and Group D objects should not be spatially correlated and Group B and Group C objects should not be spatially correlated. A spatial correlation ratio greater than 1 is a positive spatial correlation, equal to 1 is no spatial correlation and less than 1 is a negative spatial correlation.





## Strain Gauge Data



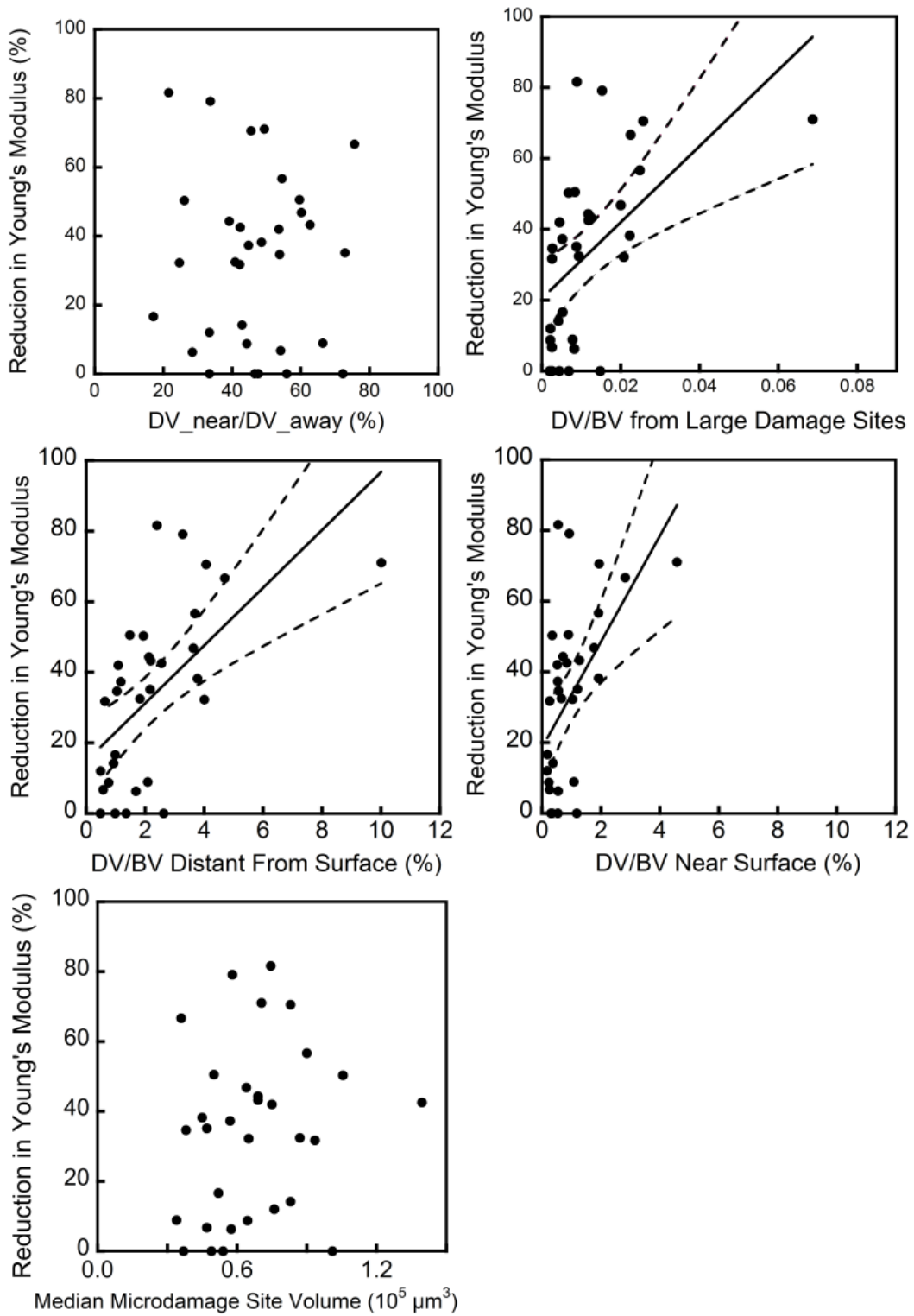


## APPENDIX B: CHAPTER 4 SUPPLEMENTARY MATERIAL

### Finite Element Data

To confirm that reductions in local mechanical stress/strain were not biasing the spatial correlations between resorption cavities and microdamage, high resolution finite element models were generated of the specimens involved in the spatial correlation analysis (n=9). Eight node brick elements, 10  $\mu\text{m}$  in size were used to model the trabecular microarchitecture. The element size is small relative to trabecular thickness ( average trabecular thickness exceeds 100  $\mu\text{m}$ ), but large compared to resorption cavity depth (30  $\mu\text{m}$  ), hence we expect element strains to accurately quantify strains associated with trabecular microstructure, but provide relatively little of the effects of stress concentrations associated with resorption cavities. Elements were assigned a Young's modulus of 18 GPa and a Poisson's ratio of 0.3. A 1% strain was applied to the cranial surface and the caudal surface was constrained in the vertical direction. Finite element models were analyzed using Olympus on a Sun Constellation Linux Cluster (Ranger; TACC, TX, USA). The von Mises strain within 10  $\mu\text{m}$  of resorption cavities ( $5400 \pm 1600 \mu\text{e}$ , mean  $\pm$  SD of nine specimens) was not significantly different from that elsewhere on the bone surface ( $4900 \pm 1000 \mu\text{e}$ ,  $p = 0.24$ , paired t-test), suggesting that the negative correlation between microdamage and resorption cavities was unlikely to be the result of reduced load distribution on trabeculae with cavities.

### Additional Measures Performed



APPENDIX C: CHAPTER 5 SUPPLEMENTARY MATERIAL

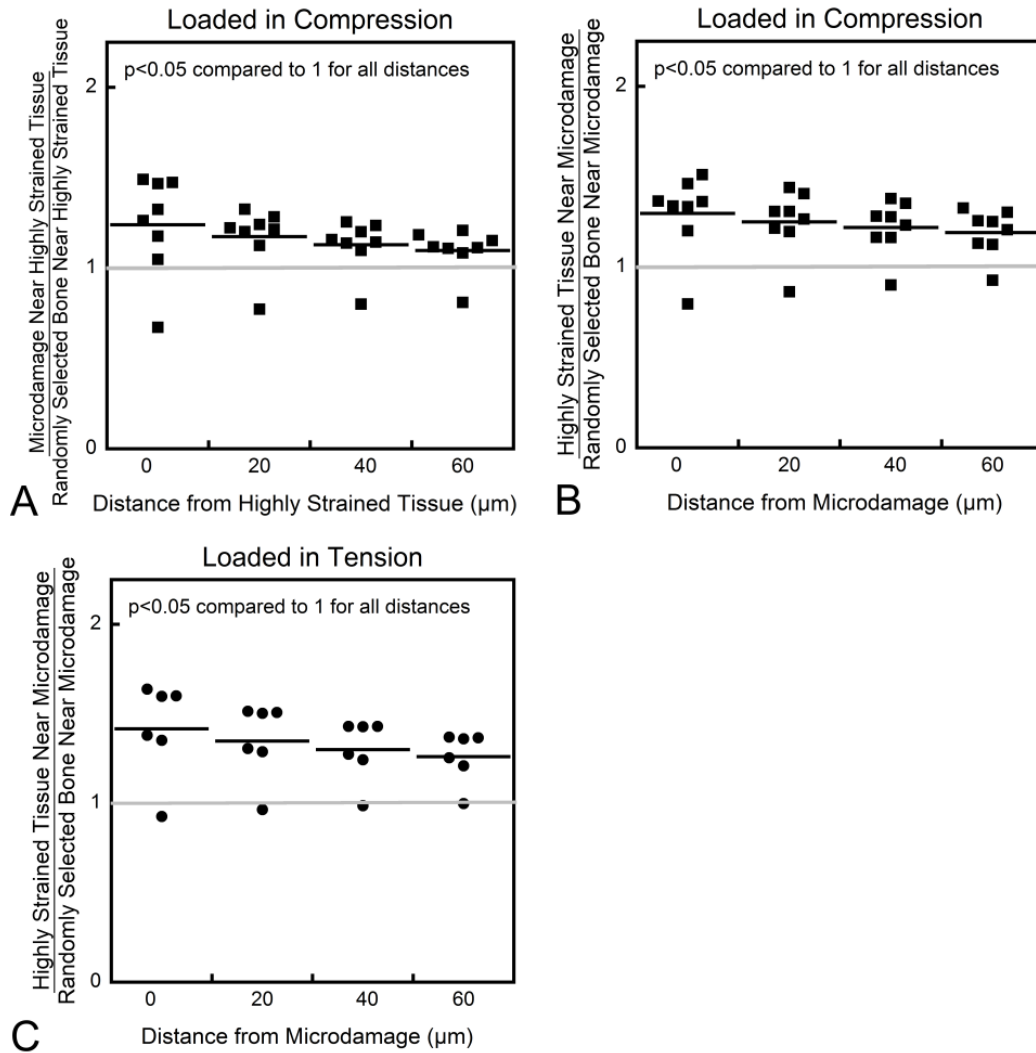


**Figure C.1** The volume-based spatial correlations between microdamage and highly strained tissue are shown at four different distances. (A) The spatial correlation between microdamage and highly strained tissue (defined as strain greater than 0.4%) and (B,C) the spatial correlation between highly strained tissue with respect to the distance between the volumes are shown.

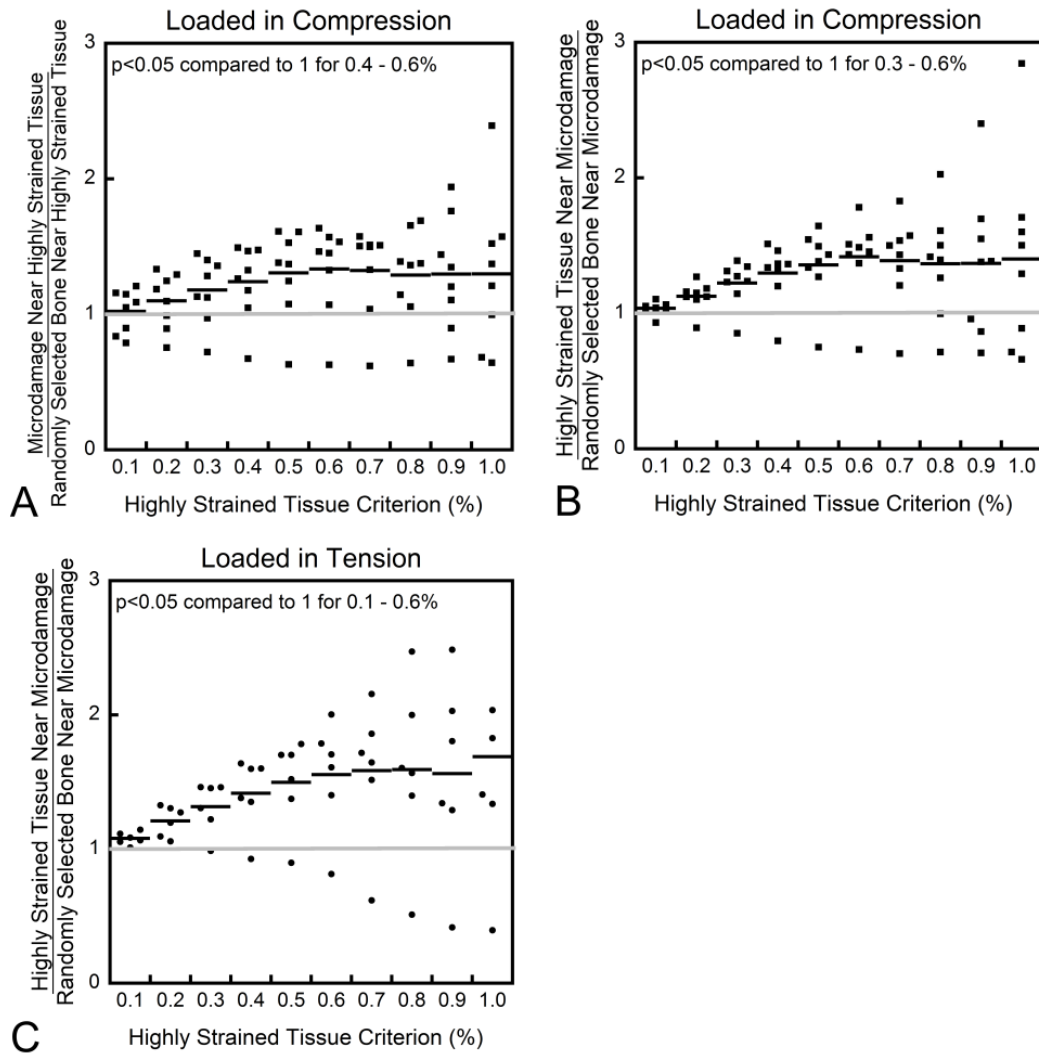


**Figure C.2** A parametric analysis determining the effect of the definition of highly strained tissue on the volume-based spatial correlations is shown. (A) The spatial correlations between microdamage and highly strained tissue for specimens (see tension in Figure 5.4 of the main text) and (B,C) spatial correlations between highly strained tissue and microdamage were greatest when the magnitude of strain used to define highly strained tissue exceeded was 0.4%.

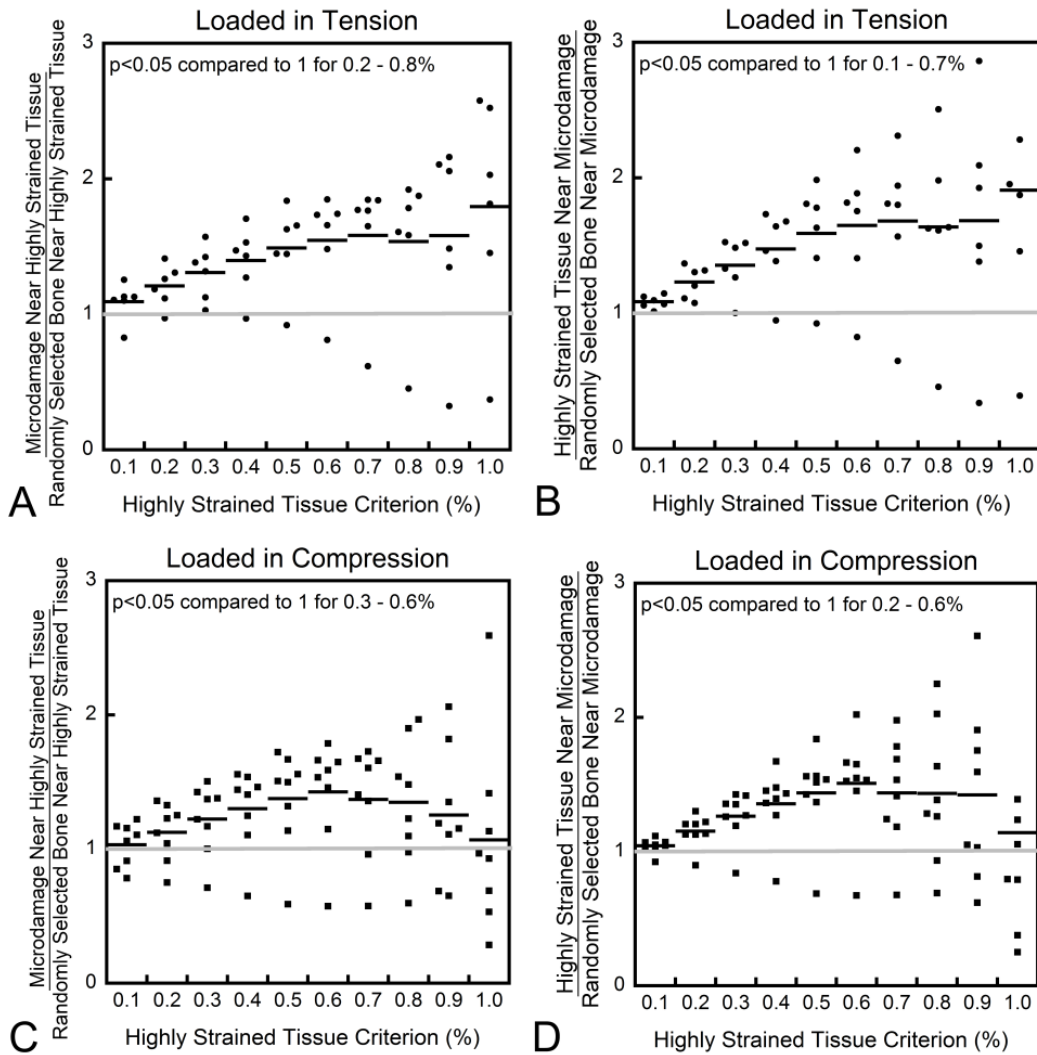


**Figure C.3** The volume-based spatial correlations for only large microdamage and highly strained tissue sites are shown. (A,C) The spatial correlation between microdamage and highly strained tissue and (B,D) the spatial correlation between highly strained tissue and microdamage are shown. Spatial correlations were greatest when the magnitude of strain used to defined highly strained tissue exceeded 0.4%.

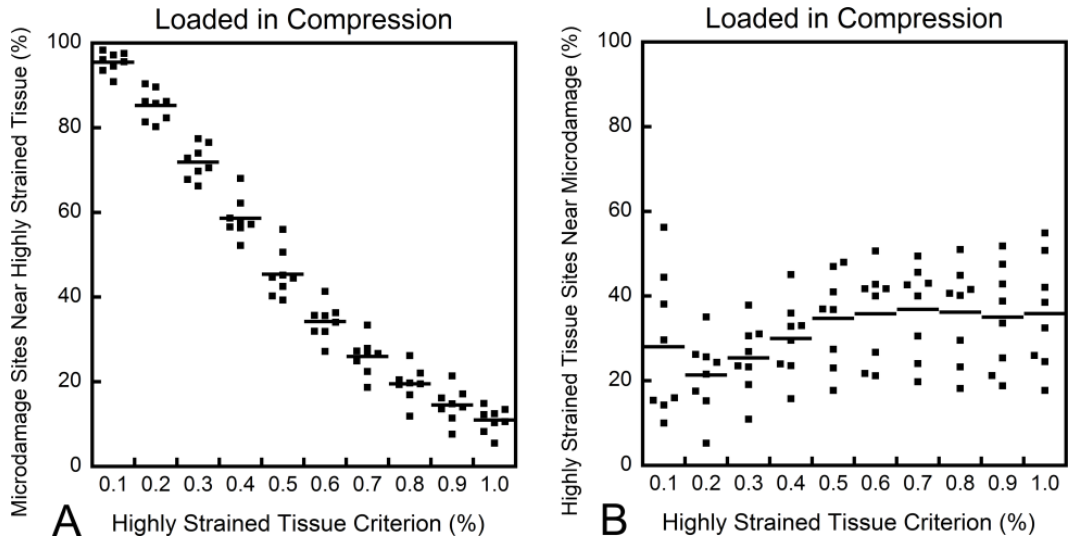


**Figure C.4** The object number-based spatial correlations are shown for specimens loaded in compression. (A) The percentage of microdamage sites near highly strained tissue was inversely proportional with the strain magnitude used to define highly strained tissue. (B) Sites of highly strained tissue were not commonly located near microdamage.

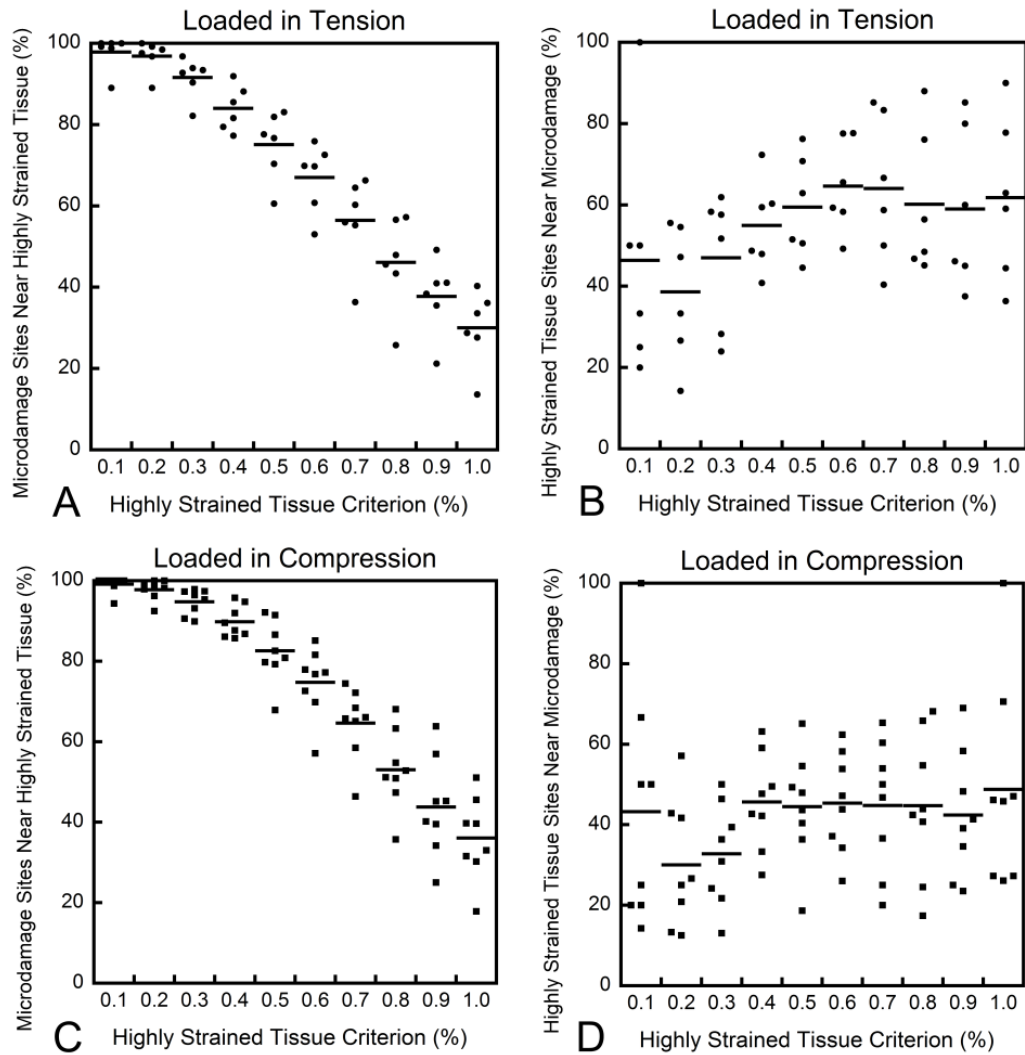


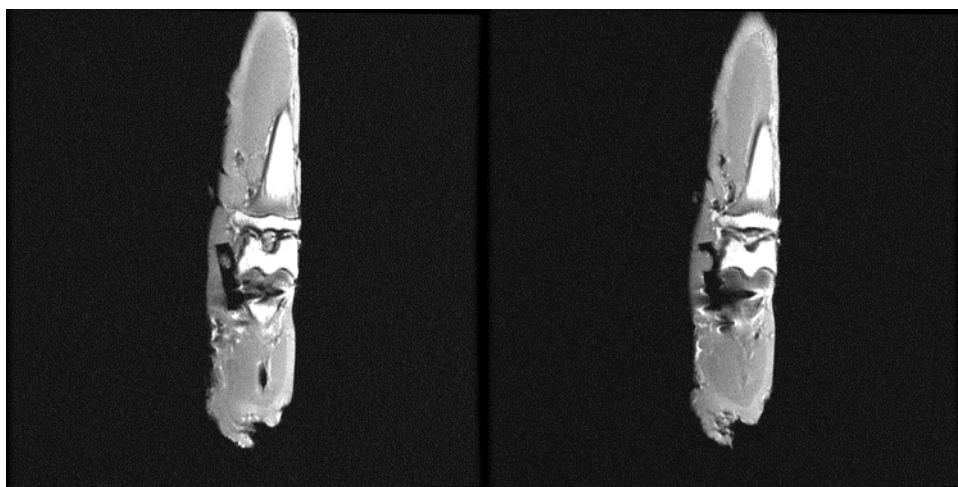
**Figure C.5** The object number-based spatial correlations are shown for large microdamage and highly strained tissue sites. (A,C) Most microdamage sites were near highly strained tissue and (B,D) most highly strained tissue sites were near microdamage.

## APPENDIX D: RABBIT STUDY PRELIMINARY MATERIAL

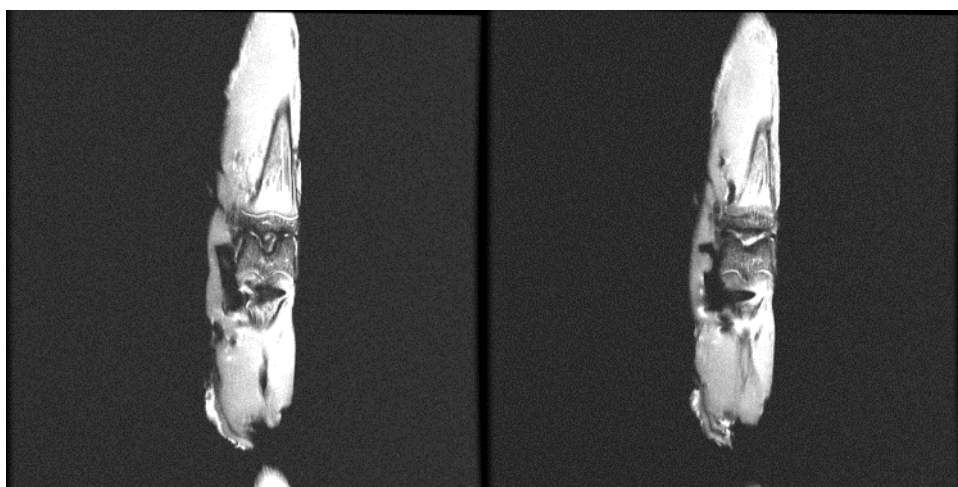
### MRI Images

One PEEK screw one Titanium screw

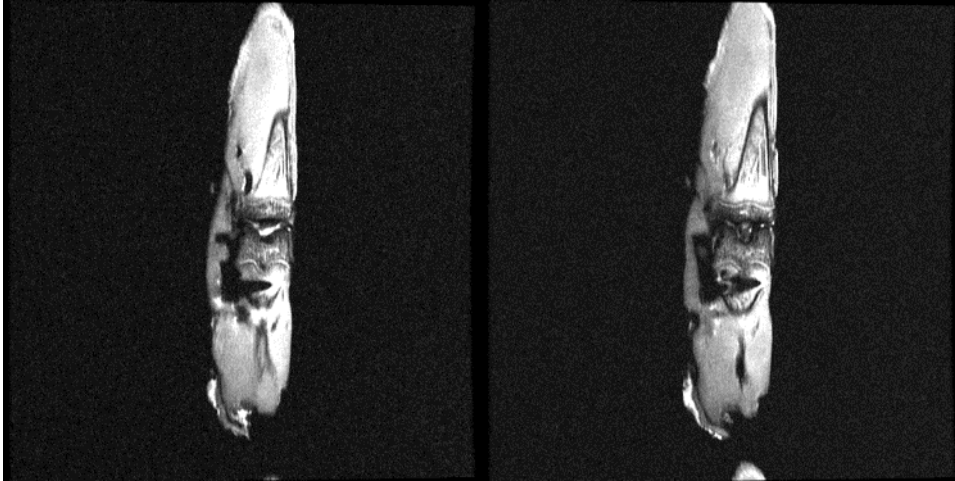
T1



T2 Stir High Res

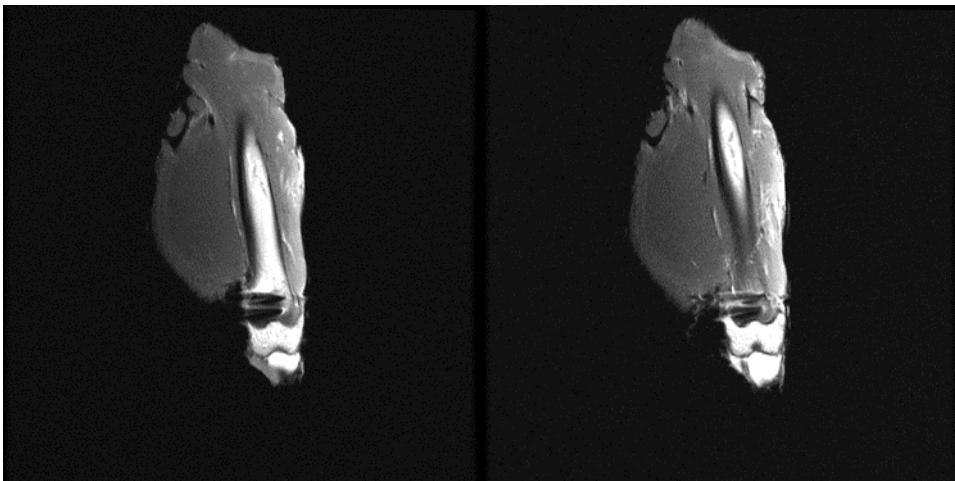


**T2 Stir Low Res**

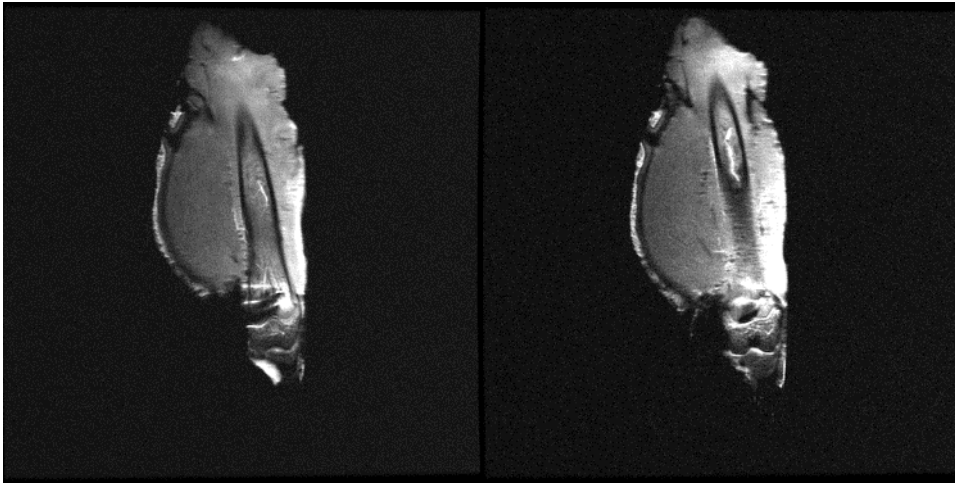


**Two Titanium screw**

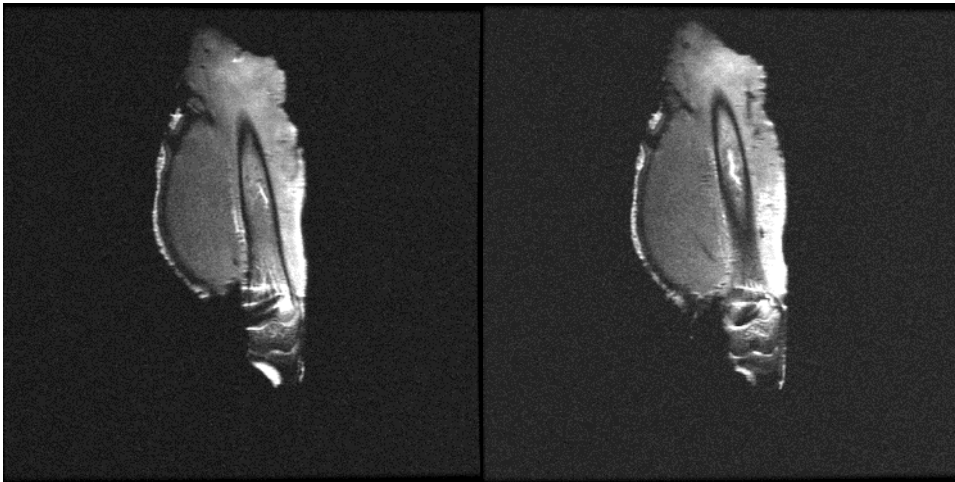
**T1**



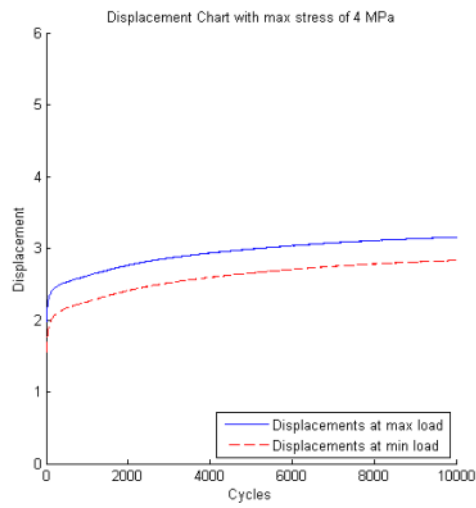
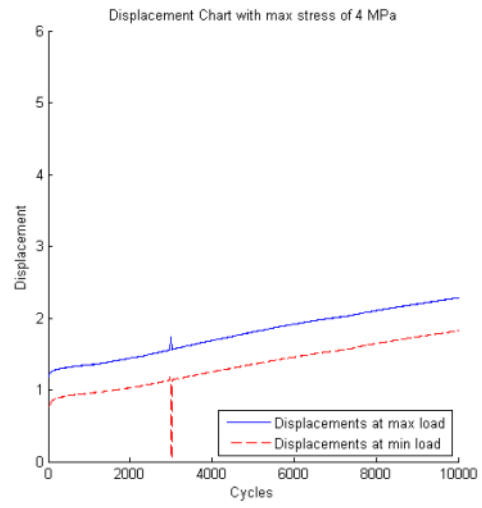
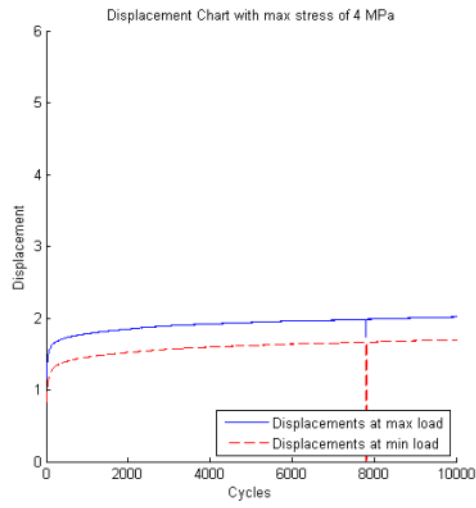
**T2 Stir High Res**



**T2 Stir Low Res**



# Rabbit Femur Loading Data



**Images of Damage Following Fatigue Loading of the Rabbit Femur**

